A Numerical Analysis of Heterogeneous and Homogeneous Truck Platoon Aerodynamic Drag Reduction

by

Michael Siemon

A thesis submitted to the Graduate Faculty of
Auburn University
in partial fulfillment of the
requirements for the Degree of
Master of Science

Auburn, Alabama
August 4, 2018

Keywords: CFD, Vehicle Platooning, Aerodynamics, Drag Reduction

Approved by

Stephen Nichols, Chair, Assistant Professor of Aerospace Engineering
David Bevly, Co-Chair, Bill and Lana McNair Endowed Distinguished Professor of Mechanical Engineering
Vrishank Raghav, Assistant Professor of Aerospace Engineering

Abstract

The purpose of this study was to provide an analysis of the aerodynamic phenomena involved with the platooning of multiple truck-trailer configurations. With fuel usage being a large factor in high operational costs of truck fleets, increases in fuel economy may drastically reduce these costs for large fleets. Furthermore, there are clear linkages between aerodynamic drag on a particular vehicle and that vehicle's fuel economy, providing incentive to decrease drag and thus decrease fuel usage. This is increasingly being achieved by the platooning of multiple vehicles coupled with a controller to govern engine usage and preserve proper separation distance between vehicles. Computational Fluid Dynamics (CFD) provides a relatively inexpensive and robust avenue for investigating drag reduction. Previous studies of these heavy vehicles have primarily focused either on single vehicle drag reduction or platoons involving two identical truck-trailer configurations. This study investigated more complex truck-trailer configurations where trailer loads were not necessarily homogeneous and therefore the wake structure behind each vehicle was somewhat unique. Modifications to lateral offset and intra-platoon separation distance in the case of homogeneous configurations, and platoon order in the case of heterogeneous configurations were all studied for their effect on platoon drag reduction. It was determined that lateral offset had a fairly significant effect on drag reduction, and platoon benefits were also incredibly sensitive to intra-platoon separation distance variation. Some effects noted in these scenarios were also present in the heterogeneous scenarios, and suggestions for platoon orders and general separation distance trends are presented.

Acknowledgments

First, I would like to thank my family, especially my parents, for driving me on towards this degree and always being enormously supportive. I am incredibly lucky to have their support, and the support of many others along the way. Acknowledgments are due to Dr. Stephen Nichols for guiding me throughout the world of CFD from the beginning, and proving himself a valuable mentor and professor throughout several years. Also, I would like to acknowledge Dr. David Bevly for providing the opportunity to work on this study and supporting me and the truck platooning team on several projects. With that, many thanks are due to the GAVLAB team this work is in support of, the members of the CFD lab for providing manpower during critical times, and to the members of IS4S and U.S. Army TARDEC for providing feedback and assistance in earlier project stages of this work. Thanks goes to Ben Urick and Ben Marussig for allowing use of their wonderful graphics demonstrating the woes of taking a CAD model into a CFD problem. Finally, this thesis and much other work would not have been possible without the HPC team at Auburn University and their maintenance and troubleshooting of the *Hopper* cluster.

Table of Contents

Abstract ii

Acknowledgments iii

1 Introduction 1

1.1 Literature Review 4

1.1.1 Overview of Truck Platooning Projects 4

1.1.2 Aerodynamic Studies of Truck Platooning 6

2 Computational Fluid Dynamics 9

2.1 General Equations 9

2.2 Turbulence Modeling 11

2.2.1 Reynolds Averaging 11

2.2.2 Turbulent Boundary Layer, Prandtl Mixing Length Theory, and Wall Coordinates 13

2.2.3 k, ε and ω 16

2.3 Solver 17

2.3.1 *Tenasi* Unsteady Incompressible 3D RANS 18

2.3.2 Blended $k-\epsilon$, $k-\omega$ Turbulence Model 20

3 Solution Methodology 22

3.1 CAD Models 22

3.2 Grid Generation 25

3.2.1 Surface Mesh Generation 26

3.2.2 Volumetric Grid Generation 31

3.3 CFD Simulation 35

3.3.1 Solver Parameters 35

3.3.2 Description of Cases 37

4 Results & Discussion 39

4.1 Baselines 39

4.2 Lateral Offset 45

4.3 Intra-Platoon Separation Distance Variation 57

4.4 Heterogeneous Platoon 63

5 Conclusions & Future Work 71

5.1 Conclusions 71

5.2 Future Work 72

References 74

Appendices 78

A Useful General CFD Equations 79

A.1 Approximation of y^+ 79

A.2 Courant-Friedrichs-Lewy (CFL) Condition 80

B Selection of Time-Accurate Results: Lateral Offset 81

List of Figures

1.1 Diagram of the separation region present on the trailing edge of a bluff body, such as a trailer [3] 2

1.2 Fuel savings from two-vehicle experimental tests conducted by Auburn University [9] 5

1.3 Lateral offset vs ideal platoon drag reduction from two-vehicle platoon CFD study conducted by Auburn University [9] 5

3.1 Image of Peterbilt 579 truck [26] 23

3.2 Peterbilt 579 model as featured in previous Auburn University studies [9, 10, 27] 23

3.3 Peterbilt 579 model used in this study 23

3.4 Peterbilt 579 model with box trailer, front view 24

3.5 Peterbilt 579 model with box trailer, side view 25

3.6 Peterbilt 579 model unloaded flatbed trailer 25

3.7 Peterbilt 579 model with centered 20 ft. shipping container 25

3.8 Peterbilt 579 model with full shipping container load 26

3.9 Example of an intersection between two surfaces and the lower order curves approximating each surface [28] 27

3.10 Example of a surface-surface intersection (SSI) where non-identical sampling points cause a gap between surfaces when imported into a mesh generation package [28] 27

3.11 Initial fully-triangular surface mesh for the box trailer configuration 29

3.12 Mixed triangular and quadrilateral element surface mesh for box trailer configuration after volume grid generation 29

3.13 Initial fully-triangular surface mesh for the full shipping container trailer configuration 29

3.14 Initial fully-triangular surface mesh for the centered shipping container trailer configuration 29

3.15 Initial fully-triangular surface mesh for the unloaded flatbed trailer configuration 30

3.16 Refined groundplane around individual truck 31

3.17 Farfield domain around single truck 32

3.18 Depiction of anisotropic cell growth on farfield wall surface domain 33

3.19 Depiction of the ”source” feature (in yellow) around the vehicle 33

3.20 View of anisotropic elements built off of the vehicle and groundplane. Blue elements are hexes and green elements are prisms 34

3.21 Slice of the volume grid around a single box trailer vehicle. Tetrahedral elements (red) are smaller in the area of the ”source” feature than outside. Near-body and near-groundplane regions contain all anisotropic elements as pictured in Figure 3.20 34

3.22 Typical example of drag force convergence for a CFD simulation 36

4.1 Static pressure contour for the isolated box trailer configuration baseline case. Grid is demarcated in uniform 1.0 meter increments. The subtitle, 2.25154, refers to z-location of the coordinate plane, in meters 40

4.2 Static pressure contour for the isolated full shipping container trailer configuration baseline case. Grid is demarcated in uniform 1.0 meter increments 41

4.3 Static pressure contour for the isolated centered shipping container trailer configuration baseline case. Grid is demarcated in uniform 1.0 meter increments . . 41

4.4 Static pressure contour for the isolated unloaded flatbed trailer configuration baseline case. Grid is demarcated in uniform 1.0 meter increments 42

4.5 Overhead view of x velocity (with +x being flow direction) for box trailer in baseline configuration. Grid is demarcated in uniform 1.0 meter increments . . 42

4.6 Overhead view of x velocity (with +x being flow direction) for full shipping container trailer in baseline configuration. Grid is demarcated in uniform 1.0 meter increments. The subtitle, 1.66819, refers to y-location of the coordinate plane, in meters 43

4.7 Overhead view of x velocity (with +x being flow direction) for centered shipping container trailer in baseline configuration. Grid is demarcated in uniform 1.0 meter increments 43

4.8 Overhead view of x velocity (with +x being flow direction) for unloaded flatbed trailer in baseline configuration. Grid is demarcated in uniform 1.0 meter increments 44

4.9 Drag reduction for lead and follower vehicles in lateral offset tests 46

4.10 Drag reduction for two truck homogeneous platoon as a function of lateral offset, 20 ft. separation distance 46

4.11 X-Velocity profile for homogeneous, two box trailer platoon with 10 ft separation distance at 0%, 10%, 25% and 50% lateral offset 48

4.12 X-Velocity profile for homogeneous, two box trailer platoon with 20 ft separation distance at 0%, 10%, 25% and 50% lateral offset 50

4.13 X-Velocity profile for homogeneous, two box trailer platoon with 30 ft separation distance at 0%, 10%, 25% and 50% lateral offset 52

4.14 X-Velocity profile for homogeneous, two box trailer platoon with 40 ft separation distance at 0%, 10%, 25% and 50% lateral offset 54

4.15 X-Velocity profile for homogeneous, two box trailer platoon with 50 ft separation distance at 0%, 10%, 25% and 50% lateral offset 56

4.16 Drag reduction for three vehicle platoon, L-F1 and F1-F2 separation distance being equal 58

4.17 Drag reduction for three vehicle platoon with L-F1 varied, F1-F2 separation constant at 100 ft. 59

4.18 Comparison of drag reduction for a select number of variations in intra-platoon separation distance 59

4.19 X-Velocity profile for three vehicle homogeneous platoon with uniform 100 ft separation distance 60

4.20 X-Velocity profile for three vehicle homogeneous platoon with 130 ft separation distance between L - F1 and 100 ft separation distance between F1 - F2 61

4.21 X-Velocity profile for three vehicle homogeneous platoon with 100 ft separation distance between L - F1 and 130 ft separation distance between F1 - F2 62

4.22 Drag reduction for heterogeneous platoon scenario 1, described in Table 3.3 . . 64

4.23 Drag reduction for heterogeneous platoon scenario 2, described in Table 3.3 . . 65

4.24 Drag reduction for heterogeneous platoon scenario 3, described in Table 3.3 . . 65

4.25 Static pressure contours for scenario 1, described in Table 3.3, at 50 ft. 66

4.26 Static pressure contours for scenario 1, described in Table 3.3, at 100 ft. 66

4.27 Static pressure contours for scenario 1, described in Table 3.3, at 150 ft. 67

4.28 Static pressure contours for scenario 1, described in Table 3.3, at 200 ft. 67

4.29 Static pressure contours for scenario 2, described in Table 3.3, at 50 ft. 68

4.30 Static pressure contours for scenario 2, described in Table 3.3, at 100 ft. 68

4.31 Static pressure contours for scenario 2, described in Table 3.3, at 200 ft. 69

4.32 Static pressure contours for scenario 3, described in Table 3.3, at 50 ft. 69

4.33 Static pressure contours for scenario 3, described in Table 3.3, at 200 ft. 70

B.1 X-Velocity profile for homogeneous, two box trailer platoon with 20 ft separation distance, 0% lateral offset, at various points in time (results are averaged across 0.1 second increments) 83

B.2 X-Velocity profile for homogeneous, two box trailer platoon with 20 ft separation distance, 10% lateral offset, at various points in time (results are averaged across 0.1 second increments) 86

List of Tables

3.1 Edge length values for cells in surface meshes on the various vehicle combinations. Values in (Combined) represent cells after undergoing combination in full grid generation 28

3.2 Description of typical grid composition for the cases presented in this thesis . . 38

3.3 Order of vehicles for heterogeneous 4 truck platoon scenarios 38

Chapter 1

Introduction

Truck transportation makes up 0.81% of the U.S. GDP, accounting for 27% of the for-hire transportation services GDP [1]. Fuel usage is the highest operational cost for truck fleets of all sectors in the United States, accounting for 38% of the total marginal operating cost [2]. Therefore, it is extremely desirable to reduce fuel consumption for vehicles across such fleets as any change will significantly affect overall operational cost. Fuel consumption for these vehicles is for the majority controlled by three key aspects [3] : engine losses due to thermal efficiency (60%), aerodynamic losses (21%), and losses due to rolling resistance (13%). Due to the relative ease of aerodynamic modification, especially compared to modifications of the engine systems, much work has been done to reduce these aerodynamic losses.

Approximately 25% of the aerodynamic drag occurs on the rear end of the trailer section, caused by the low pressure separation region present off this trailing edge [3]. Reduction of this base drag by implementation of boat-tail devices or flap extenders on the rear of the trailer has resulted in 4% to 10% fuel savings from these features alone [3, 4]. Since approximately another 25% of the aerodynamic drag is present on the front face of the tractor [3], allowing vehicles to take advantage of this separation via “drafting” have the benefit of both reducing the frontal pressure of the rear vehicle and modifying the separation on the trailing edge of the lead vehicle. Such scenarios have been tested with automated platoons of trucks [5] and have resulted in measurable fuel savings across the platoon. Thus, as vehicle autonomy and electronic driving assistance become more common in the automotive world it makes sense from a cost perspective to leverage these advances further by more common formation of these platoons, as this method requires no modification to the exterior of the vehicles. Platooning

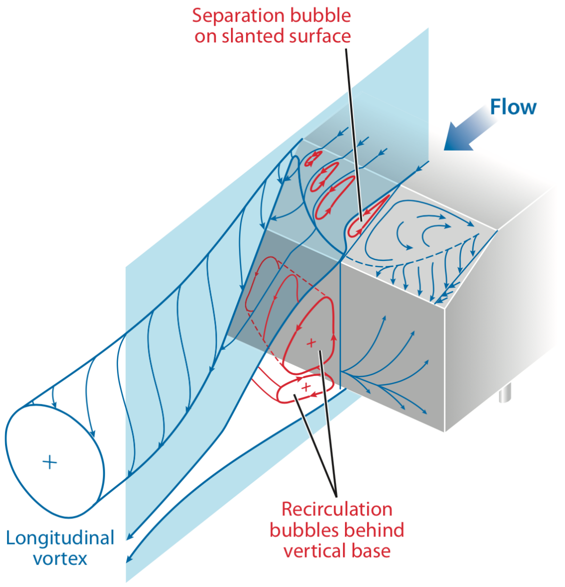

Figure 1.1: Diagram of the separation region present on the trailing edge of a bluff body, such as a trailer [3]

instead provides a method of intelligently using existing technology and hardware to reduce drag and fuel costs.

While it is necessary of course to investigate the full-scale real-world results of such scenarios via experimental track and road testing, the sole use of these methods can be rather cost prohibitive. These costs only compound as tests broaden in scope and this also often has the added problem of incurring additional lead time before actual testing. This means there can be quite significant time periods between the formulation of testing plans and the actual analysis of results from said tests. It is therefore beneficial to seek alternatives in the meantime to investigate more broad scenarios and narrow down specific cases to be relegated to experimental testing. Scale models of vehicles are commonly implemented in wind or water tunnel testing, but this approach is subject to problems associated with both model and tunnel design. Vehicle models often do not feature rotating wheels and there is no ability to translate the ground-plane below them due to tunnel limitations. These factors drastically alter the ability of the scale tests to realistically model flow phenomena as they cannot replicate real-world driving conditions. The absence of these features has been proven to have a significant impact on measured drag values [6, 7] as they substantially change the overall flow field characteristics. Running such wind tunnel tests also can be quite cost-prohibitive depending on the specific facility and cases in question, and for many facilities the models must be quite small in order to prevent significant blockage in the test section.

Computational Fluid Dynamics (CFD) offers an alternative to model scale testing. This approach allows for relatively low cost investigation of flow dynamics at full scale (though somewhat limited by the specific computational resources available) and with the ability to appropriately set boundary conditions, such as on the ground-plane and wheels of a vehicle. An added benefit is the ability to probe any modeled space in the computational domain for flow characteristics. This provides a more in-depth picture of the flow-field when compared to results obtained by experimental tests which are limited by expensive probes and narrow images of particle traces. However, there are several sources of error that one must be aware of before undertaking such simulations. In order to properly utilize computational resources, there must first be a discretization of differential equations which results in some level of discretization error. There are yet further errors introduced by the discretization of a spatial domain into elements and volumes, where too coarse a domain incurs unwanted numerical dissipative effects. And not last nor least, there does not yet exist any definitive model for turbulence, so highly turbulent flows must be modeled with various approximations, each model having different characteristics than any other.

However, with proper acknowledgment of these limitations, and careful efforts to reduce their effects on solutions, CFD remains an ideal tool to perform initial and wide-ranging investigations of the aerodynamic phenomena present in truck platooning scenarios. This thesis presents several cases of truck platoons featuring both homogeneous and heterogeneous trailer loads, where drag reduction and flow features will be analyzed via CFD. Generally, all platoons will feature results at various separation distances, regardless of the other specific factors being analyzed in each case.

1.1 Literature Review

1.1.1 Overview of Truck Platooning Projects

A brief survey of past efforts involving truck platooning is necessary before more in-depth aerodynamic discussion in order to properly understand motivations and analyze which kinds of cases are relevant for further investigation. In the context of this thesis, those projects which prominently aimed for energy savings by means of drafting are the most relevant, however within the wider field of autonomous vehicle development, these are also the most recent as well as the least studied. The basic idea shared amongst all these projects is the implementation of a combination of sensors and communications for sharing separation distances and speed differences amongst all the trucks for cooperative longitudinal control.

A 2011 study under the “Energy ITS” project [8] is perhaps one of the earliest looks at truck platooning as a means for fuel saving. In this study, a platoon of three trucks was tested under both highway and test track conditions, with a constant controlled velocity of around 22 m/s and a controlled gap of 10 m. A broad suite of tests were conducted involving the use of adaptive cruise control (ACC) within traffic scenarios in addition to the intra-platoon cooperative adaptive cruise control (CACC) used to maintain truck separation distances, as well as tests involving cut-ins of other vehicles within the truck platoon. Lateral control was also implemented via machine vision units which measured offset with respect to lane markers, resulting in a tight lateral control of +/- 15 cm on highway tests and +/- 6 cm on track tests. Overall the mean fuel savings for the three vehicle platoon scenarios were around 14% when compared to a single vehicle. Furthermore, it was found that the middle truck experienced the greatest reduction with the third truck experiencing only slightly less savings.

Further fuel economy testing was conducted by a group of researchers from Auburn University[9] for a two vehicle platoon at various separation distances. The platoon in this case was run at 65 mph (approx 29 m/s) with purely longitudinal control and no lateral control. Surprisingly, it was observed that the fuel savings experienced by the follower truck greatly diminished for the smallest separation distance. An analysis of engine ambient temperature, fan cycle, and the torque load (affected by the controller) was conducted [10] in order to investigate possible causes of this decreased fuel savings. There was no clear indication that any of these factors would have caused such a significant shift in trends, however it was theorized that the lack of tight lateral control may have played a part. That is to say, at the smaller separation distances the follower truck was not receiving the full benefits of the wake of the front truck due to lateral misalignment.

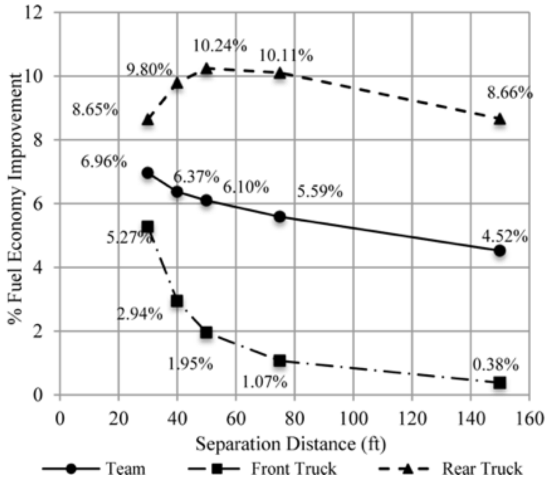

Figure 1.2: Fuel savings from two-vehicle experimental tests conducted by Auburn University [9]

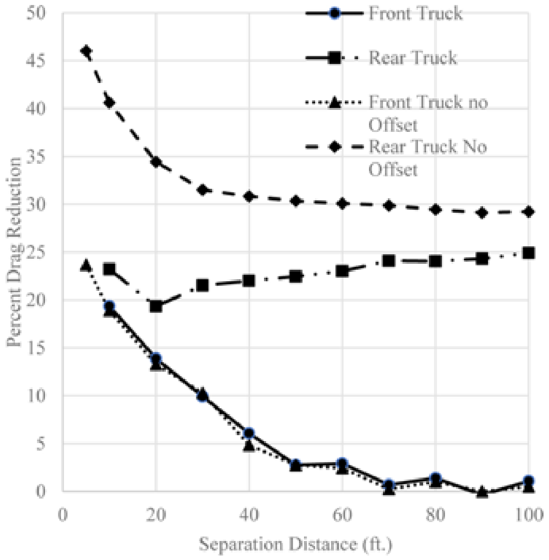

Figure 1.3: Lateral offset vs ideal platoon drag reduction from two-vehicle platoon CFD study conducted by Auburn University [9]

Finally, one of the most comprehensive studies to date of a truck platoon using CACC longitudinal control was conducted in 2017 by a joint US and Canadian research team [11]. Fuel testing was conducted on a test track with two and three truck platoons traveling at about 65 mph (29 m/s). Scenarios were tested with all trucks featuring side-skirt and boat-tail devices, as well as scenarios where one of the trucks only had a standard box trailer for comparison. This is one of the only fuel test studies currently available featuring such mismatched vehicles, resulting in some degree of heterogeneity compared to the purely homogeneous platoons discussed previously. The two-truck, mismatched platoon at 12 m separation distance featured a standard trailer on the trailing truck and achieved 5% fuel savings. The scenario where both trucks featured boat-tails resulted in a comparative 6.6% fuel savings. Furthermore, a three truck platoon at the same separation distance, where the middle truck featured a standard trailer, achieved a platoon savings of 7.6% and 5.2% at 12 m and 58.1 m, respectively. The homogeneous three truck platoon featuring all boat-tails however achieved fuel savings of 9.5% and 5.3% at the same separation distances. This seems to suggest that such mismatched trailer configurations have a non-negligible effect at smaller separation distances. It should be also noted that the last vehicle in each platoon scenario experienced a similar effect as seen in the Auburn study, where significantly small separation distances (below about 10 m in this case) resulted in decreased fuel savings. The platoon as a whole however still saw monotonically decreasing fuel savings as separation distance increased.

1.1.2 Aerodynamic Studies of Truck Platooning

While extensive work has been done in the past to aerodynamically characterize individual automotive vehicles, including trucks, far less has been with regards to truck platooning itself. Aerodynamic work has been focused on both scale model experimental methods and numerical methods but it should be noted that there also exists some discrepancy between the two in several cases. This can be expected to an extent due to the errors inherent in both lines of testing discussed previously, and of course the optimal solution to this problem has been to validate as best possible with full scale, real world testing.

A 2012 study by Schito and Braghin [12] was conducted in order to characterize a variety of platooning scenarios with scale CFD and wind tunnel models. While the authors did not investigate platoon configurations with multiple trucks, the results nonetheless serve to highlight some of the key factors governing wake behavior and aerodynamic benefit. Two configurations featuring like-sized vehicles were studied, made up of a van, a compact car, and a sedan with slanted back. A maximum 20% drag reduction was seen on the van when it was in the lead position and the compact car and van both experienced about a 40% drag reduction as trailing vehicles. However, in the scenario featuring the sedan with slanted back in lead and the van in the third position, while the sedan experienced about the same profile as the leader van previously with a maximum 20% drag reduction, the compact car and van experienced much less significant drag reductions than before (about 20-25%). In a platoon configuration with a compact car and sedan following a truck, while the truck experienced negligible to no difference in drag, the following vehicles saw anywhere from 80% to 50% reduction in drag. These results point to the lead vehicle being highly sensitive to the size of follower vehicles while the follower vehicles are in turn affected by the end-profile of the lead vehicle, with more bluff and wide bodies giving best results.

A more focused, full-scale CFD study of truck platooning specifically was presented in 2014 [13] with two and three truck platoons of a generic truck model at various separation distances. Overall it was found that quite significant reductions were experienced for the last following vehicle in both scenarios, with the lead vehicle approaching base drag at higher separation distances. More important for the purposes of this Master Thesis however was the comparison between pure Reynolds-Averaged Navier-Stokes (RANS) solutions with Detached Eddy Simulation (DES) models and a Very Large Eddy Simulation (VLES) model. It was found that the RANS solutions did not perform well in regions with strong swirl such as in cases of separation and recirculation when compared to DES and VLES simulations (which were in agreement with each other), key effects that must be modeled accurately in the case of highly separated flows like those present off the trailing edge of truck trailers.

A team comprised of researchers from Argonne National Laboratory and Cummins Inc. [14] similarly presented results from a CFD study on the platooning of two and three trucks, but with added variability in lateral offset for the two vehicle cases as well as yaw angle sweeps. For 0 , 6 and -6 degree yaw angle results were compared between a two vehicle platoon with no lateral offset and a two vehicle platoon with each vehicle in a different lane (accounting for about 50% of the trailer width). Drag values were then yaw-averaged to provide a better indication of true drag reduction across the various yaw angles. For both the lead and follow vehicles, the addition of the lateral offset on the follower vehicle led to almost a 1/2 decrease in measured drag reduction. Tests were also done with three vehicles where two trucks were side-by-side (in different lanes) in lead of a truck directly behind one of the lead vehicles and it was again found that the tail vehicle at a lateral offset was the most sensitive to any variability in upstream conditions. This sensitivity of the tail vehicle to lateral offset and upwind conditions is echoed in a 2017 thesis by Humphreys [10] where two-vehicle platoons were tested with both lateral offset (again, at a maximum offset of about 50% of the trailer width) and under crosswind conditions. A local maximum in drag reduction was observed for a non-minimum separation distance and results at an offset differed significantly from the centered cases.

1:50 scale wind tunnel tests were conducted recently at Lawrence Livermore National Laboratory [15] on two and three truck platoons. Lateral offsets were tested for the two vehicle platoons, similar to the tests previously discussed. For small separation distances of 50 ft or less, the effect of an imposed lateral offset was more significant than at 100+ ft separation distances but still determined to be relatively insignificant at 5% or less variation when compared to the no offset cases. The wake from the lead truck was noted as much wider than the tested lateral offsets.

Clearly then, there are still many questions that are left unresolved, like in the case of lateral offset, or wholly unanswered when it comes to the study of drag reduction for truck platoon scenarios. This thesis revisits some of these factors discussed in previous literature with extended simulation parameters. A focus on variability in intra-platoon separation distance is also conducted in order to determine the sensitivity and nature of the complex system existing between trucks. Finally, this thesis attempts to characterize something which no other current literature (to the best of the author's knowledge) examines: platoons made of highly heterogeneous trailer configurations. While some of the previous studies discussed have examined some variability in trailer devices, they have all featured standard box trailer profiles homogeneously. Additionally, they are nearly all limited to two or three vehicles. As the scope of truck platooning expands and more emphasis is placed on dynamic formation platoons, it is reasonable to expect that platoons can be made of more than two vehicles and that the degree of variability in trailer configurations is bound to increase, beyond just modifications of the standard box trailer. The next chapter provides some description of the numerical methods used to achieve these simulations.

Chapter 2

Computational Fluid Dynamics

The modeling of fluids and their behavior given a set of boundary and initial conditions is known as Computational Fluid Dynamics (CFD). There are several given sets of equations for modeling different phenomena, especially in the cases of heat transfer and fluid chemical reactions. The most general equations for representing any given fluid flow are the Navier-Stokes equations, developed in the 19th century. In contrast with the Euler equations published the century prior, the Navier-Stokes equations account for viscous effects in a fluid system. In other words, the Navier-Stokes equations represent a dissipative system. Both sets of equations arise from a conservation of mass, momentum, and energy. As such, they are highly non-linear and there exists no current analytical (exact) method of solving. These partial differential equations (PDE) are instead solved via numerical methods, with the governing equations discretized spatially as well as temporally. This form is then iteratively solved until convergence is reached. The discretization of equations can be accomplished via such techniques as Finite Difference Method (FDM) or Finite Element Method (FEM), but the Finite Volume Method (FVM) is most commonly used for CFD purposes. This method solves the flux through faces of the fluid volume domains, rather than propagating a difference between spatial points as in a FDM scheme.

2.1 General Equations

There are many different forms by which the governing equations discussed previously may be presented. For conceptual explanation purposes only, let us consider a conservative form of the 2-D unsteady Navier-Stokes equations, which consists of four equations: continuity, x-momentum, y-momentum, and energy. These can be expressed as

$$\frac{\partial Q}{\partial t} + \frac{\partial E}{\partial x} + \frac{\partial F}{\partial y} = \frac{\partial E_V}{\partial x} + \frac{\partial F_V}{\partial y} \tag{2.1}$$

where

$$Q = \begin{bmatrix} \rho \\ \rho u \\ \rho v \\ e \end{bmatrix}, E = \begin{bmatrix} \rho u \\ \rho u^2 + P \\ \rho uv \\ u(e+P) \end{bmatrix}, F = \begin{bmatrix} \rho v \\ \rho uv \\ \rho v^2 + P \\ v(e+P) \end{bmatrix} \tag{2.2}$$

$$E_v = \begin{bmatrix} 0 \\ \tau_{xx} \\ \tau_{xy} \\ f_4 \end{bmatrix}, F_v = \begin{bmatrix} 0 \\ \tau_{xy} \\ \tau_{yy} \\ g_4 \end{bmatrix} \tag{2.3}$$

The Q matrix represents the conservative quantities, with ρ being the density and e being the total energy, both expressed as per unit volume. The other terms in Q are the momentum terms in both dimensions. E and F are the inviscid flux vectors, where forces and work exerted by pressure, P, are accounted for.

E_V and F_V encompass the terms representing viscosity and heat conduction. For a Newtonian fluid, the viscous (shear) stresses in this 2-D case may be expressed by

$$\begin{aligned} \tau_{xx} &= \mu(\frac{4}{3}\frac{\partial u}{\partial x} - \frac{2}{3}\frac{\partial v}{\partial y}), \\ \tau_{xy} &= \mu(\frac{\partial u}{\partial y} + \frac{\partial v}{\partial x}), \\ \tau_{yy} &= \mu(-\frac{2}{3}\frac{\partial u}{\partial x} + \frac{4}{3}\frac{\partial v}{\partial y}) \end{aligned} \tag{2.4}$$

where μ is dynamic viscosity, a function of temperature and calculated via Sutherland's law. The terms f_4 and g_4 are a combination of work done by viscous forces and heat conduction. Assuming ideal gas conditions, these are written as

$$\begin{aligned} f_4 &= u\tau_{xx} + v\tau_{xy} + \frac{\mu}{Pr(\gamma-1)}\frac{\partial(\gamma RT)}{\partial x} \\ g_4 &= u\tau_{xy} + v\tau_{yy} + \frac{\mu}{Pr(\gamma-1)}\frac{\partial(\gamma RT)}{\partial y} \end{aligned} \tag{2.5}$$

where Pr is the Prandtl number (a ratio of kinematic viscosity to thermal diffusivity), γ is the ratio of specific heats, R is the specific gas constant, and T is the temperature.

2.2 Turbulence Modeling

The study of turbulence is an important topic for many fluid dynamics scenarios and the modeling of turbulence is key for the solving of the Reynolds-Averaged Navier-Stokes (RANS) equations. No exact method exists for solving turbulence, and as such there are a variety of methods for modeling turbulent phenomena numerically. A brief discussion of how these equations arise via Reynolds-Averaging is beneficial before further analysis of specific turbulence models.

2.2.1 Reynolds Averaging

In order to properly consider turbulence, it is first necessary to move from the 2-D equations presented previously to 3-D. The basic Cartesian 3-D momentum equations (ignoring body forces) can be expressed in tensor notation as

$$\rho(\frac{\partial u_i}{\partial t} + u_j\frac{\partial u_i}{\partial x_j}) = \frac{\partial \sigma_{ij}}{\partial x_j} \quad i,j = (1,2,3) \tag{2.6}$$

where σ_{ij} is the stress tensor for three dimensions. The stress tensor is a combination of the shear stress terms τ and the pressure terms presented in Equations 2.1 - 2.3. It is represented as

$$\sigma_{ij} = -P\delta_{ij} + \mu(\frac{\partial u_i}{\partial x_j} + \frac{\partial u_j}{\partial x_i}) - \frac{2}{3}\mu\frac{\partial u_k}{\partial x_k}\delta_{ij} = -P\delta_{ij} + \tau_{ij} \quad i,j = (1,2,3) \tag{2.7}$$

where δ_{ij} is the Kronecker delta function.

The flow variables themselves are observed to have relatively small fluctuations in time around a mean value, and can thus be expressed as a sum of both the steady value and the fluctuations. For example, the x-velocity u is then written as

$$u = \bar{u} + u' \tag{2.8}$$

where $\bar{u}$ is the steady value and u' is the time-dependent fluctuation value. The other components of velocity follow the same treatment, as well as scalars such as pressure and temperature. Each variable, $f(\mathbf{x}, t)$, may then be time-averaged to produce an average value $\bar{f}(\mathbf{x})$ by

$$\bar{f}(\mathbf{x}) = \lim_{t\to\infty} \frac{1}{t}\int_{t_0}^{t_0+t} f(\mathbf{x}, t)dt \tag{2.9}$$

For the momentum equations in Equation 2.6, after substituting in variables of the nature of Equation 2.8 and applying appropriate time averaging rules, the equations take the form of

$$\frac{\partial}{\partial x_j}(\rho(\bar{u}_j\bar{u}_i + \overline{u_j{}'u_i{}'})) = \frac{\partial}{\partial x_j}(\bar{\sigma}_{ji}) \tag{2.10}$$

Finally, with decomposition of the stress tensor into pressure and viscous stress from Equation 2.7 and the rearranging of terms, the momentum equation may be expressed as

$$\frac{\partial}{\partial x_j}(\rho\bar{u}_j\bar{u}_i) = -\frac{\partial \bar{P}}{\partial x_i} + \frac{\partial}{\partial x_j}(\bar{\tau}_{ij} - \rho\overline{u_j{}'u_i{}'}) \tag{2.11}$$

The $\rho\overline{u_j{}'u_i{}'}$ term is then a new term in comparison with the original form of Equation 2.6 and referred to as the *Reynolds stress*. This term, while mathematically derived, is experimentally quantifiable and a reflection of the time-dependent nature of turbulent flow. It is this term that is the basis for modeling turbulence in the boundary layer. An attempt at modeling this term algebraically was proposed by Boussinesq in the 1870s with a "zero-equation" model, making Reynolds stress analogous to molecular shear via a term known as eddy viscosity, μ_t. It should be noted that this term is solely a property of flow conditions and is not an intrinsic property of the fluid. Thus, the Reynolds stress in such a zero-equation model can be expressed as

$$-\rho\overline{u_j'u_i'} = \mu_t\left(\frac{\partial u_i}{\partial x_j} + \frac{\partial u_j}{\partial x_i} - \frac{2}{3}\frac{\partial u_k}{\partial x_k}\delta_{ij}\right) - \frac{2}{3}\rho k\delta_{ij} \tag{2.12}$$

where k is the turbulence kinetic energy which will be defined later. However, this method still involves the solving of five highly nonlinear equations and this approach does not adequately capture all cases, like that of an asymmetrical wake. For this reason, other one-equation and two-equation approaches have been developed over the years and provide the basis for modern turbulence modeling. The process of developing these equations and the background theory is discussed next.

2.2.2 Turbulent Boundary Layer, Prandtl Mixing Length Theory, and Wall Coordinates

The most simple example of a turbulent boundary layer is perhaps that of external flow in one direction over a flat plate. In the case of purely x-direction flow only the y-direction gradients normal to the plate are considered, with the stream-wise gradient negligible except in cases of a stagnation point or boundary-layer separation. Equation 2.11 is then rewritten for this scenario (with the shear stress utilizing Newton's law of viscosity) as

$$\bar{u}\frac{\partial\bar{u}}{\partial x} + \bar{v}\frac{\partial\bar{u}}{\partial y} = -\frac{1}{\rho}\frac{d\bar{P}}{dx} + \frac{\partial}{\partial y}(\nu\frac{\partial\bar{u}}{\partial y} - \overline{u'v'}) \tag{2.13}$$

(where ν is simply the kinematic viscosity, μ/ρ). The term $\overline{u'v'}$ is then the apparent turbulent shear stress, and should approach zero if no gradient is present in the mean velocity profile, same as the viscous shear stress. A proportionality factor ε_M, known as the eddy diffusivity for momentum, can then be defined as a proportionality factor such that $\overline{u'v'}$ is equivalent to $\varepsilon_M\frac{\partial\bar{u}}{\partial y}$. Substitution into Equation 2.13 leads to the last term becoming $\frac{\partial}{\partial y}\left[(\nu+\varepsilon_M)\frac{\partial\bar{u}}{\partial y}\right]$. In most cases, by analysis, it is found that ε_M is dominant in fully turbulent regions while ν is dominant close to the wall.

Using this concept and knowledge of the gradients, Prandtl posited a mixing length, which was defined as "... the distance traversed by a mass of this type before it becomes blended in with neighbouring masses..." [16]. That is to say, there is some small length l_m a fluid packet travels, over which it retains some history of its previous condition, until blending with its surroundings. The associated eddy viscosity can then be written in terms of this mixing length and the gradient as

$$\nu_t = l_m|u'| \tag{2.14}$$

in general, where $|u'|$ is a measured quantity. For a one dimensional case as described, eddy viscosity can also be determined as

$$\nu_t = {l_m}^2 \left| \frac{\partial \bar{u}}{\partial y} \right| \tag{2.15}$$

For the region close to the wall where boundary layer interactions of the nature described by Prandtl occurs, it is also useful to form a new coordinate system, as local length scales are drastically different from global length scales in most cases. First, the total shear stress, the combination of molecular turbulence, is expressed as

$$\frac{\tau}{\rho} = (\nu + \nu_t)\frac{\partial \bar{u}}{\partial y} \tag{2.16}$$

using the definition of ν_t and the viscosity coefficient. Substitution into $\frac{\partial}{\partial y}\left[(\nu + \nu_t)\frac{\partial \bar{u}}{\partial y}\right]$ and Equation 2.13, along with multiplying through by ρ, yields

$$\rho\bar{u}\frac{\partial \bar{u}}{\partial x} + \rho\bar{v}\frac{\partial \bar{u}}{\partial y} = -\frac{d\bar{P}}{dx} + \frac{\partial \tau}{\partial y} \tag{2.17}$$

Under a Couette flow assumption near the wall, $\rho\bar{u}\frac{\partial \bar{u}}{\partial x}$ is much smaller than the other terms and is not considered. This is a generally valid assumption for up to one third of the boundary layer, far larger than the small viscous sublayer considered here. Thus, for unidirectional flow as in this scenario, $\bar{u}$ is considered a function of y alone and does not significantly change along the x direction of flow. Equation 2.17 can be integrated from $y = 0$ to any y within this region, where $\tau = \tau_w$ and $\bar{u} = 0$ by the no-slip viscous condition at the wall, resulting in

$$\frac{\tau}{\tau_w} = 1 + \frac{\rho v_w \bar{u}}{\tau_w} + \frac{d\bar{P}}{dx}\frac{y}{\tau_w} \tag{2.18}$$

The normal velocity $\bar{v}$ at the wall $\bar{v}_w$ can normally be assumed to equal zero in the absence of suction or blowing. This equation then relates shear at any point in this fluid region to shear at the wall, with τ/τ_w approaching zero at the edge of the boundary layer. Finally, using the definition of the skin friction coefficient

$$C_f = \frac{\tau_w}{\frac{1}{2}\rho u^2{}_\infty} \tag{2.19}$$

where u_∞ is the free-stream velocity, a shear velocity u_τ can be defined as

$$u_\tau = \sqrt{\tau_w/\rho} \tag{2.20}$$

Since u_τ has units of velocity, it can be considered a characteristic velocity by which to non-dimensionalize the other quantities in Equation 2.18 and form a new non-dimensional coordinate system in terms of wall and free-stream conditions. These are:

$$\begin{aligned} u^+ &= \frac{\bar{u}}{u_\tau} \\ y^+ &= \frac{y u_\tau}{\nu} \\ {v_w}^+ &= \frac{v_w}{u_\tau} \\ p^+ &= \frac{\mu d\bar{P}/dx}{\rho^{1/2}{\tau_w}^{3/2}} \end{aligned} \tag{2.21}$$

and τ/τ_w can be solved as τ^+ with

$$\tau^+ = 1 + {v_w}^+ u^+ + p^+ y^+ \tag{2.22}$$

For the region extremely close to the wall under Couette flow assumptions, and where p^+ and ${v_w}^+$ are zero, $\tau^+ = 1$. By integration of Equation 2.16 under these assumptions, and with substitutions of definitions from Prandtl mixing length theory as well as the wall coordinate definitions, the ”law of the wall” is obtained:

$$u^+ = 2.44 \ln y^+ + 5.0 \tag{2.23}$$

Comparisons with experimental data leads to a two-layer model for describing the effective sublayer thickness in terms of y^+ and u^+. At small y^+ (less than about 5.0), there can be an approximation of $u^+ = y^+$, while at greater y^+ the law of the wall is used.

2.2.3 k, ε and ω

Another approach to turbulence modeling relies on the turbulence kinetic energy k in substitution of ν_t from the Prandtl mixing length model. While Prandtl mixing length theory assumes that turbulent eddies do not interact with each other and are instead discrete molecules, this method presents that idea that more energetic turbulence will result in greater momentum exchange. The turbulence kinetic energy is defined in tensor notation as

$$k = \frac{1}{2}\overline{{u_i}'{u_i}'} \tag{2.24}$$

Thus, by substituting into Equation 2.14, ν_t can now be treated as $l_m\sqrt{k}$. An additional variable ω can also be used together with k in order to model ν_t. This variable ω is known as the specific dissipation rate and is proportional to u/l_m such that ν_t can also be expressed as

$$\nu_t = k/\omega \tag{2.25}$$

Similarly, the turbulence dissipation rate ε is also often substituted into these equations so that

$$\varepsilon = \nu \overline{\frac{\partial {u_i}'}{\partial x_j}\frac{\partial {u_i}'}{\partial x_j}} \tag{2.26}$$

The k term and combinations with ε and ω serve as the basis for the majority of one-equation and two-equation models. Turbulence kinetic energy k may be solved solely by itself in a one-equation model, or as a $k - \varepsilon$ or $k - \omega$ two-equation model. For example, a one dimensional Couette flow in the case of constant fluid properties, similar to Equation 2.13, may be modeled with a two-equation $k - \varepsilon$ approach as

$$\bar{u}\frac{\partial \bar{k}}{\partial x} + \bar{v}\frac{\partial \bar{k}}{\partial y} = \frac{\partial}{\partial y}\left[(\nu + \varepsilon_k)\frac{\partial \bar{k}}{\partial y}\right] + \varepsilon_M(\frac{\partial \bar{u}}{\partial y})^2 - \varepsilon \tag{2.27}$$

$$\bar{u}\frac{\partial \varepsilon}{dx} + \bar{v}\frac{\partial \varepsilon}{dy} = \frac{\partial}{\partial y}\left[(\nu + \varepsilon_\varepsilon)\frac{\partial \varepsilon}{\partial y}\right] + C_1\frac{\varepsilon}{\bar{k}}\left[\varepsilon_M(\frac{\partial u}{\partial y})^2\right] - C_2\frac{\varepsilon^2}{\bar{k}} \tag{2.28}$$

where ε_k is the eddy diffusivity for turbulence kinetic energy transport, defined experimentally in proportion to ε_M, C_1 and C_2 are constants, and ε_ε is the turbulent transport of ε and proportional to ν_t. In this case, $\bar{k}$ is also considered a quantity proportional to ε and ν_t and determined somewhat empirically. Thus, if a solution is obtained for both the $\bar{k}$ and ε equations, ε_M can be determined.

For a more detailed consideration of these models and turbulence theory as described in this thesis, see Reference [17].

2.3 Solver

Tenasi, an unstructured three-dimensional CFD solver developed by the University of Tennessee at Chattanooga SimCenter and maintained by researchers at Auburn University, was used for the research presented in this thesis. It is a node-centered, finite volume package with a variety of flow regimes modeled including both incompressible and compressible schemes. Inviscid fluxes are solved using a Roe [18] or HLLC [19] method. A variety of turbulence models are available, including both one equation and two equation models. Both steady-state and time-accurate modes, including second order temporal accuracy, are available within the solver. Up to 7th order spatial accuracy is also able to be achieved by implementation of a specialized form of the WENO stencil [20].

Additionally, *Tenasi* features a DES (Detached Eddy Simulation) mode with sub-grid scale modeling. Pure RANS models tend to model wall flow well, but overly dissipate flow features away from such regions, as in the free-stream. LES (Large Eddy Simulation) offers an alternative to this with non wall-bounded features resolved well. However, a pure LES solution requires much more refinement in this region to adequately resolve the solution and is thus more computationally expensive. In addition, the flow near the wall cannot be fully resolved and thus must be modeled. With the DES feature in *Tenasi* and many other solvers, areas close to no-slip walls retain the accuracy of RANS simulations while cells in the freestream, far away from walls, take advantage of LES calculations. This provides a relatively less computationally expensive method of solving compared to a full LES simulation and proper resolution of features near the wall, akin to a RANS simulation. This mode in *Tenasi* additionally allows for ”sub-grid scale” modeling whereby the solution is not limited by the length scale of the grid and can instead allow for flow features to define turbulence length scales.

Previous studies of heavy trucks have been done using *Tenasi* and these features, most notably DES coupled with the blended $k - \varepsilon, k - \omega$ SST turbulence model, to much success [7, 21, 22]. Because of these validation cases, coupled with validation work done by the author of this thesis regarding preservation of small-scale vortex features using this approach [23], the incompressible RANS scheme with DES and the blended $k - \varepsilon, k - \omega$ SST turbulence model was used for the results presented in this thesis. The next sections describe the implementations of these features in *Tenasi*.

2.3.1 *Tenasi* Unsteady Incompressible 3D RANS

The incompressible unsteady three-dimensional Reynolds-averaged Navier-Stokes equations [24] used in this thesis are briefly presented in Cartesian coordinates and in conservative form as

$$\frac{\partial}{\partial t}\int_{\Omega} Q d\mathcal{V} + \int_{\partial\Omega} \vec{F} \cdot \hat{\vec{n}} dA = \int_{\partial\Omega} \vec{F}_v \cdot \hat{\vec{n}} dA \tag{2.29}$$

where $\hat{\vec{n}}$ is the outward pointing unit normal to the control volume $\mathcal{V}$. The vector of dependent variables and the components of the inviscid and viscous flux vectors are given as

$$Q = \begin{bmatrix} P \\ u \\ v \\ w \end{bmatrix} \tag{2.30}$$

$$\vec{F} \cdot \hat{\vec{n}} = \begin{bmatrix} \beta\left(\Theta - a_t\right) \\ u\Theta + \hat{n}_x P \\ v\Theta + \hat{n}_y P \\ w\Theta + \hat{n}_z P \end{bmatrix} \tag{2.31}$$

$$\vec{F}_v \cdot \hat{\vec{n}} = \begin{bmatrix} 0 \\ \hat{n}_x \tau_{xx} + \hat{n}_y \tau_{xy} + \hat{n}_z \tau_{xz} \\ \hat{n}_x \tau_{yx} + \hat{n}_y \tau_{yy} + \hat{n}_z \tau_{yz} \\ \hat{n}_x \tau_{zx} + \hat{n}_y \tau_{zy} + \hat{n}_z \tau_{zz} \end{bmatrix} \tag{2.32}$$

where β is the artificial compressibility parameter, u, v, and w are the Cartesian velocity components in the x, y, and z directions, and $\hat{n}_x$, $\hat{n}_y$, and $\hat{n}_z$ are the components of the normalized control volume face vector. Θ is the velocity normal to a control volume face:

$$\Theta = \hat{n}_x u + \hat{n}_y v + \hat{n}_z w + a_t \tag{2.33}$$

where the grid speed $a_t = -\left(V_x \hat{n}_x + V_y \hat{n}_y + V_z \hat{n}_z\right)$. Notice that $\vec{V_s} = V_x \hat{i} + V_y \hat{j} + V_z \hat{k}$ is the control volume face velocity. The variables in the preceding equations are normalized with respect to a characteristic length scale (L_r) and reference values of velocity (U_r), density (ρ_r), and viscosity (μ_r). Thus, the Reynolds number is defined as $Re = \rho_r U_r L_r / \mu_r$. Pressure is normalized with $P = \left(P^* - P_\infty\right) / p_r {U_r}^2$ where P^* is the local dimensional static pressure.

When using eddy viscosity, the stresses given in Equation 2.32 are

$$\tau_{ij} = \frac{(\nu + \nu_t)}{Re_L}\left(\frac{\partial u_i}{\partial x_j} + \frac{\partial u_j}{\partial x_i}\right) \tag{2.34}$$

where μ and μ_t are the molecular and eddy viscosities, respectively and $\tilde{\tau}_{ij}$ are the Reynolds stresses.

2.3.2 Blended $k-\epsilon$, $k-\omega$ Turbulence Model

The non-dimensionalized $k-\epsilon, k-\omega$ turbulence model [25] used in this study is expressed as

$$\frac{\partial}{\partial t}\int_{\Omega}\rho k d\mathcal{V} + \int_{\partial\Omega}\rho k \Theta dA = \frac{1}{Re}\int_{\partial\Omega}(\mu + \sigma_k\mu_t)\,\overrightarrow{\nabla k}\cdot\hat{\vec{n}}dA + \mathcal{V}\left[P - \frac{\rho k^{3/2}}{l_t} + (1-F_1)\,\overline{p''d''}\right] \tag{2.35}$$

$$\begin{aligned}&\frac{\partial}{\partial t}\int_{\Omega}\rho\omega d\mathcal{V} + \int_{\partial\Omega}\rho\omega\Theta dA = \\ &\quad\frac{1}{Re}\int_{\partial\Omega}(\mu + \sigma_\omega\mu_t)\,\overrightarrow{\nabla\omega}\cdot\hat{\vec{n}}dA \\ &\quad+\mathcal{V}\left[\frac{\delta\omega}{k}P - \beta\rho\omega^2 + (1-F_1)\,\beta^*\alpha_1 {M_t}^2\rho\omega^2 + 2\rho\,(1-F_1)\,\sigma_{\omega 2}\frac{1}{\omega}\overrightarrow{\nabla k}\cdot\overrightarrow{\nabla\omega} - (1-F_1)\,\frac{\overline{p''d''}}{\nu_t}\right]\end{aligned} \tag{2.36}$$

where $\rho = 1.0$ is used for this incompressible study and the eddy viscosity, production, turbulent length scale, and pressure dilatation terms are defined as

$$\mu_t = Re_L\frac{\rho k}{\omega} \tag{2.37}$$

$$P = \frac{\rho k}{\omega}\left(2S_{ij}S_{ij} - \frac{2}{3}\left(\nabla\cdot\vec{u}\right)^2\right) - \frac{2\rho k}{3}\left(\nabla\cdot\vec{u}\right) \qquad S_{ij} = \frac{1}{2}\left(\frac{\partial u_i}{\partial x_j} + \frac{\partial u_j}{\partial x_i}\right) \tag{2.38}$$

$$\overline{p''d''} = -P\alpha_2{M_t}^2 + \alpha_3\rho\epsilon{M_t}^2 \tag{2.39}$$

$$l_{k\omega} = \frac{\sqrt{k}}{\omega\beta^*\left[1 + \alpha_1{M_t}^2\,(1-F_1)\right]} \tag{2.40}$$

$$l_t = \begin{cases} l_{k\omega} & : \text{RANS mode} \\ \frac{a_2\sqrt{k}}{D_l} & : \text{DES mode}\end{cases} \tag{2.41}$$

$$D_l = \max\left(a_2\omega\beta^*\left[1+\alpha_1{M_t}^2\left(1-F_1\right)\right], F_3\sqrt{2S_{ij}S_{ij}}, F_4\frac{a_2\sqrt{k}}{C_{DES}\Delta_{max}}\right) \tag{2.42}$$

and $C_{DES} = 0.65$, Δ_{max} is the local maximum node-to-node distance, ${M_t}^2 = 2k/c^2$, $\epsilon = c_\mu k\omega$, $c_\mu = 0.09$, $\alpha_1 = 1.0$, $\alpha_2 = 0.4$, $\alpha_3 = 0.2$, and $a_2 = 2.5$.

The definition of l_t in Equation 2.41 is modified from its original version [25]. The addition of two new blending functions and the use of the local strain-rate invariant completes the new definition of l_t. The strain-rate invariant is used to allow local flow features to govern the turbulent length scale instead of grid spacing, and the blending functions F_3 and F_4 are basic attempts to reduce the grid sensitivity of DES models by blending between RANS and DES regions instead of abruptly changing regions. The new functions are defined as $F_3 = tanh\left({\varphi_3}^2\right)$ and $F_4 = tanh\left({\varphi_4}^2\right)$ where $\varphi_3 = d_v/\left(C_{DES}\Delta\right)$, $\varphi_4 = \varphi_3/2$, and d_v is the distance to the viscous surface. Although rudimentary in nature, these modifications are quite effective in reducing sudden grid induced changes. Development is ongoing to define more inclusive and robust switching parameters.

The blending function F_1 is defined as $F_1 = tanh\left(\varphi^4\right)$ where

$$\varphi = \min\left(\max\left(\frac{\sqrt{k}}{0.09\omega d_v}, \frac{500\mu}{\rho\omega {d_v}^2}\right), \frac{4\rho\sigma_{\omega 2}}{D_{k\omega}{d_v}^2}\right) \tag{2.43}$$

$$D_{k\omega} = \max\left(2\rho\sigma_{\omega 2}\frac{1}{\omega}\overrightarrow{\nabla k}\cdot\overrightarrow{\nabla\omega}, 10^{-14}\right) \tag{2.44}$$

F_1 is used to blend the model constants between the $k-\omega$ and $k-\epsilon$ regions of the flow using $\phi = F_1\phi_1 + \left(1-F_1\right)\phi_2$ where ϕ_1 and ϕ_2 are general constants for the $k-\omega$ and $k-\epsilon$ regions respectively.

Chapter 3

Solution Methodology

The work involved in a full CFD simulation can be roughly sorted into three categories. The first of these is the task of pre-processing, involving the development of physical models and generation of discretized surface and volumetric meshes in order to conduct calculations. The second of these then is the actual solution stage, whereby a solution is calculated for a given set of initial and boundary conditions imposed upon the aforementioned mesh, as well as for a set of CFD solver parameters. This is where methods such as RANS vs LES or DES, and a choice of turbulence model, come into play. Finally, there is the post-processing step whereby the results from the CFD solver are ported into visualization software for interpretation and inspection. The details of both pre-processing and the setup of the simulation are presented in the following sections.

3.1 CAD Models

The CAD models used for this thesis were based on the Peterbilt 579 tractor, pictured in Figure 3.1. The model itself started in a form presented in previous Auburn University work [10] with smaller-scale features such as mirrors removed for simplification of the geometry. The model was still deemed adequate for capturing larger scale features, as has been the focus of truck platoon studies. A major difference for this thesis however was the modeling of distinct wheels on both the truck and trailer, whereas the previous works had featured a blended, solid wheel well and wheel assembly. This blended approach reduced model complexity, but did not allow for proper rotational conditions on the wheels and thus was modified. The original version is shown in Figure 3.2, with the updated version in Figure 3.3.

Figure 3.1: Image of Peterbilt 579 truck [26]

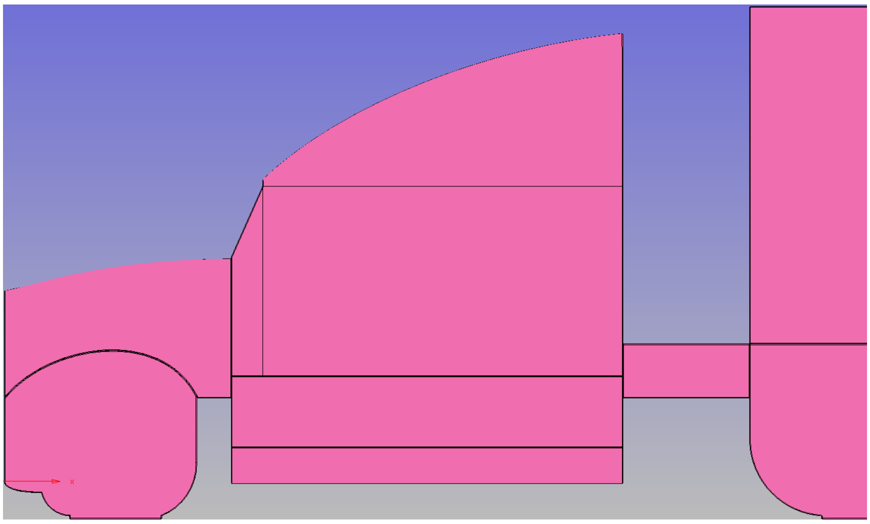

Figure 3.2: Peterbilt 579 model as featured in previous Auburn University studies [9, 10, 27]

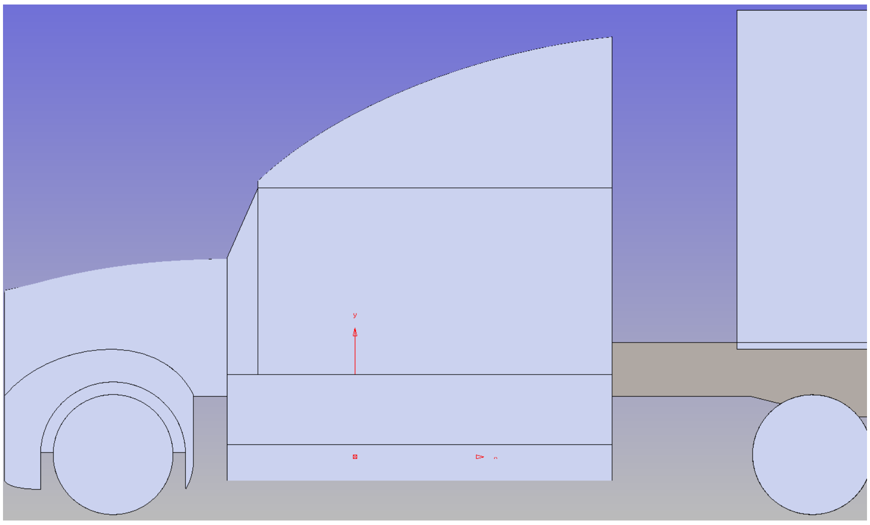

Figure 3.3: Peterbilt 579 model used in this study

Several versions of trailer loads were also created to accompany the truck model. The standard 53 ft. box trailer used in previous studies was adapted to also include free wheels for implementation of a rotation condition. However it was not significantly altered otherwise. Three variations of a flatbed trailer were also created. One version featured a completely unloaded trailer, the second featured a centered 20 ft. shipping container, and the third featured the trailer fully loaded with two shipping containers. One point of note is that the CAD models for these shipping containers do not feature corrugation like their real-world counterparts, and instead are modeled with smooth surfaces analogous with the box trailer. This was partly done to ease complications with grid generation in subsequent steps, as models featuring corrugation added a significant amount of points to the grids. Comparisons between forces on smooth containers and corrugated shipping containers had been done previously and little difference was found in measured forces or overall flow features, aside from at the corrugations themselves. All models featured the same Peterbilt 579 truck model. It should be noted that there is some level of resolution disparity between the underbody of the flatbed trailer and the box trailer, with the former featuring more detail, including a semblance of axles. These differences are not severe however, and overall both trailer types feature the same general level of fidelity. Depictions and dimensions of all these models are shown in Figures 3.4 - 3.8.

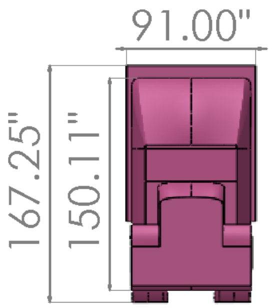

Figure 3.4: Peterbilt 579 model with box trailer, front view

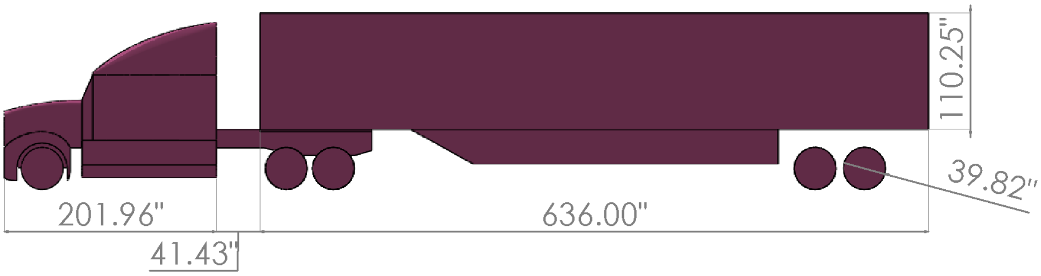

Figure 3.5: Peterbilt 579 model with box trailer, side view

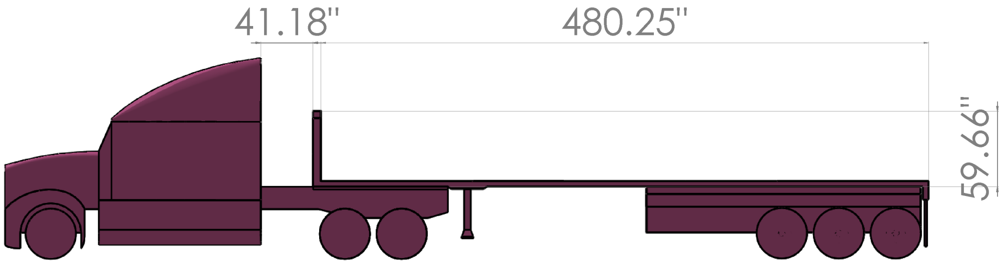

Figure 3.6: Peterbilt 579 model unloaded flatbed trailer

3.2 Grid Generation

While the CAD models serve as a model of real geometry, they are not a sufficient end model for a CFD study. In order to properly be interpreted by a solver, a number of discrete surface meshes must be constructed using the CAD model as a template and guideline. Further, volumetric elements must also be built off of these surfaces for 3D finite volume simulations. While these two steps may seem basic, there is much room for introduced error and thus may lead to inexact, or indeed wholly divergent, solutions.

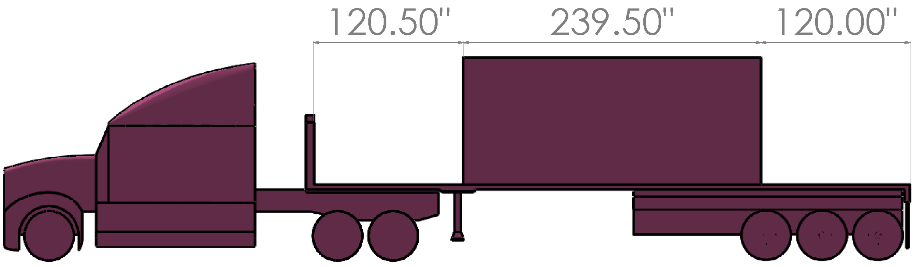

Figure 3.7: Peterbilt 579 model with centered 20 ft. shipping container

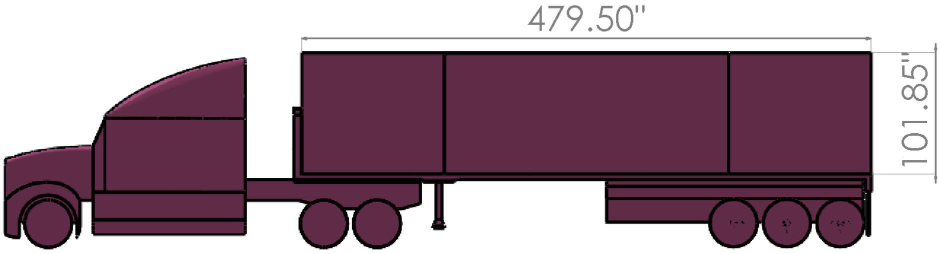

Figure 3.8: Peterbilt 579 model with full shipping container load

Three major problems are universal for the transformation of CAD geometry to a CFD-ready, discretized grid. The first of these is inherent to the way that CAD geometries are constructed, especially with regards to intersections of surfaces. While in a CAD modeling program these surfaces seem to be completely closed, there is often a small gap present in actuality due to non identical placement of sampling points for each surface at the intersection. This means that the surfaces are not “watertight” and therefore a proper volumetric grid cannot be generated. This requires much effort on the part of the user to clean these geometries, and patches are sometimes not as exact as presented by the CAD model.

The second and third major problems involve proper refinement of the surface meshes and volumetric elements themselves. There is a careful balance to be struck between having a computationally light, but inadequate coarse grid and an intractable, overrefined grid. This also affects the skewness of volumetric cells where cells are generally quite ”flat”, causing problems in calculating fluxes across the faces. This can have disastrous effects on a CFD solution by leading to severe convergence issues. For this thesis, grid refinement was based upon previous studies of this nature [7, 10, 21], SAE J2966 guidelines for CFD modeling of heavy commercial ground vehicles [29], and governed by limitations within the meshing software itself.

3.2.1 Surface Mesh Generation

Pointwise, a commercial grid generation software package, was used for both surface mesh generation and the full 3D volume grid. The CAD model was first imported into the software to be used as a template and then edges were represented by discretized curves, allowing for

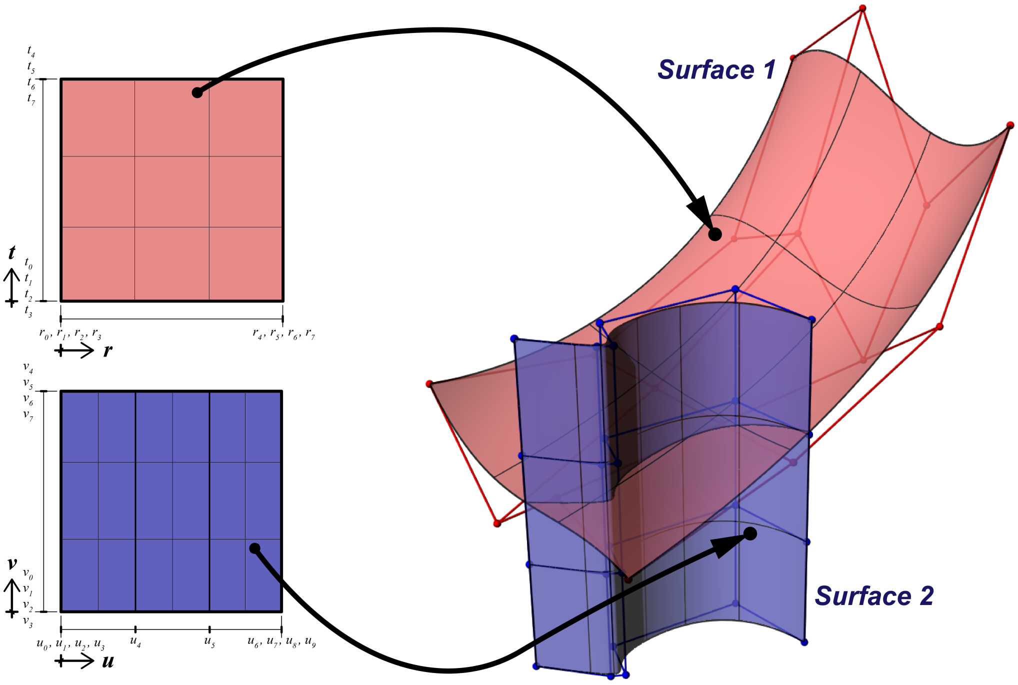

NURBS Surfaces: Parameter Space and Model Space

Figure 3.9: Example of an intersection between two surfaces and the lower order curves approximating each surface [28]

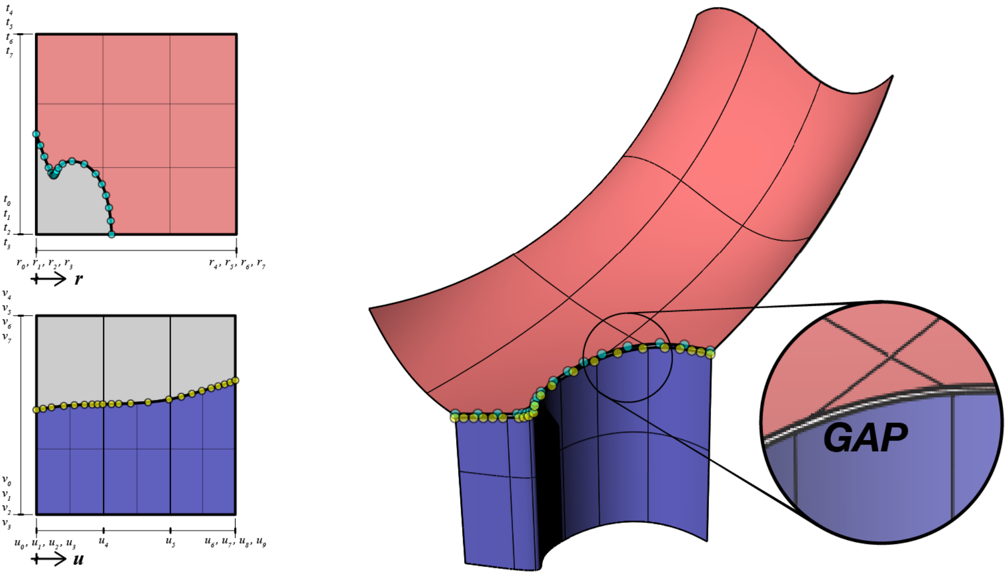

Approximated Curves From SSI Sampling Points

Figure 3.10: Example of a surface-surface intersection (SSI) where non-identical sampling points cause a gap between surfaces when imported into a mesh generation package [28]

variable levels of refinement at different sections of each vehicle. During this stage, much work was also done in order to fix non-watertight intersections and provide a solid model to build a proper volumetric mesh around. Figures 3.9 and 3.10 show an example of where a non-watertight model is created from intersections on a CAD model. Surfaces are either extended by the user in Pointwise to cover such gaps or an arbitrary surface mesh is wrapped around. An advancing front algorithm within Pointwise (known as “advancing front ortho”) was used for marching triangular elements off the edges. This provided the ability to keep higher refinement confined to surface edges and with higher quality cells, while also easing difficulties in transition to the non wall-bounded areas of the surface mesh.

Surface mesh refinement was determined using the refinements presented in Humphreys’ work [10] on the box trailer model as a baseline. Additional refinement was used along the sharp edges on the vehicles. Additionally, surface meshes were much further refined during the course of this study than those presented by Humphreys. Whereas average cell sizes in Humphrey’s work was typically between 10-15 inches, the average cell size used in this thesis ranged from 1.3 - 3.0 inches in the fully triangular surface meshes created by the user. During volume cell generation, a number of these surface mesh elements were also recombined into quadrilateral elements (mostly for cells not at surface intersections) and the final surface meshes yielded even further refined features. Table 3.1 describes the typical edge length ranges and average edge length for all vehicle models.

Configuration	**Min (Combined)**	**Max (Combined)**	**Average (Combined)**
Box Trailer	0.0846 (0.0846) in	13.147 (10.835) in	3.00 (2.735) in
Full Shipping	0.01659 (0.01659) in	10.442 (8.378) in	1.5068 (1.359) in
Centered Shipping	0.01659 (0.01659) in	9.985 (8.572) in	1.4406 (1.288) in
Unloaded Flatbed	0.01659 (0.01659) in	9.949 (7.8242) in	1.3656 (1.226) in

Table 3.1: Edge length values for cells in surface meshes on the various vehicle combinations. Values in (Combined) represent cells after undergoing combination in full grid generation

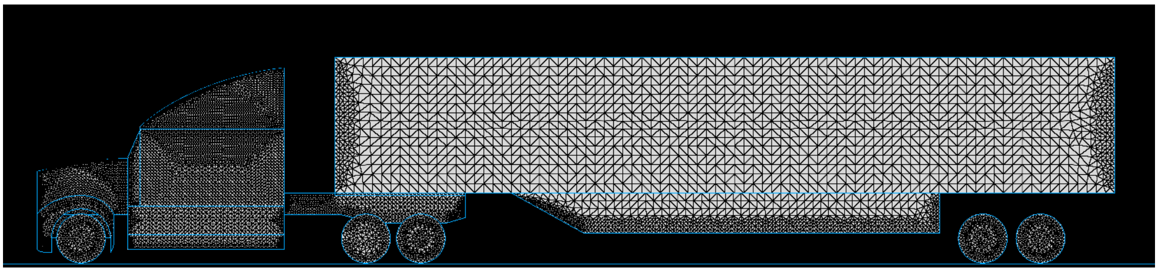

Figure 3.11: Initial fully-triangular surface mesh for the box trailer configuration

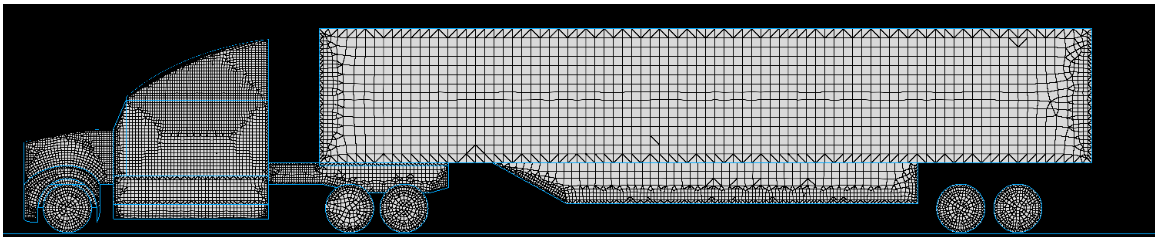

Figure 3.12: Mixed triangular and quadrilateral element surface mesh for box trailer configuration after volume grid generation

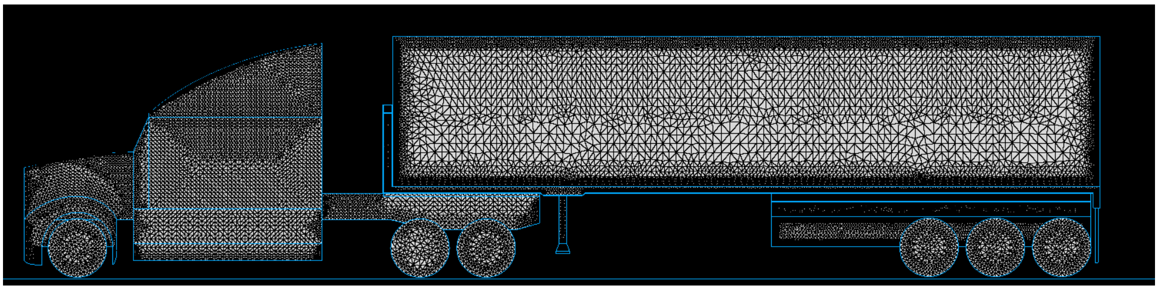

Figure 3.13: Initial fully-triangular surface mesh for the full shipping container trailer configuration

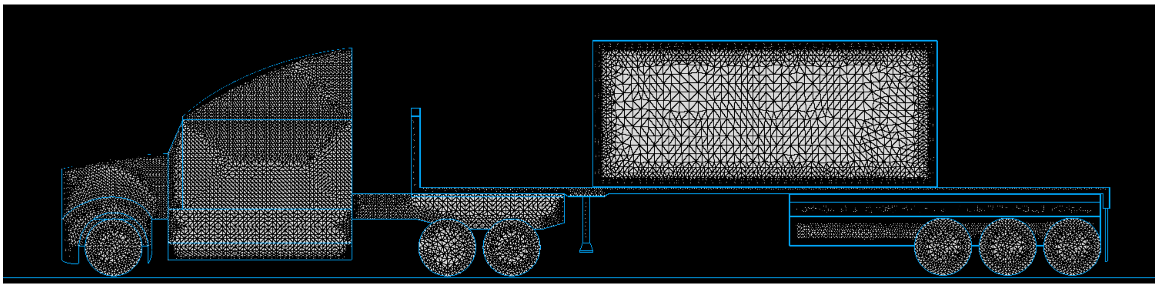

Figure 3.14: Initial fully-triangular surface mesh for the centered shipping container trailer configuration

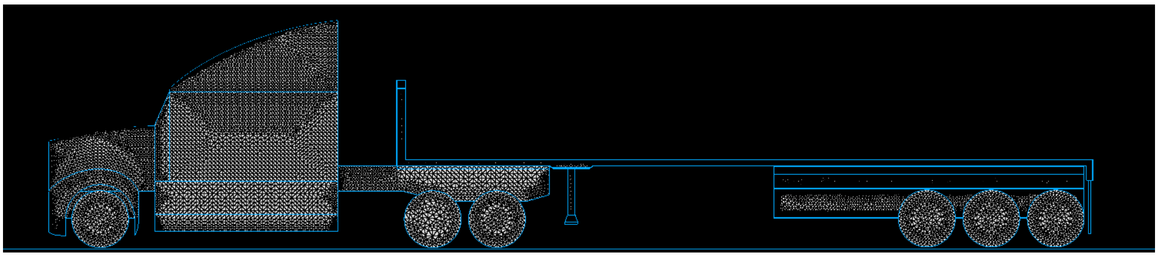

Figure 3.15: Initial fully-triangular surface mesh for the unloaded flatbed trailer configuration

3.2.2 Volumetric Grid Generation

A rectangular box was constructed around the vehicle models and platoon models in order to generate a volume grid. This box had dimensions of at least 4x the largest trailer width on either side of the vehicles, 5x the largest trailer height above the vehicles, 2x the largest trailer length in front of the vehicles, and 7x the largest trailer length rear of the vehicles. The domain beneath the tires was also offset 1.0 inch in order to properly facilitate element growth between itself and the tire domains. It was not possible to model a contact point between the ground and wheels due to the rotation condition implemented in *Tenasi*.This groundplane domain also featured a more refined cutout around each vehicle in order to increase point density in the near-field.

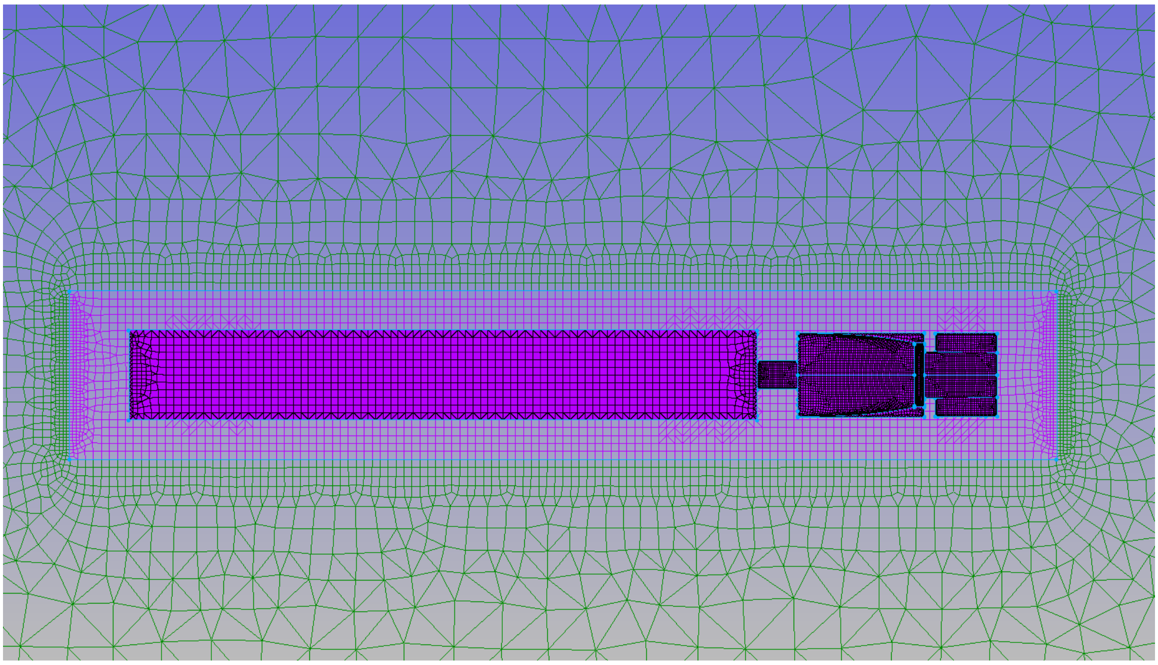

Figure 3.16: Refined groundplane around individual truck

Volume generation itself was done by propagating anisotropic elements outward normally from both the vehicles and the groundplane until a maximum number of layers is reached, or no further anisotropic elements can be created. The remainder of the volume grid is then populated with tetrahedral elements. The initial spacing for these anisotropic elements is governed by the chosen y^+ value and flow conditions, as in Equation 2.21. The trailer height of the box trailer was used for a reference length, rather than the length of the trailer, as this is fairly standard

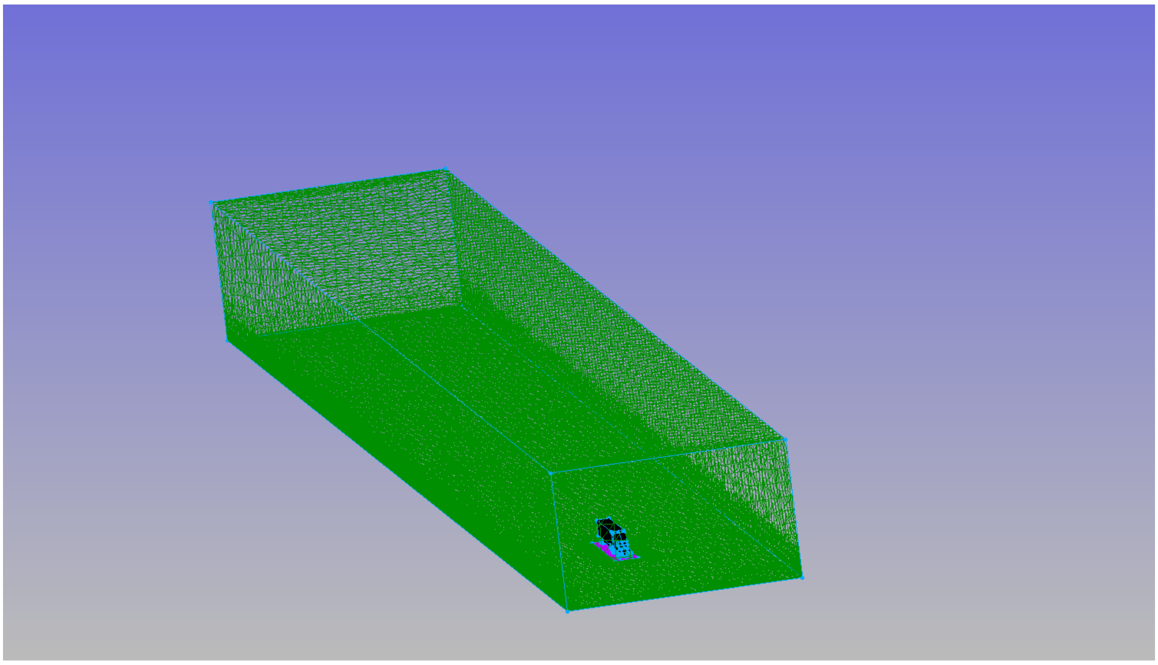

Figure 3.17: Farfield domain around single truck

practice. A y^+ of 5.0 was chosen, resulting in an initial wall spacing off the vehicles of about 0.003 inches. SAE vehicle modeling standards [29] recommend a y^+ between 1.0 - 5.0, but it was found that the Pointwise software had much trouble creating a valid grid around complex geometries for values closer to 1.0 . Anisotropic elements were also built off the groundplane in order to more effectively model the boundary layer. An initial spacing of 0.006 inches was used here, as this area does not typically need as much refinement as the vehicles themselves. In both cases, cells were grown at a rate of 1.3 until either a maximum of 25 layers was reached or cell growth could not continue. This growth rate is also reflective of issues encountered within Pointwise, where lower growth rates, even at an initial y^+ value of 5.0, resulted in cell generation errors by the software.

To provide additional refinement and somewhat compensate for having to use a higher growth rate for these anisotropic cells, the ”source” feature in Pointwise was also utilized around the vehicles. This feature allowed for tetrahedral cells built after the anisotropic layers and lying within the specified region to be constrained to a constant preferred size. In this case, 6.0 inches is chosen as the maximum cell edge length for the ”source” region. This refinement region spanned from about 5 ft in front of the vehicle to 2-3 vehicle lengths behind the vehicle, and was spanned about 4 ft in either lateral direction as well as at least about 7 ft above the vehicle. Final grids consisted then consisted of a mix of hexahedral, prismatic, and pyramid elements off the vehicles and ground, with small tetrahedral elements encompassing the near-field of the vehicle and larger tetrahedral elements filling the rest of the domain.

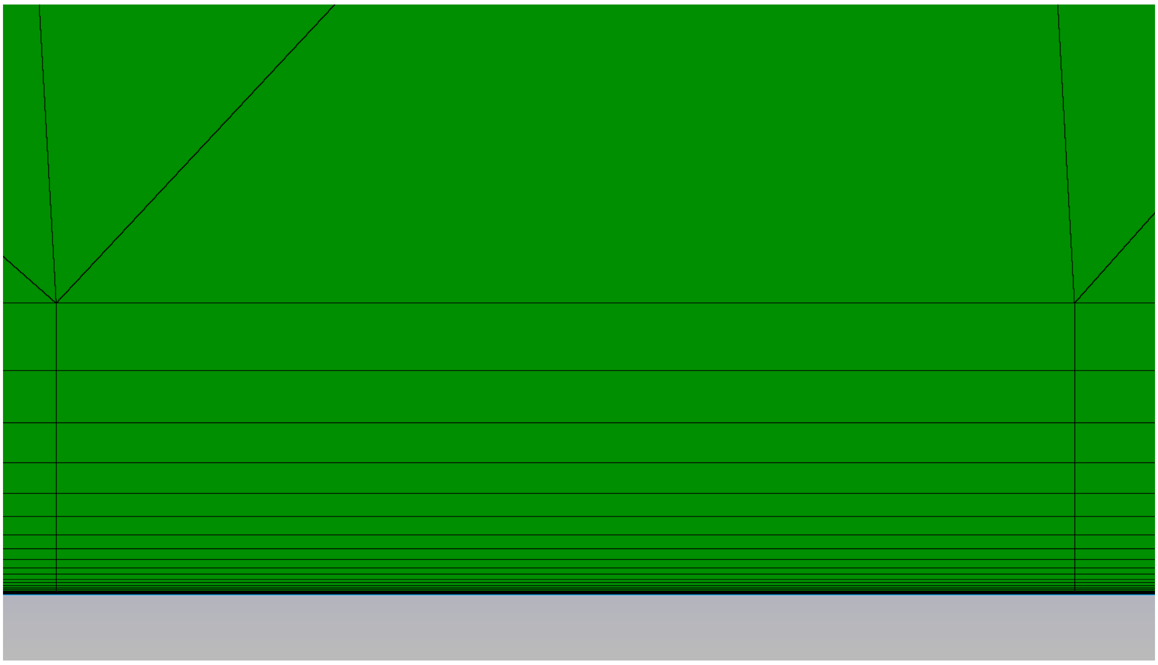

Figure 3.18: Depiction of anisotropic cell growth on farfield wall surface domain

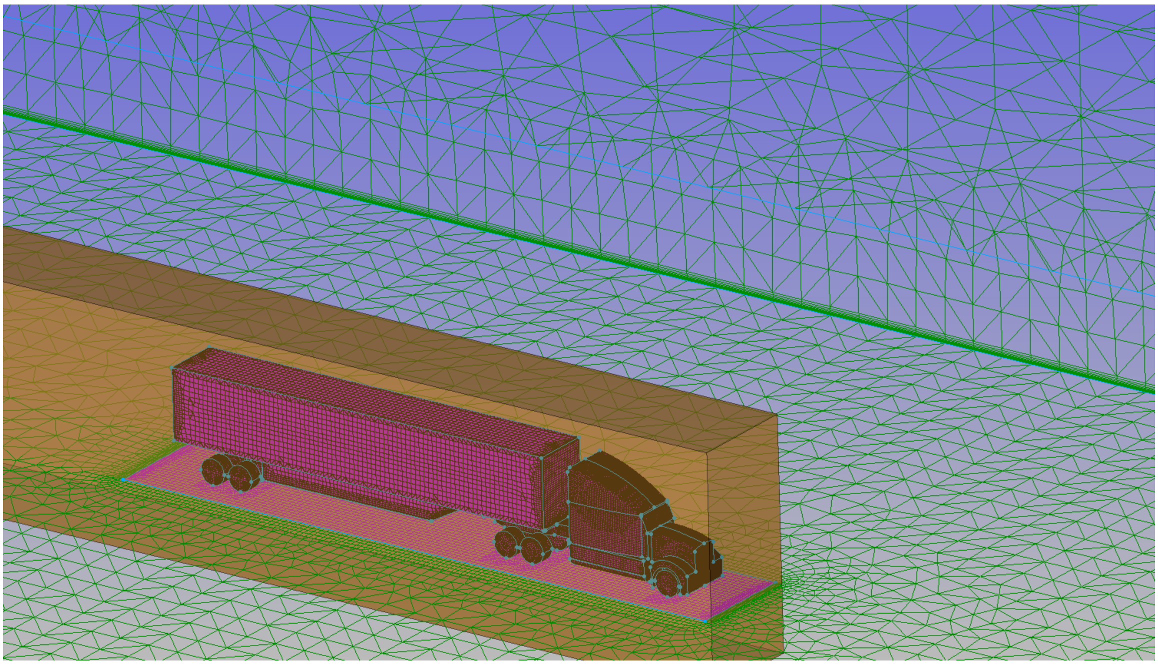

Figure 3.19: Depiction of the ”source” feature (in yellow) around the vehicle

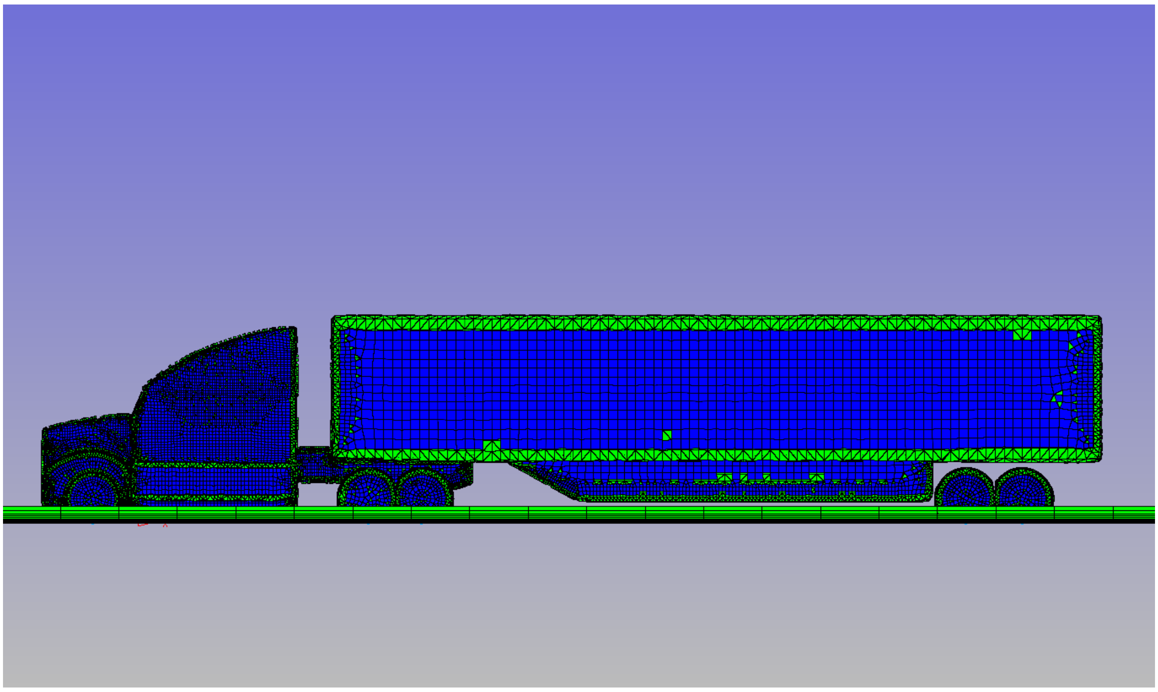

Figure 3.20: View of anisotropic elements built off of the vehicle and groundplane. Blue elements are hexes and green elements are prisms

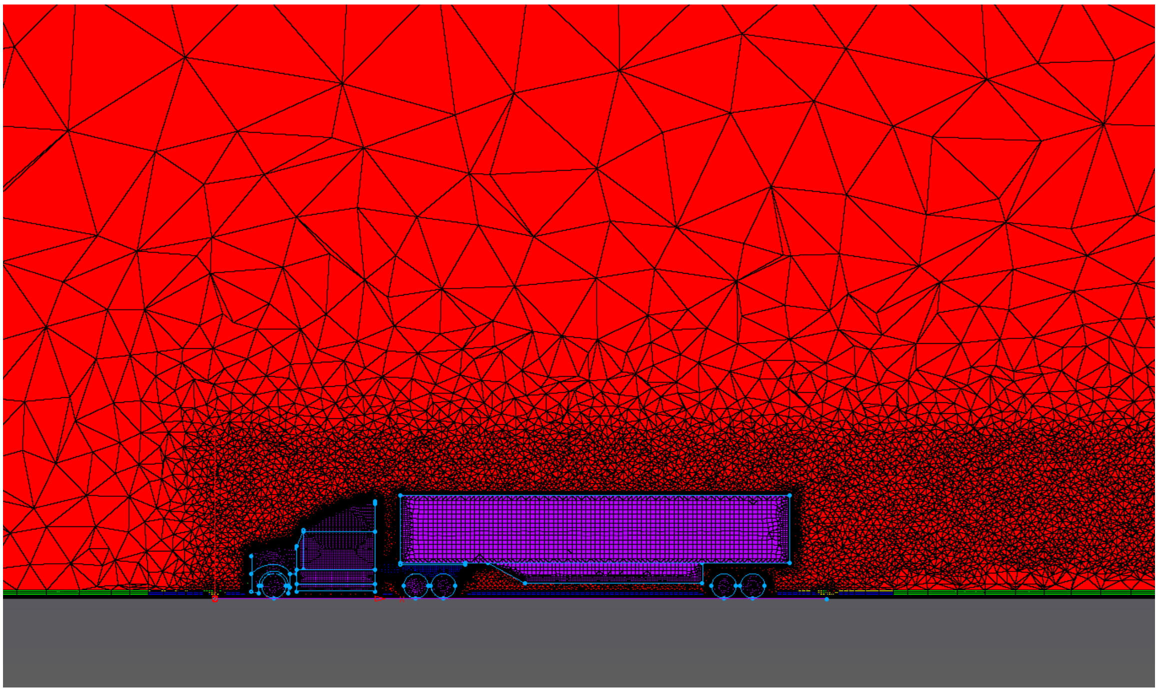

Figure 3.21: Slice of the volume grid around a single box trailer vehicle. Tetrahedral elements (red) are smaller in the area of the ”source” feature than outside. Near-body and near-groundplane regions contain all anisotropic elements as pictured in Figure 3.20

3.3 CFD Simulation

After creating the full grid for each case, the next step is to conduct the CFD simulation using an exported version of the grid. The exact process of running these simulations can be just as diverse as the grid generation stages, with many variables within any given solver affecting a solution in a multitude of different ways. CFD is an iterative process and thus the general idea is to achieve a stable solution with some level of convergence after a sufficient number of iterations. However, certain combinations of grid features and solver parameters can easily lead to spurious, or worse, divergent, solutions. Furthermore, it is not always possible to achieve machine-level precision convergence for all parameters depending on the case studied. Thus, in many cases it is sufficient to conclude a solution converged when fluctuations of parameters such as drag are, for a reasonable amount of iterations, lower than or within a range of specified tolerances.

3.3.1 Solver Parameters

As specified previously, the incompressible regime for *Tenasi* is used for these studies. All parameters within *Tenasi* are normalized to SI units, so there is some unavoidable mixed-unit use due to the nature of this work. Highway conditions of 65 mph are used in this study, and as such the top and side walls of the farfield as shown in Figure 3.17 are set with a freestream velocity farfield condition of about 29 m/s, equivalent to 65 mph. The groundplane is set as a viscous, no-slip surface with a translating condition of 29 m/s as well. Each vehicle is set as a viscous, no-slip surface while the wheels have an additional rotational velocity condition corresponding to a linear 29 m/s. Flow reference conditions are set using sea level standard atmosphere conditions, with a reference velocity specified as 29 m/s and a reference length of 2.8 m (corresponding to the height of the box trailer).

An initial steady state solution is used to establish the flow-field around the vehicles in a given scenario with a time-accurate solution following this in order to get a more accurate picture of the flow phenomena. 10,000 steady state iterations with 1st order spatial accuracy are first run, with the CFL (Courant-Friedrichs-Lewy) condition, a steady-state pseudo time-step parameter, increased from 1.0 to 5.0 over the first 5,000 iterations. A higher CFL lead to convergence issues in most cases. The DES feature begins at the next 5,000 iterations, and the following 5,000 iterations use 7$^{\text{th}}$ order spatial accuracy. Finally, 10,000 time-accurate iterations are run with a time step of $1.0E-04$ seconds at second order temporal accuracy. The Barth-Jespersen limiter is also utilized to aid the stability of the solution. The solution is considered to be converged at each stage of iterations when drag force achieves a fairly uniform value and residuals are within low fluctuations. The last 5,000 iterations of time-accurate runs are averaged to produce a final drag value, and the last 1,000 iterations are iteration-averaged by *Tenasi* in order to be viewed in post processing.

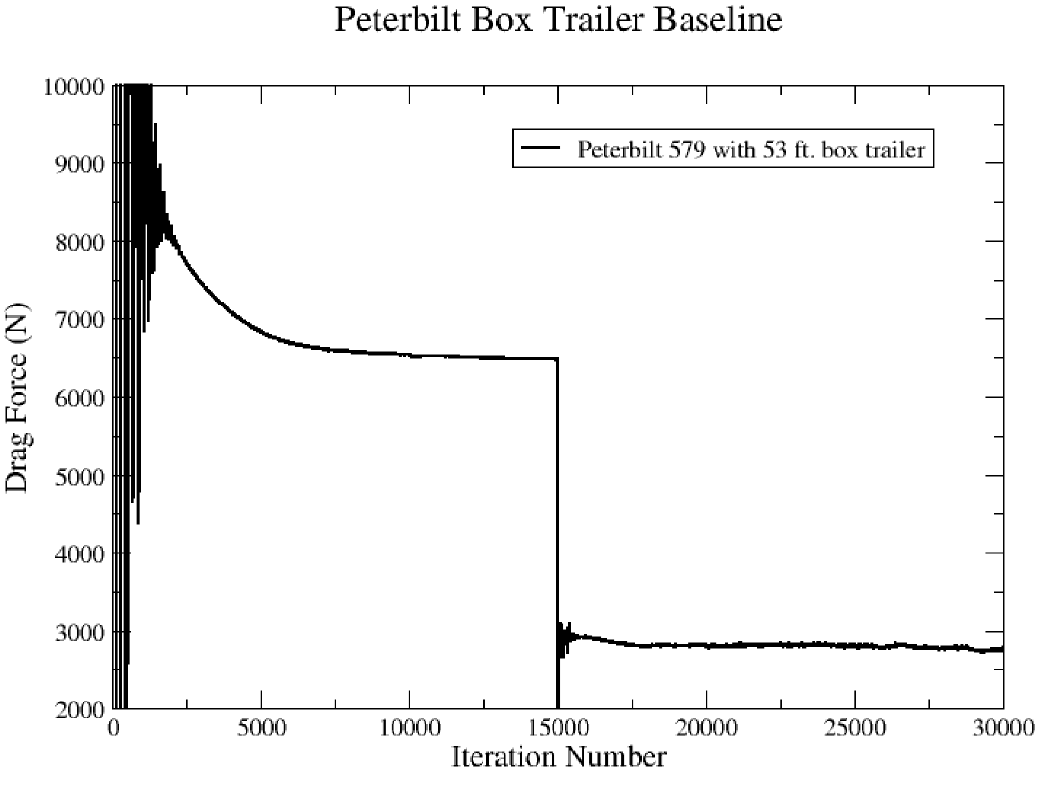

Figure 3.22: Typical example of drag force convergence for a CFD simulation

Solutions are run using Auburn University's High Performance Compute Cluster (HPCC) known as *Hopper*. *Hopper* consists of a total of 5888 cores, mainly comprised of nodes featuring 128 GB of memory and two Haswell CPUs each, at 10 cores/CPU. An overall 38 TB of RAM is available on *Hopper* and total computational speeds clock at about 250 TFlops. The grids themselves are decomposed into a number of partitions in order to spread out cases amongst compute nodes and limit computational overhead. The number of cores assigned to each case varies depending on the grid in question, but in general around 100,000 - 300,000 points are assigned to each partition.

3.3.2 Description of Cases

Three kinds of platooning cases are studied in this thesis. The first of these cases is the re-evaluation of the effects of lateral offset within a platoon of two homogeneous trucks at several small separation distances. As discussed previously, there has been some disagreement between results of previous CFD studies [10] which suggests that lateral offset has significant effects on frontal pressure drag for the tail vehicle, and a recent wind tunnel study [15] which suggests that lateral offset has little effect on platoon dynamics. It should be noted that for this thesis, there is no attempt to provide a sweep of yaw angles for the free-stream unlike the wind tunnel tests. While Humphreys' [10] CFD work did include some yaw sweep, it was also found that there was a noticeable effect at 0° yaw, and the variable yaw angles either produced more or less favorable results depending on the direction with respect to the lateral offset. Lateral offset distance for these cases in this thesis are presented as a percentage of the trailer width for 0%, 10%, 25% and 50% .

The second case studied in this thesis involves the variation of intra-platoon separation distance for a three truck homogeneous platoon. Previous studies of truck platoons have only considered platoons where the vehicle-to-vehicle separation distance is nominally identical throughout the whole of the platoon. While intuitively it may seem that this is the ideal and most logical way to form the platoon for maximizing drag reduction, it is still an important factor to consider. This is also partly due to the fact that controllers for the vehicles may not be uniformly rigid throughout the platoon and thus there is some level of drift around a proscribed separation distance. Therefore, it is beneficial to investigate the effects of this phenomena on the drag reduction.

The third case abandons the assumption of a fully homogeneous platoon, at least with regards to trailer loads. Depending on the mission of a platoon, and especially if platoons are formed dynamically from trucks already on a road, there is a greater chance of mismatched trailers within the platoon. This can be as relatively minor as a difference in trailer devices such as boattails like the case presented by the Canada-US joint study [11] discussed earlier in this thesis or as major as entirely different trailer types whatsoever. There exists a wide variety of trailer loads in the trucking industry and the selection described previously in this chapter provides a general sampling of these configurations. Four vehicle, fully heterogeneous platoons are formed from these loads with a variation in trailer load order to provide some insight into how these affect the platoon drag savings.

All cases are studied at a variety of separation distances and thus a large number of grids are constructed to cover these scenarios. A breakdown of typical grid properties for the cases is presented in Table 3.2. The scenarios for the heterogeneous platoon case are described in Table 3.3.

Case	Points	Anisotropic Cells	Total Cells
Baseline Box Trailer	2,548,270	2,934,432	7,394,097
Baseline 40 ft. Shipping Containers	4,921,003	6,907,003	11,362,512
2x Box Trailer Lat. Offset	3,637,170	4,099,499	8,748,201
3x Box Trailer Intra-Platoon Var.	5,654,507	7,115,690	14,159,462
Heterogeneous 4 Truck Platoon	14,135,433	26,127,257	34,660,305

Table 3.2: Description of typical grid composition for the cases presented in this thesis

Scenario	Leader	Follower 1	Follower 2	Follower 3
1	Box	Full Shipping	Centered Shipping	Unloaded Flatbed
2	Unloaded Flatbed	Full Shipping	Centered Shipping	Box
3	Full Shipping	Box	Centered Shipping	Unloaded Flatbed

Table 3.3: Order of vehicles for heterogeneous 4 truck platoon scenarios

Chapter 4

Results & Discussion

Both qualitative analysis of the flow fields around the platoon vehicles and quantitative analysis of drag reduction on all trucks is conducted for CFD simulation results. No experimental data exists for direct comparison with CFD results, however at least moderate confidence can still be assumed based on practices following previously well-tested studies. Drag values are compared against baseline individual vehicle tests to track drag reduction.

4.1 Baselines

Some insight into the behavior of each trailer configuration and expected properties within a platoon of heterogeneous makeup is given by inspection of the wake profile of the trailers in isolated conditions shown in Figures 4.1 - 4.4. A look at the flow velocity as presented in Figures 4.5 - 4.8 shows that for even the most disparate cases, the wake is still laterally isolated to the width of the trailer. It should be noted that this is also not likely an unintended consequence of the “source” feature used to add grid refinement in the wake, as the geometry defined by this refinement region was significantly wider than the depicted resulting wakes. Unsurprisingly, all trucks feature large high pressure stagnation regions near the front of the vehicles extending just upstream of the engine compartment as well as low pressure recirculation areas on the hood followed by another stagnation region before the truck’s fairing. Also unsurprisingly, the flatbed configuration features the smallest wake profile out of the four trailer configurations, with free-stream pressure re-establishing fairly quickly after the trailer gap region, and the wake behind the end of the trailer dissipating rapidly. More interesting however is the differences in wake topology for the other three vehicles. With the box trailer, the wake at the end of the trailer is fairly isolated and recirculation within the trailer-gap is highly concentrated near the top and bottom. By contrast, both of the shipping container configurations have a far lengthier and more intense recirculation region within this trailer gap. It seems by inspection that this also affects the general wake of the trailers, as both cases connected wake region spanning from the end of the truck's fairing to the trailing edge of the trailer.

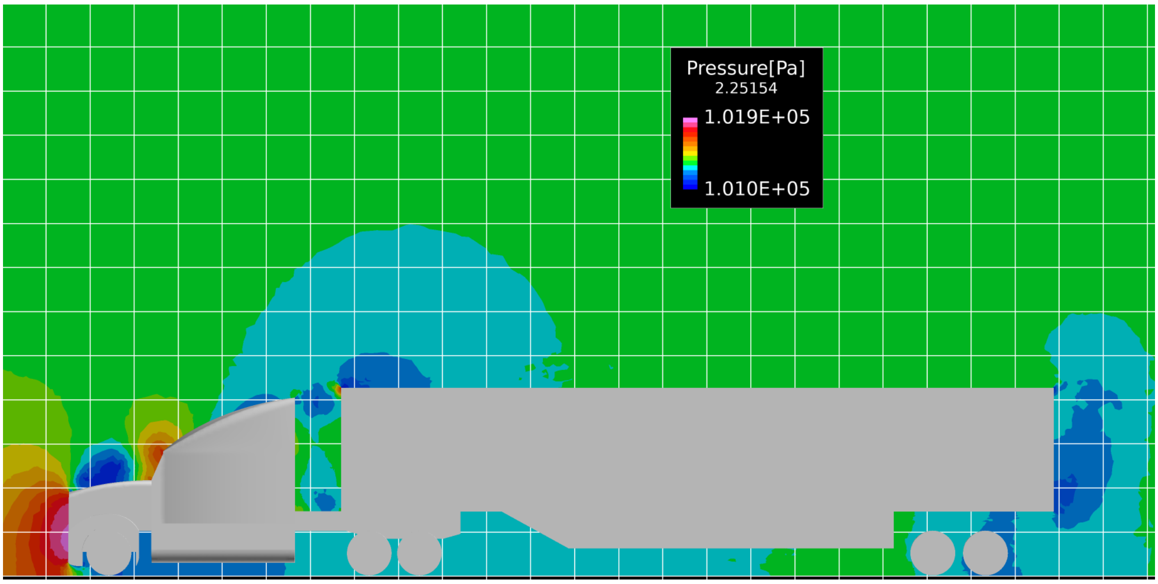

Figure 4.1: Static pressure contour for the isolated box trailer configuration baseline case. Grid is demarcated in uniform 1.0 meter increments. The subtitle, 2.25154, refers to z-location of the coordinate plane, in meters

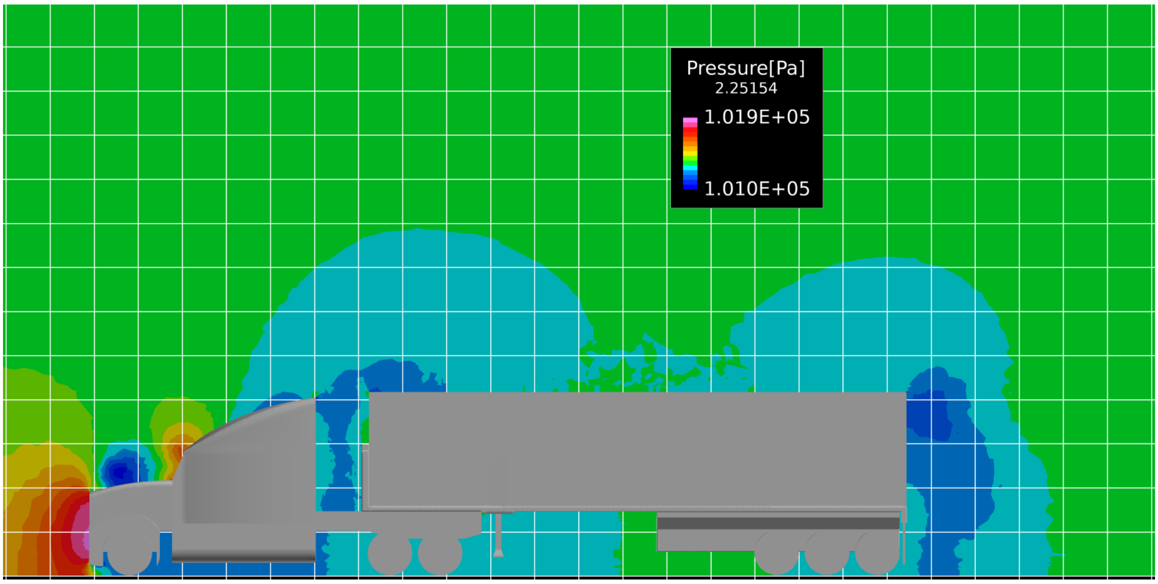

Figure 4.2: Static pressure contour for the isolated full shipping container trailer configuration baseline case. Grid is demarcated in uniform 1.0 meter increments

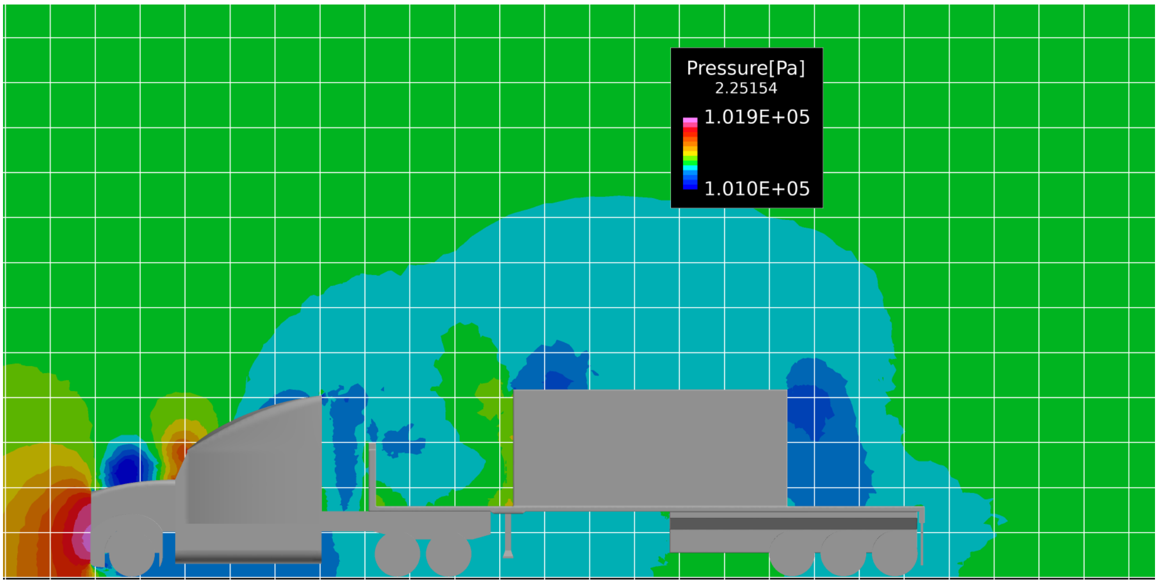

Figure 4.3: Static pressure contour for the isolated centered shipping container trailer configuration baseline case. Grid is demarcated in uniform 1.0 meter increments

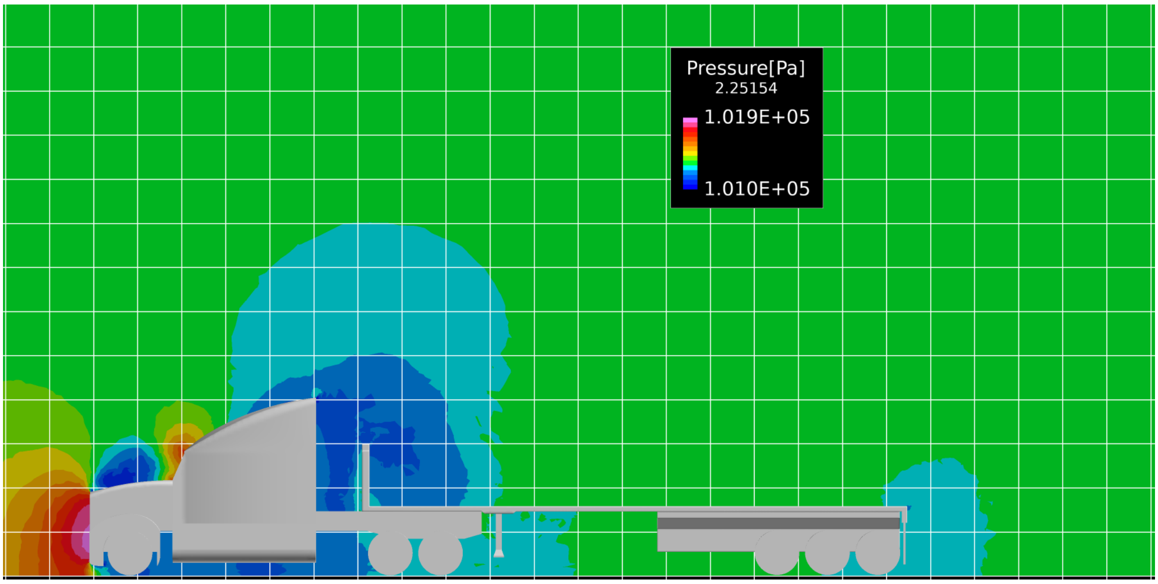

Figure 4.4: Static pressure contour for the isolated unloaded flatbed trailer configuration baseline case. Grid is demarcated in uniform 1.0 meter increments

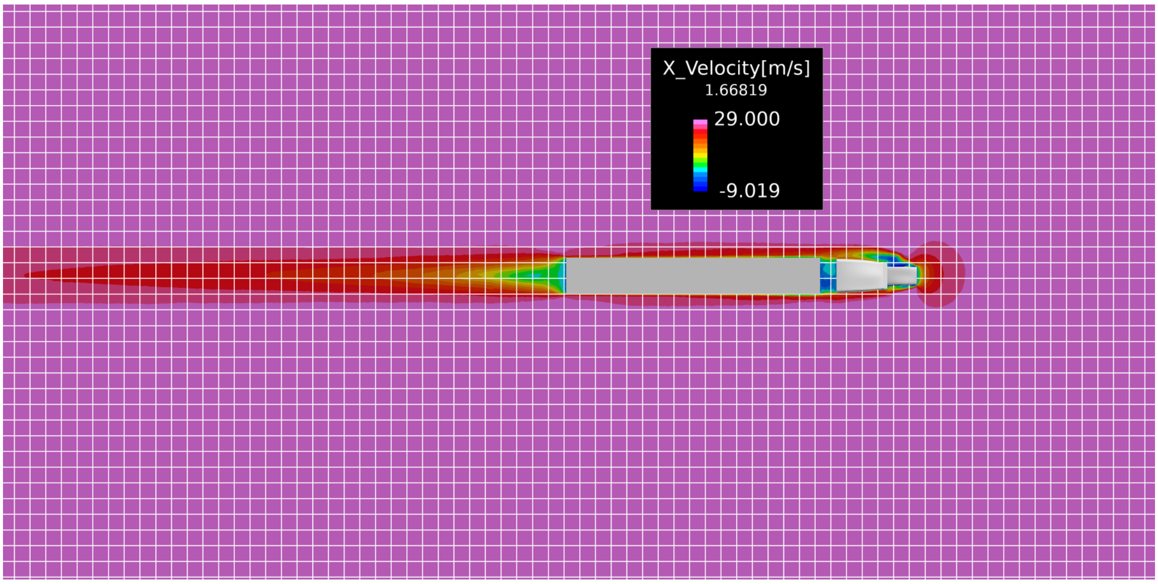

Figure 4.5: Overhead view of x velocity (with +x being flow direction) for box trailer in baseline configuration. Grid is demarcated in uniform 1.0 meter increments

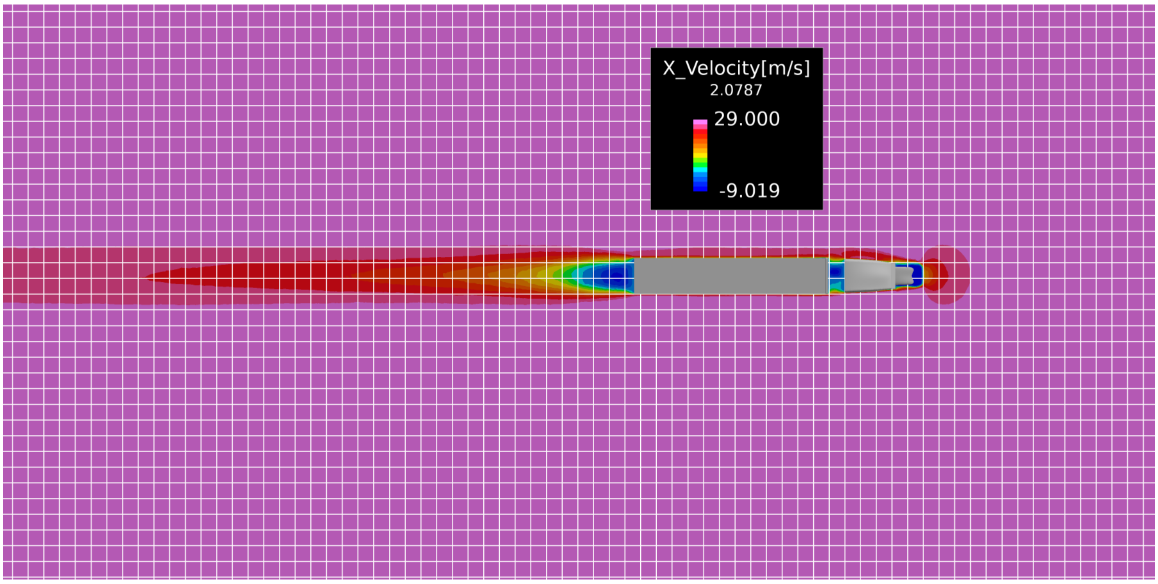

Figure 4.6: Overhead view of x velocity (with +x being flow direction) for full shipping container trailer in baseline configuration. Grid is demarcated in uniform 1.0 meter increments. The subtitle, 1.66819, refers to y-location of the coordinate plane, in meters

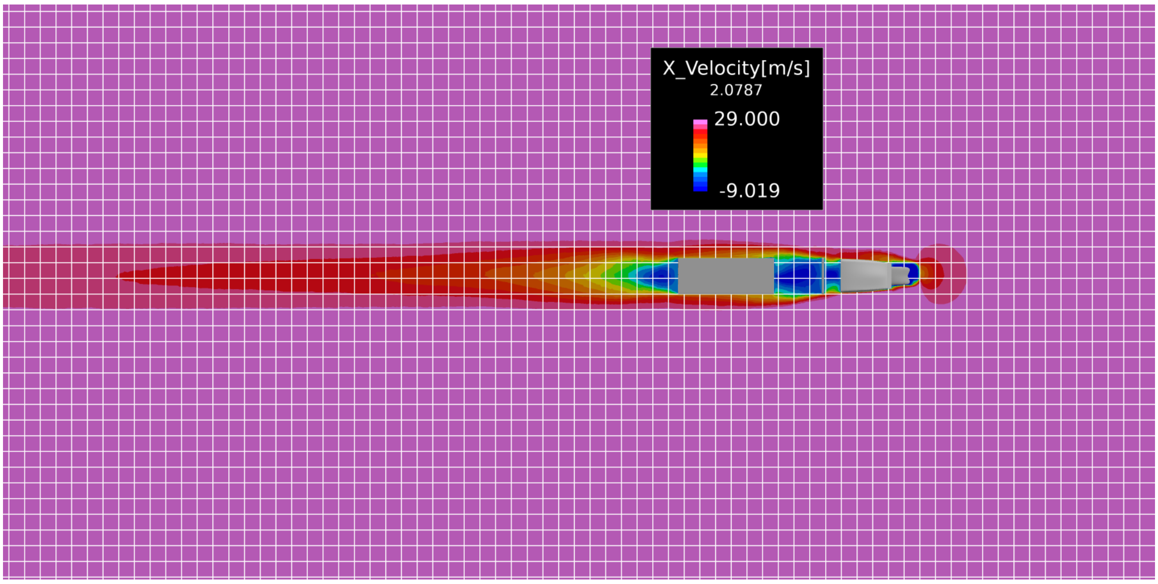

Figure 4.7: Overhead view of x velocity (with +x being flow direction) for centered shipping container trailer in baseline configuration. Grid is demarcated in uniform 1.0 meter increments

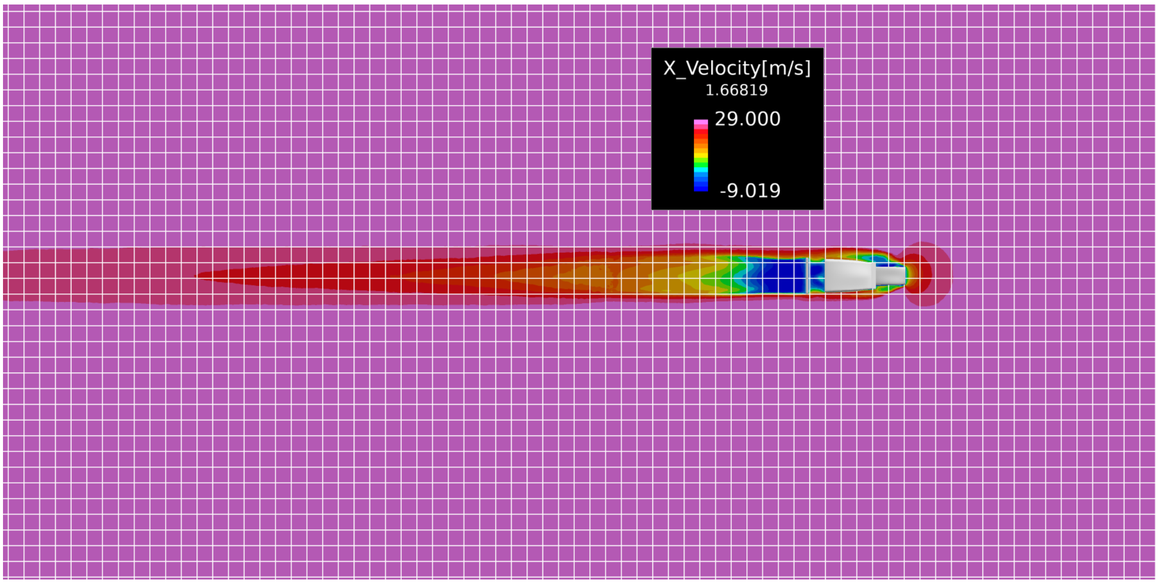

Figure 4.8: Overhead view of x velocity (with +x being flow direction) for unloaded flatbed trailer in baseline configuration. Grid is demarcated in uniform 1.0 meter increments

4.2 Lateral Offset

For the most part, the data from the lateral offset cases presented in Figure 4.9 shows two fairly consistent tends. The first of these is similar to the case presented in Figure 1.3 where the lead vehicle is fairly insensitive to changes in lateral offset. The second general trend is that the follower vehicle is much more sensitive to lateral offset, where the largest offset is typically only about half as effective at reducing drag when compared to no lateral offset. There is a rather obvious outlier presented though, occurring at 20 ft. separation with 10% lateral offset, where both the lead and follower vehicles see a drastic increase in drag reduction not seen in other trends. When comparing the 20 ft. separation distance in Figure 4.12 with both the 10 ft separation distance in Figure 4.11 and the 30 ft separation distance in Figure 4.13, it seems that at 10% offset the follow vehicle is still fully in the wake of the lead for 10 ft and 20 ft.

In order to study the sensitivity in this region to lateral offset, additional offsets of 5%, 8%, 12% and 15% are conducted at 20 ft. separation distance, with drag reduction presented in Figure 4.10. However no clear explanation can be drawn from these results as there is no indicator at lateral offsets smaller or larger than 10% that suggests the behavior at 10% itself. In-line with the results from Figure 4.9 though, the more extensive sweep of lateral offsets at 20 ft. do show a significant influence of lateral offset on drag reduction.

A qualitative analysis of the velocity plots in Figures 4.11 - 4.15 also shows that for smaller separation distances, there is a more significant modification to the width of the wake from the lead trailer. At a large offset, the wake is highly non uniform across the front of the follower truck and in most cases the largest velocity deficits from the lead trailer are detached from the region in front of the follower truck. Conversely, there remains some level of connection between the core of the wake and the front surface of the follower truck across most offsets at large separation distances. For 20 ft separation and 10% offset, it is interesting to note that there is a somewhat significant expansion of the low velocity core of the lead truck wake that isn't seen at the other separation distances for 10% offset. It is possible that this is a critical region for 20 ft separation distance and that similar critical regions exist at different lateral offsets for other small separation distances. Analyzing the results over a small sample time for the 20 ft case at 0% offset and 10% offset presented in Appendix B shows that that not only does the recirculation zone rear of the leader get stretched, but also that the vortex shedding on the front of the leader becomes much stronger.

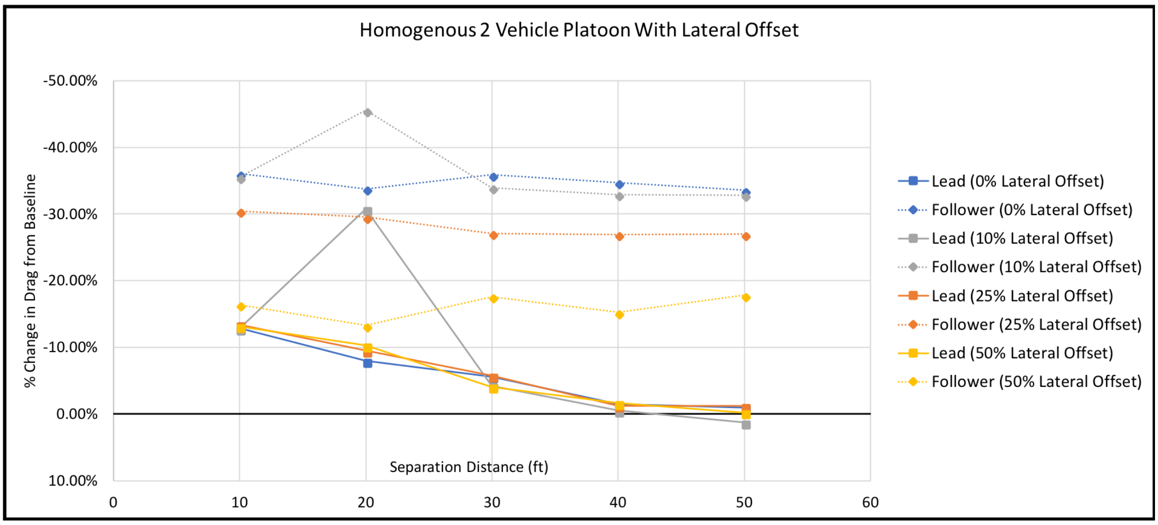

Figure 4.9: Drag reduction for lead and follower vehicles in lateral offset tests

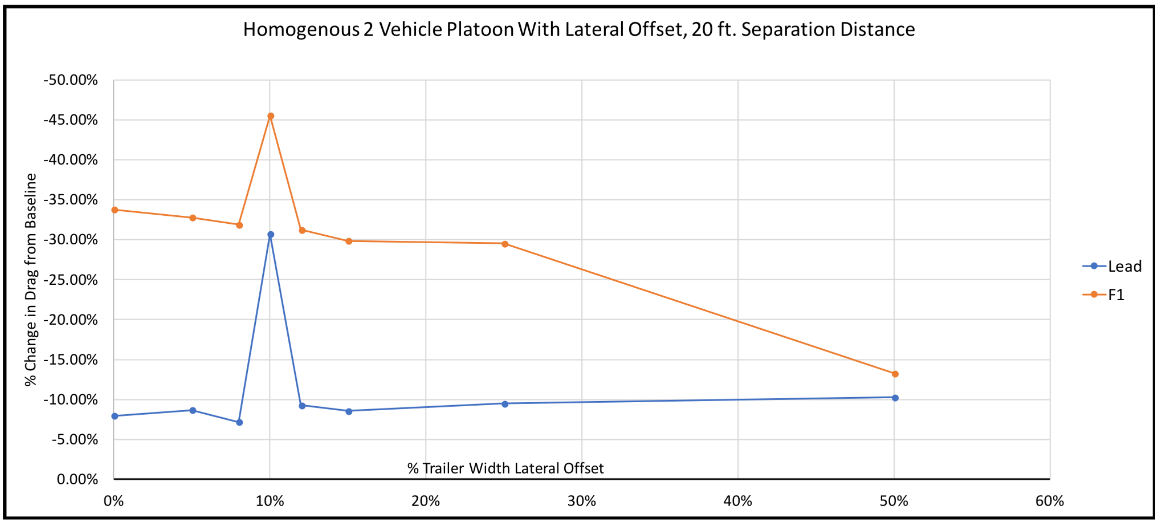

Figure 4.10: Drag reduction for two truck homogeneous platoon as a function of lateral offset, 20 ft. separation distance

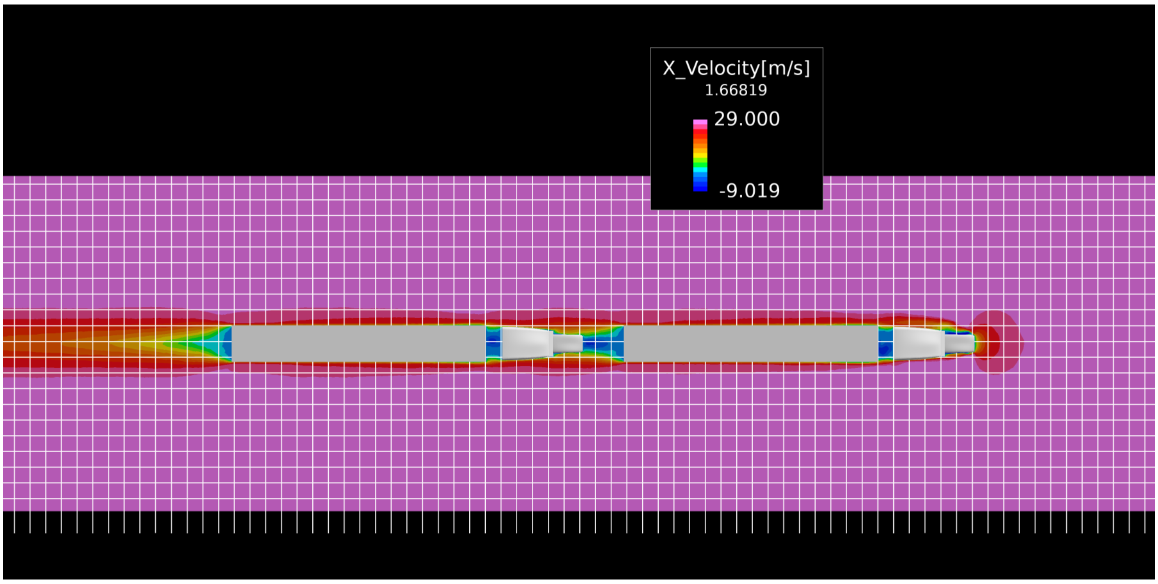

(a) 0% offset

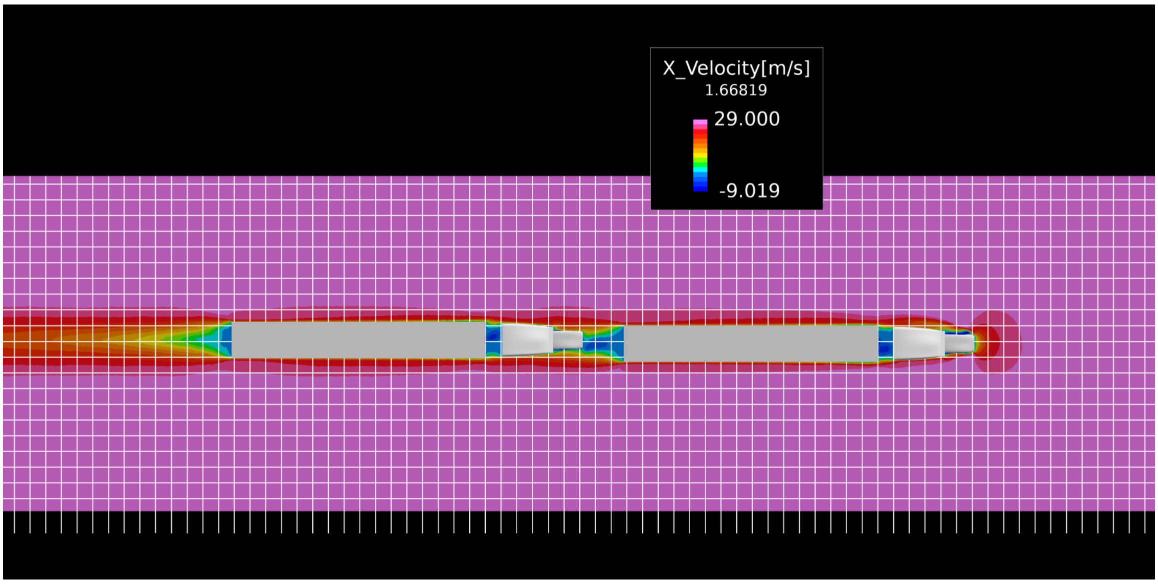

(b) 10% offset

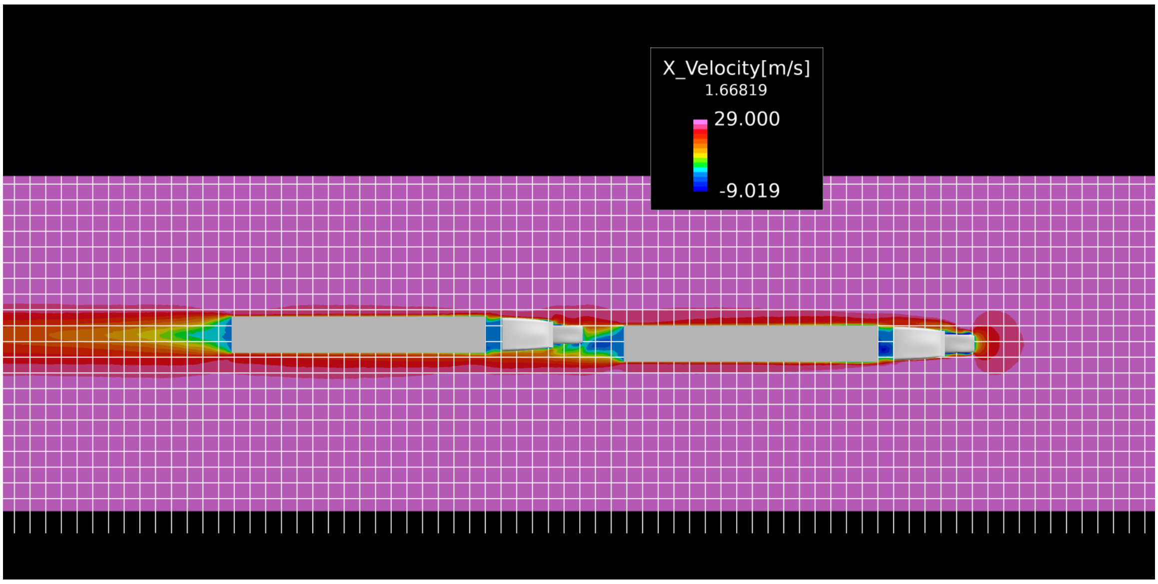

(c) 25% offset

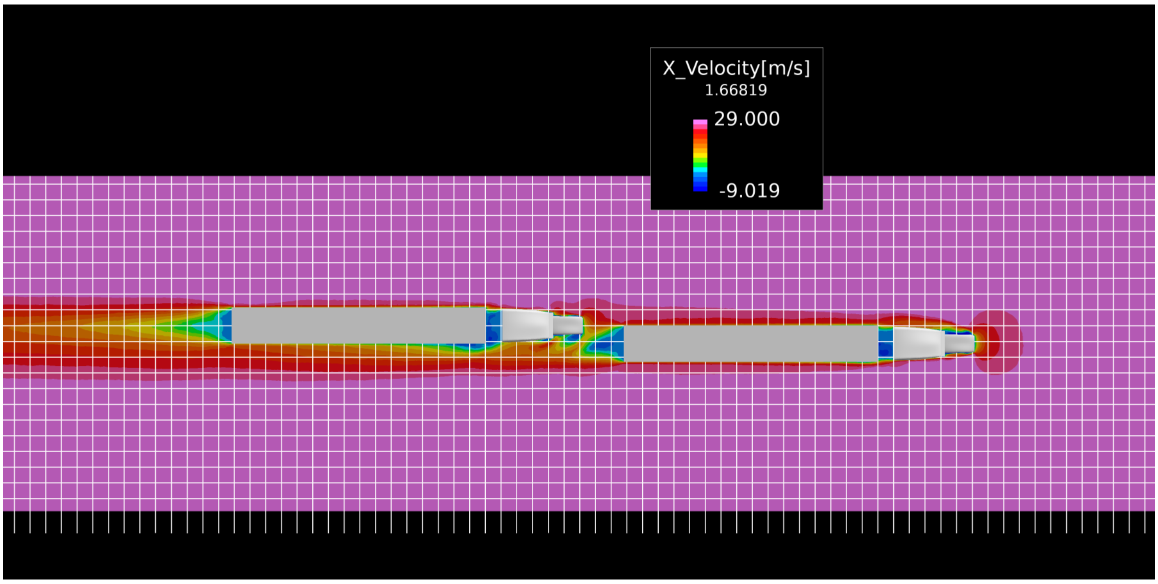

(d) 50% offset

Figure 4.11: X-Velocity profile for homogeneous, two box trailer platoon with 10 ft separation distance at 0%, 10%, 25% and 50% lateral offset

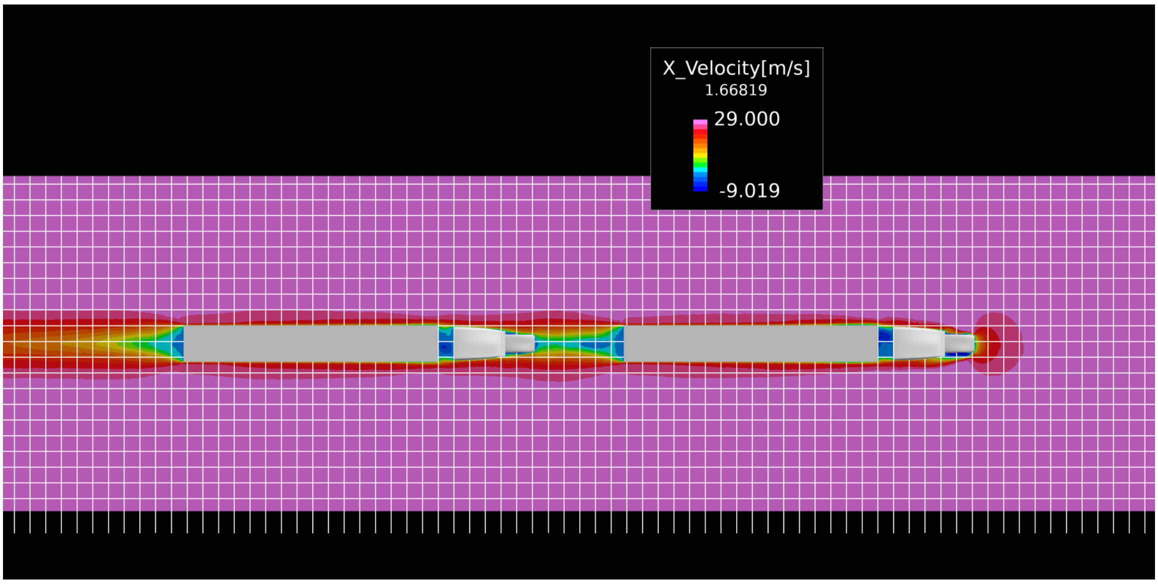

(a) 0% offset

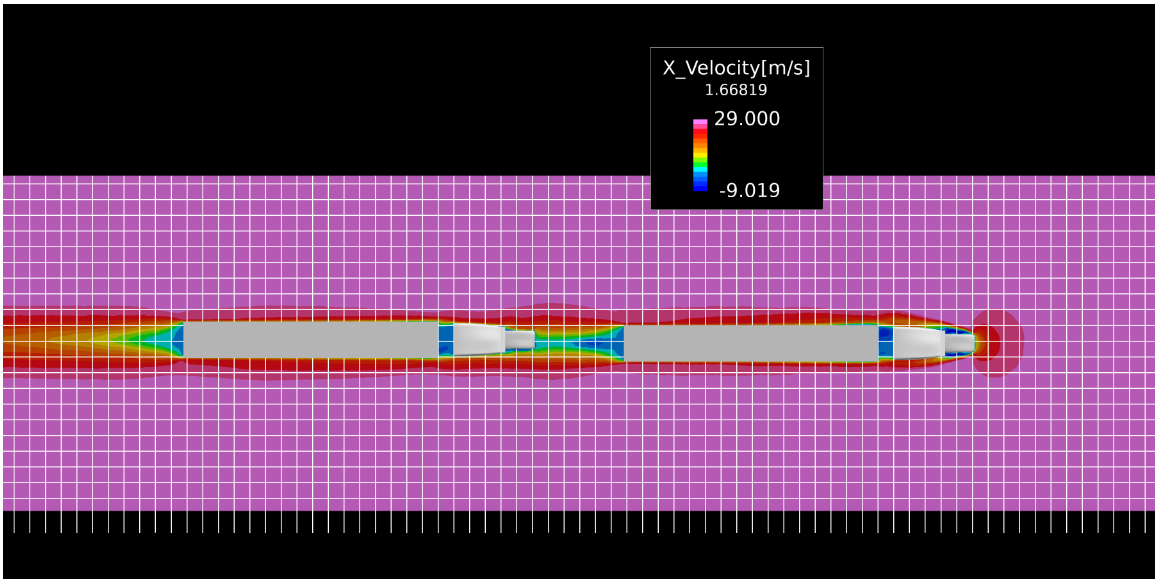

(b) 10% offset

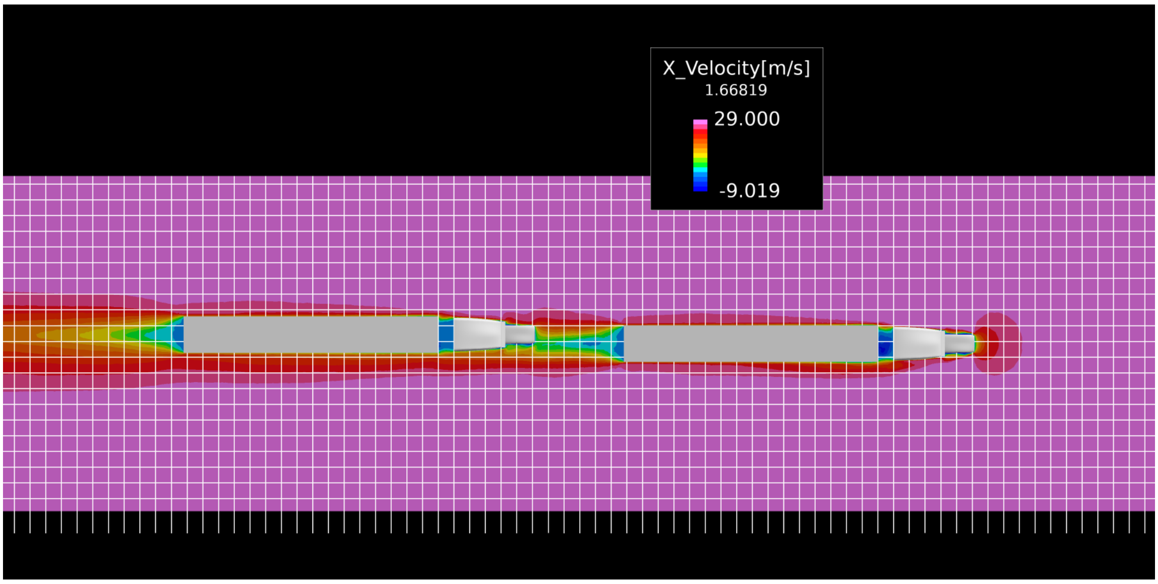

(c) 25% offset

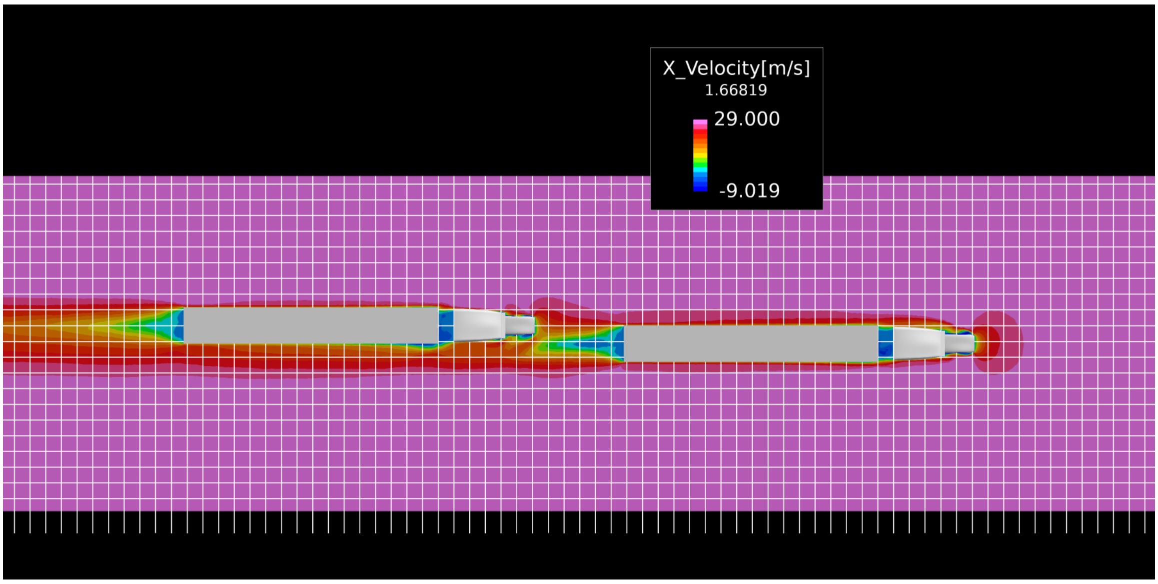

(d) 50% offset

Figure 4.12: X-Velocity profile for homogeneous, two box trailer platoon with 20 ft separation distance at 0%, 10%, 25% and 50% lateral offset

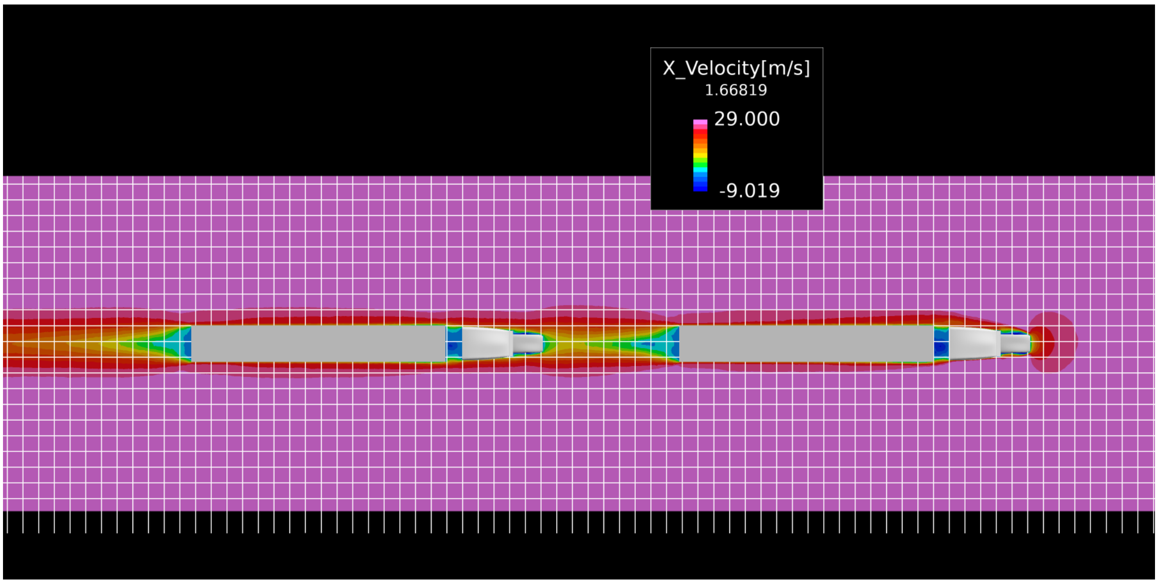

(a) 0% offset

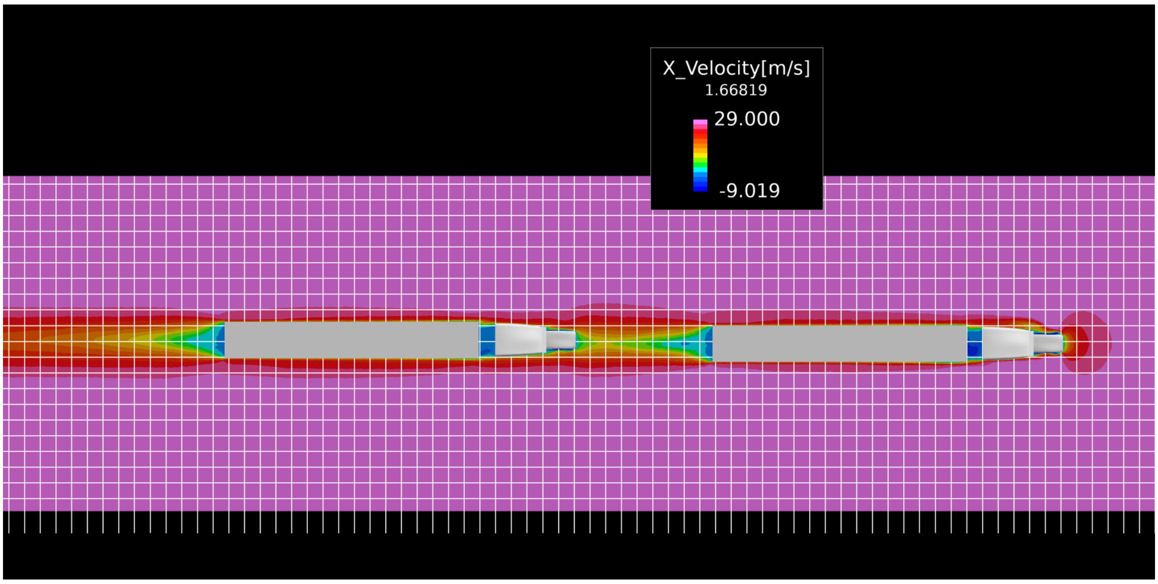

(b) 10% offset

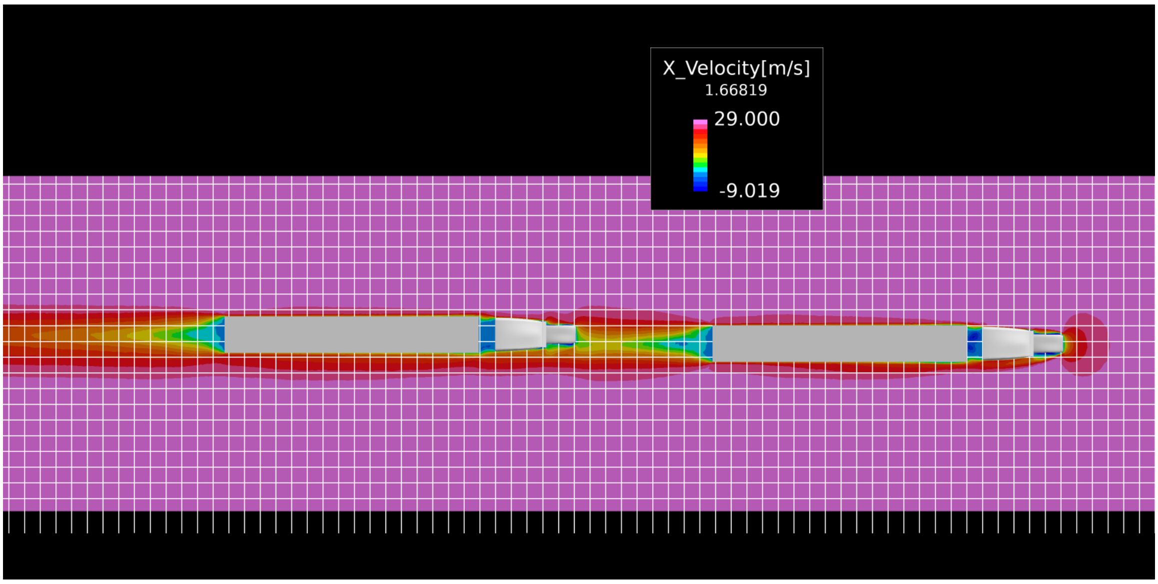

(c) 25% offset

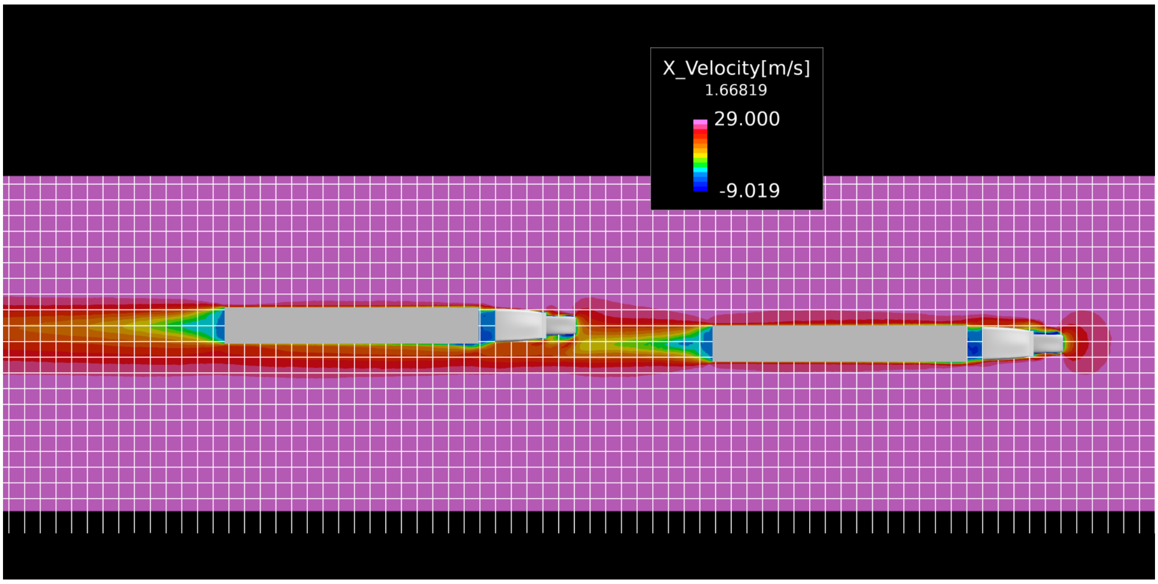

(d) 50% offset

Figure 4.13: X-Velocity profile for homogeneous, two box trailer platoon with 30 ft separation distance at 0%, 10%, 25% and 50% lateral offset

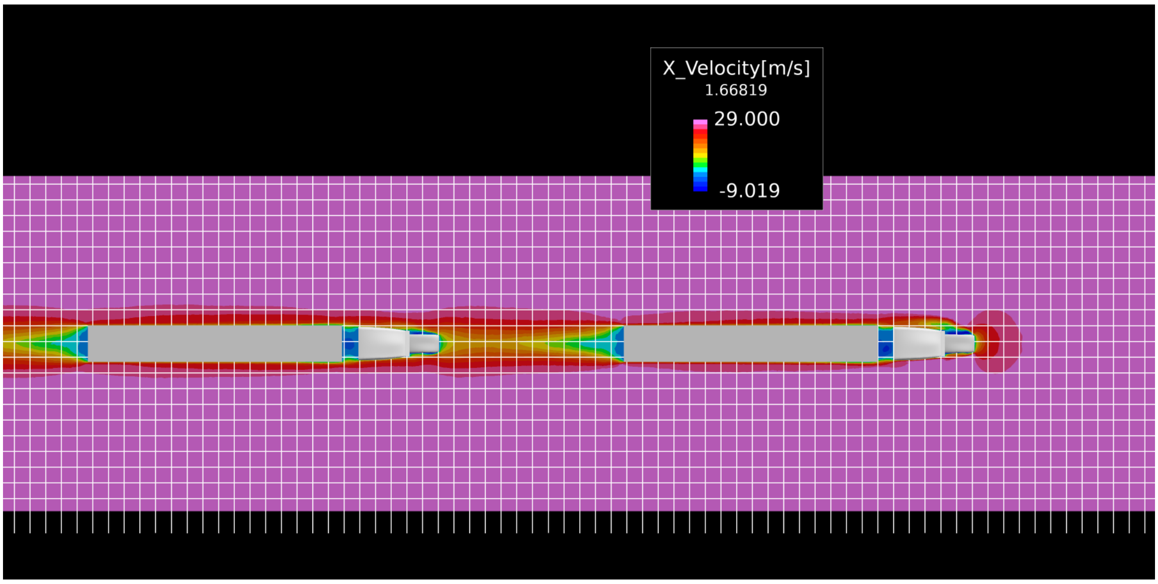

(a) 0% offset

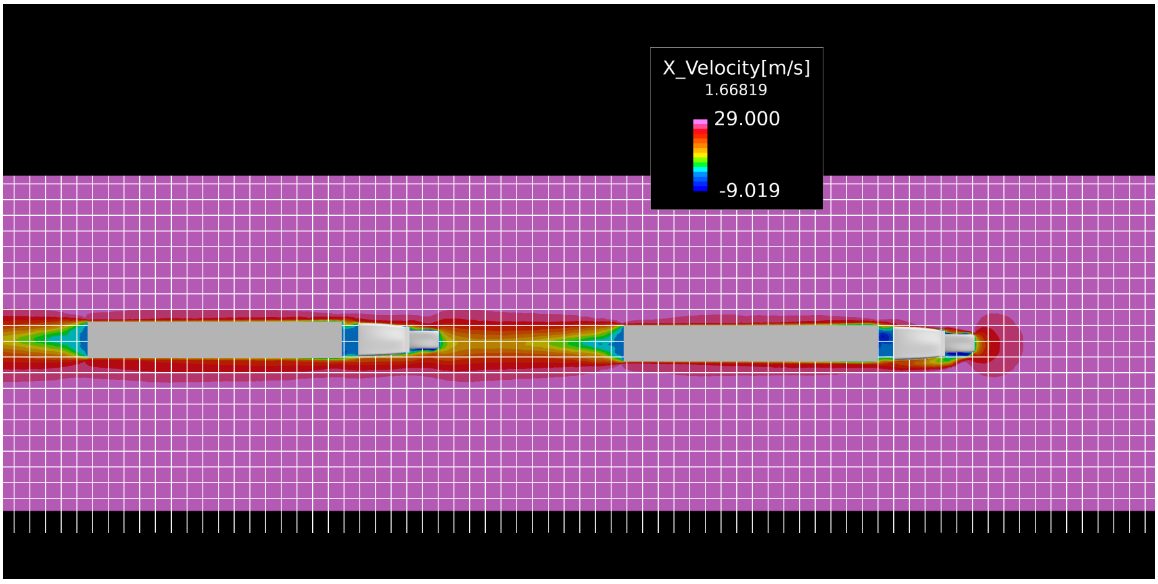

(b) 10% offset

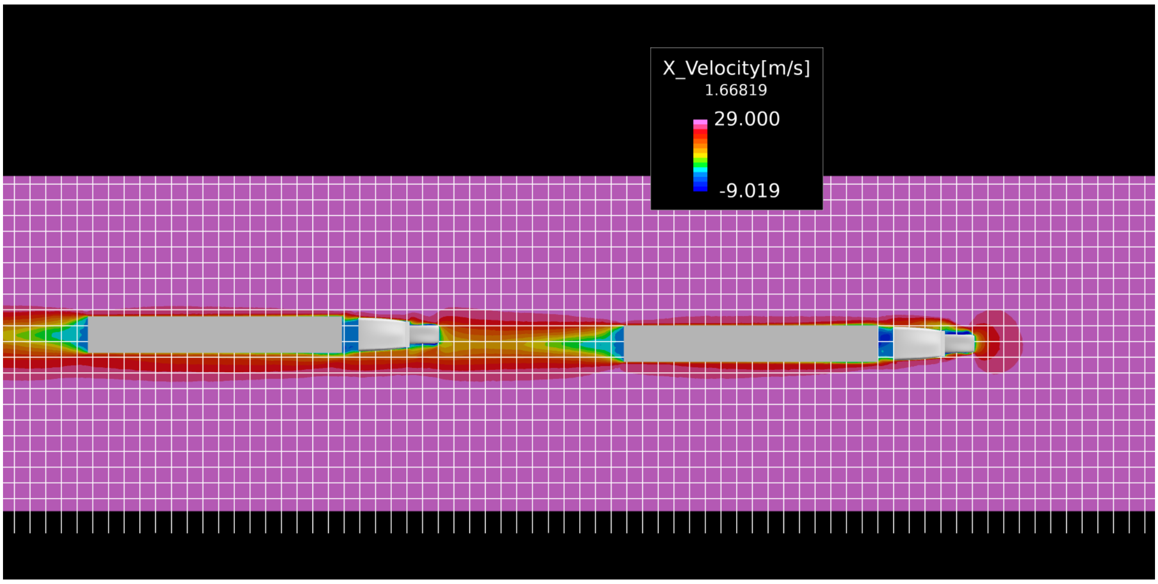

(c) 25% offset

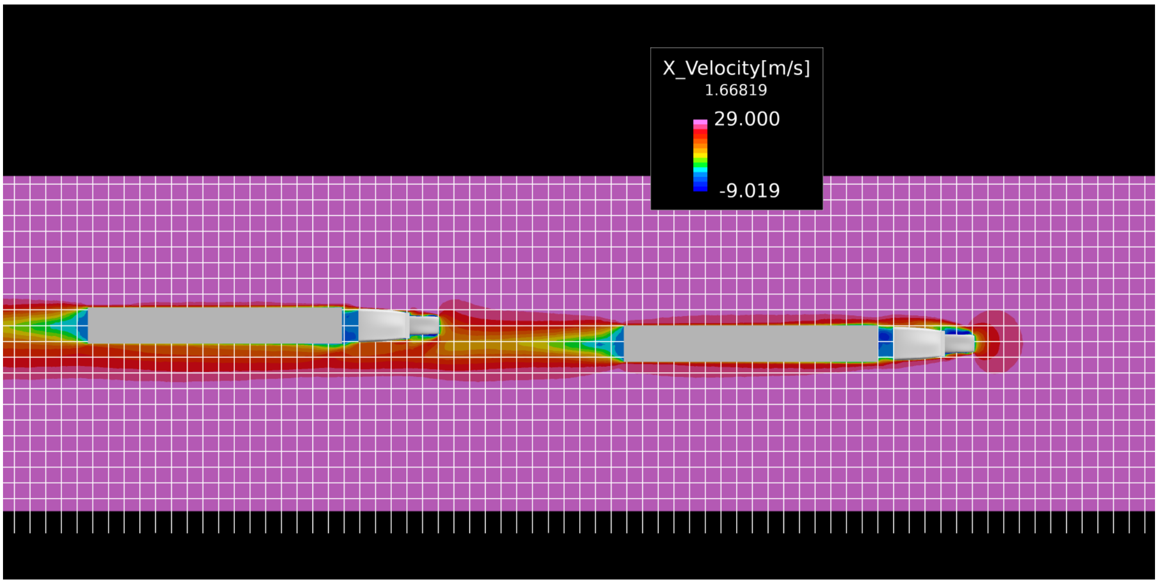

(d) 50% offset

Figure 4.14: X-Velocity profile for homogeneous, two box trailer platoon with 40 ft separation distance at 0%, 10%, 25% and 50% lateral offset

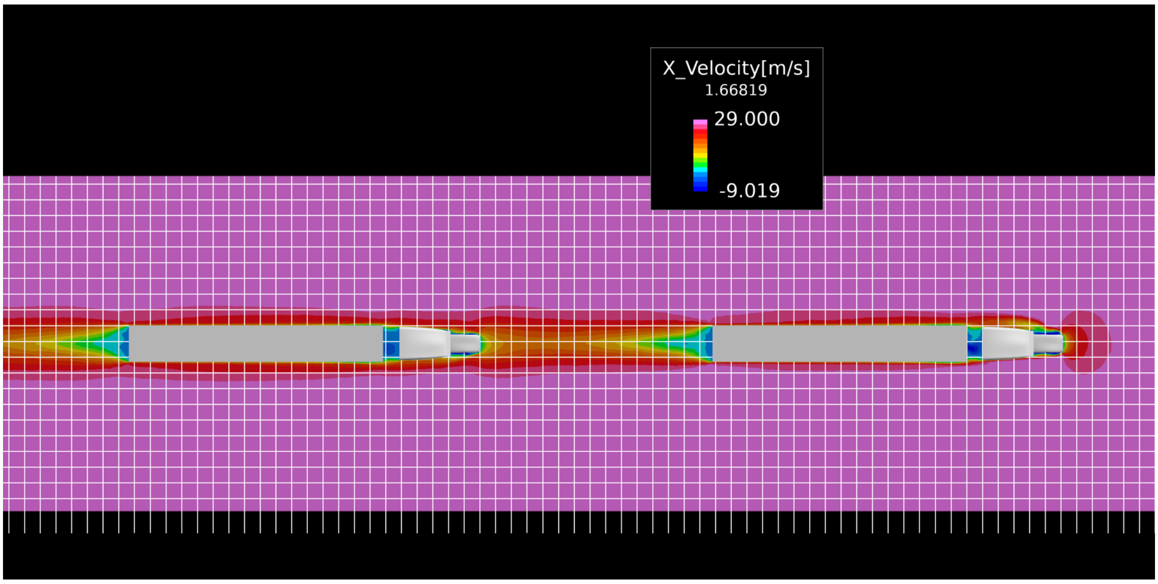

(a) 0% offset

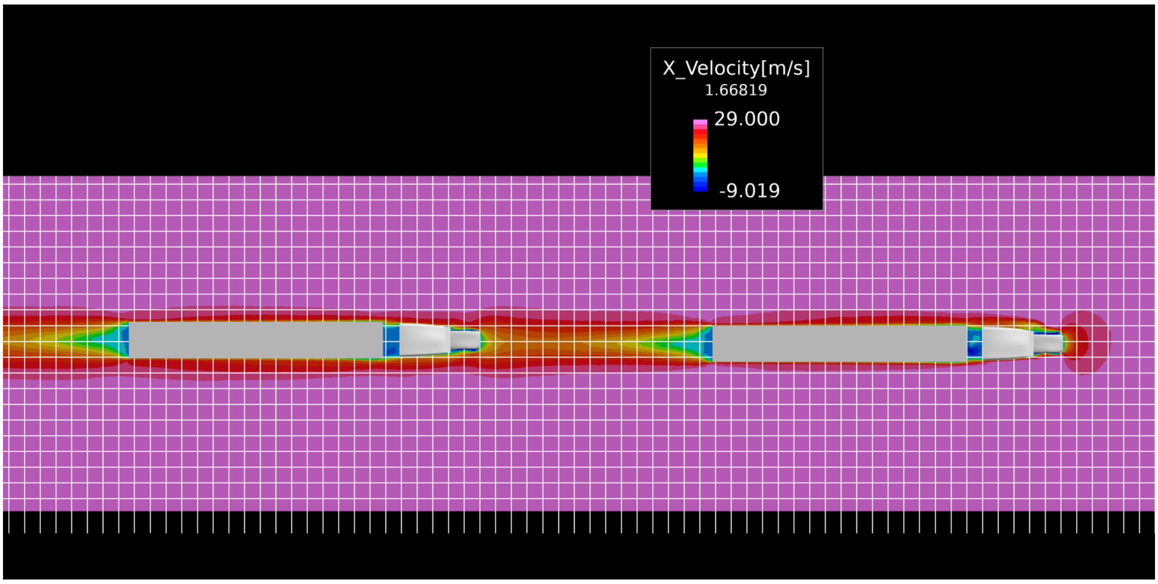

(b) 10% offset

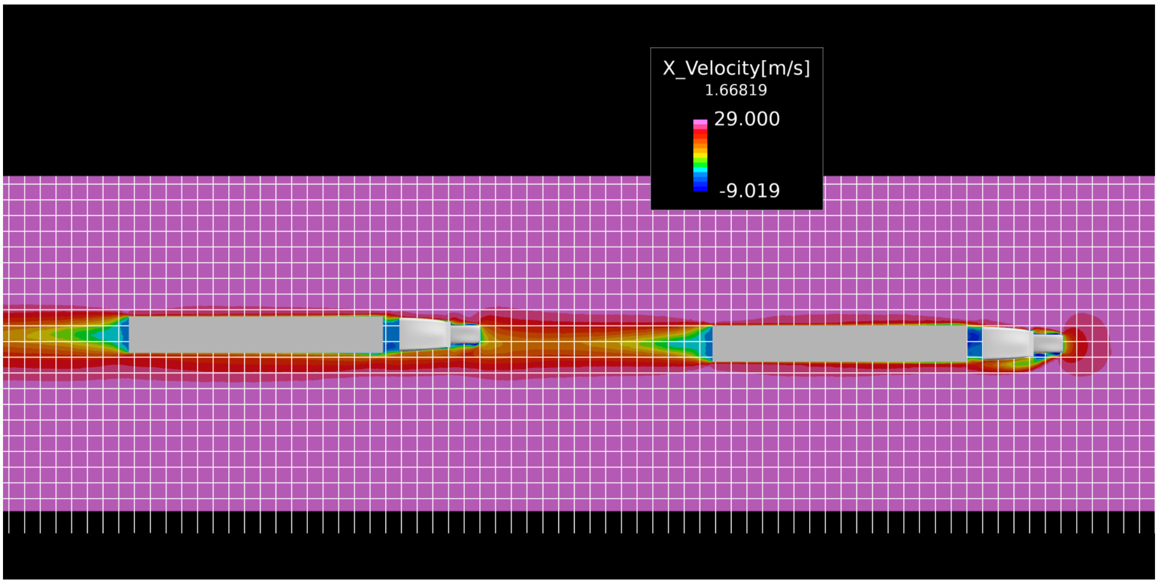

(c) 25% offset

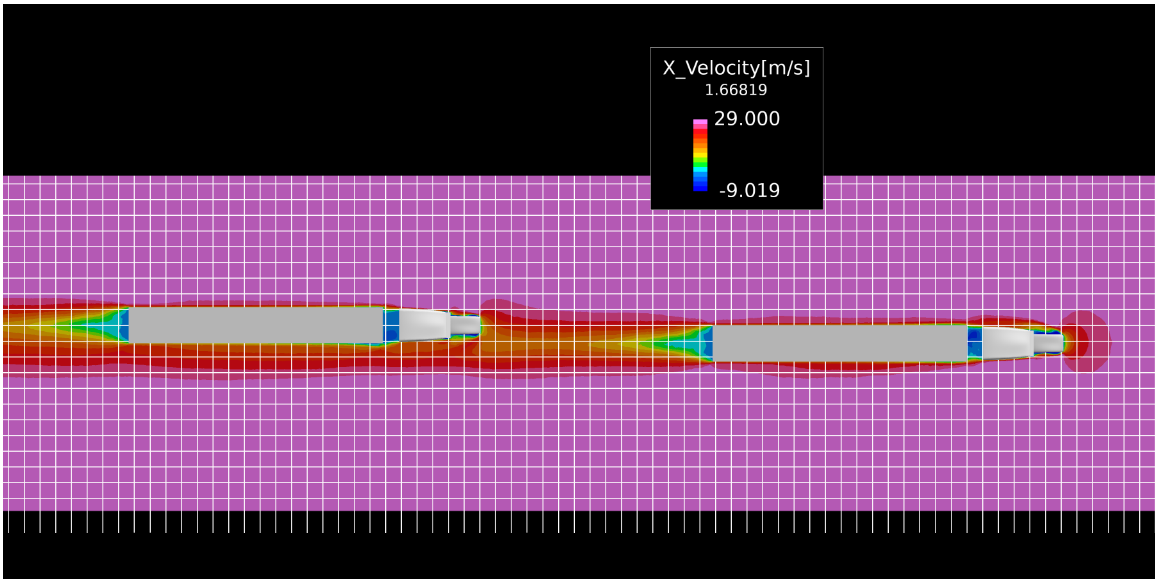

(d) 50% offset

Figure 4.15: X-Velocity profile for homogeneous, two box trailer platoon with 50 ft separation distance at 0%, 10%, 25% and 50% lateral offset

4.3 Intra-Platoon Separation Distance Variation

First, solutions are run for identical separation distances between Lead - Follower 1 (L-F1) and Follower 1 - Follower 2 (F1-F2)to identify some baseline expected behavior. Similar to results from the two vehicle platoon with 0% lateral offset in Figure 4.9, the lead vehicle does not see measurable benefit beyond 50 ft. and experiences increased drag at 100 ft., shown in Figure 4.16. Some fluctuation around 0% change is expected for larger separation distances but the magnitude of the drag increase on the lead vehicle is certainly not expected. However, when accounting for the platoon as a whole, these values do not severely impact overall trends. While both follower vehicles see an increased benefit over the two vehicle platoon's lone follower, F2 experienced an increased drag reduction over F1 at larger separation distances. This is substantially different from the trend observed at separation distances below 50 ft. Therefore, more cases are run at larger separation distances, with only variation in the distance L-F1, keeping F1-F2 at a constant 100 ft. The results from these tests are shown in Figure 4.17. As the distance between L-F1 is increased, there is relatively little change in the drag on F2, and throughout all separation distances the leader sees almost no change in drag force. Additionally, after about a L-F1 separation distance of 140 ft., even F1 is fairly insensitive to changes in separation distance. Again however, the nature of the large drag increase on the lead truck in these scenarios is somewhat puzzling. One would expect that as separation distance is even further increased, the lead truck would trend back to the baseline drag (therefore, 0% change) but this is not the case. It is possible that there is something like a 15% shift in the numbers and that accounting for this would more reliably represent drag values, but the author did not find anything numerically or in post-processing procedure that would suggest this on the user side. This persistent 15% trend does not wholly undermine the overall trends observed for the other trucks and the platoon as a whole, however.

The opposite scenario is also tested to a limited extent, where the distance between L-F1 was kept constant at 100 ft. and the distance between F1-F2 was extended. The results from this scenario are presented and compared against the previous scenarios in Figure 4.18. Interestingly, it seems that not only does an increased separation distance towards the rear of the platoon dramatically increase the effectiveness of each vehicle, but it appears that for this scenario, at least in the separation distances tested, the platoon is relatively insensitive to further increases in rear platoon separation distances. This is especially interesting when compared to Figure 4.16 since intuitively one might presume that the smaller separation distances across the whole platoon would be the ideal scenario, however comparable drag reduction is achieved at even larger separation distances.

An analysis of the x-velocity plots in Figures 4.19 - 4.21 reveals some unexpected trends overall. Figures 4.19 and 4.20 show that the wake starts relatively confined to the trailer width for the first gap, and increases in width after the first gap. However, Figure 4.21 shows a wider expansion of the wake in the first 100 ft. gap, and an even greater expansion of the wake for the second 130 ft. gap. This seems to suggest that the increased gap between the follower trailers has a significant effect on the wake expansion between the leader and F1 which is then compounded by F1's own wake. In addition, this creates a much lower drag profile on the lead vehicle than either the homogeneous separation distances or modulation of the L-F1 separation distance. The fact that this trend exists for both the 130 ft and 150 ft rear separation cases lends some credence to the validity of this observed effect.

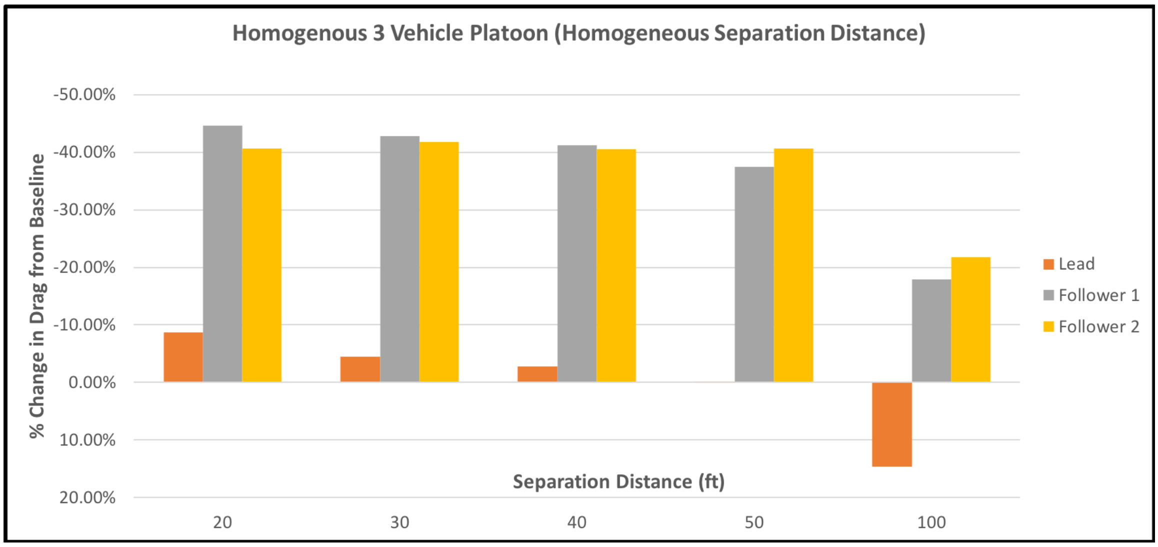

Figure 4.16: Drag reduction for three vehicle platoon, L-F1 and F1-F2 separation distance being equal

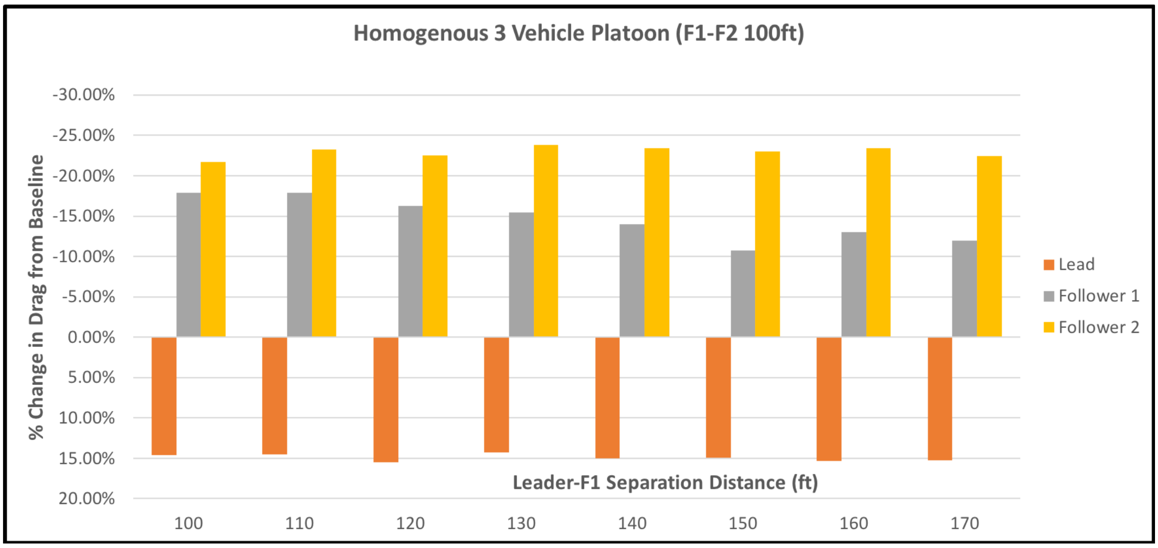

Figure 4.17: Drag reduction for three vehicle platoon with L-F1 varied, F1-F2 separation constant at 100 ft.

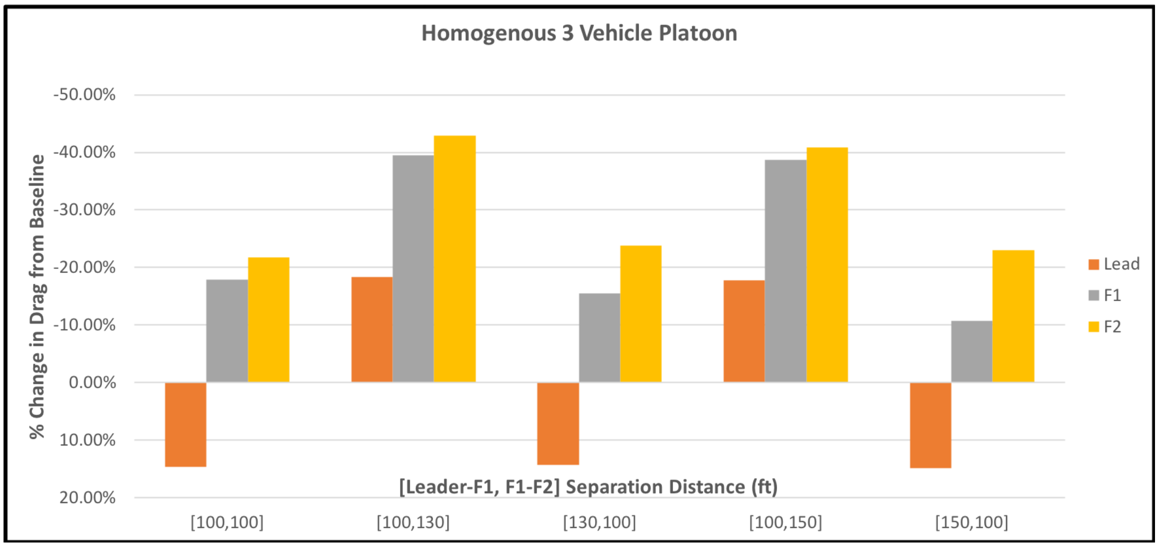

Figure 4.18: Comparison of drag reduction for a select number of variations in intra-platoon separation distance

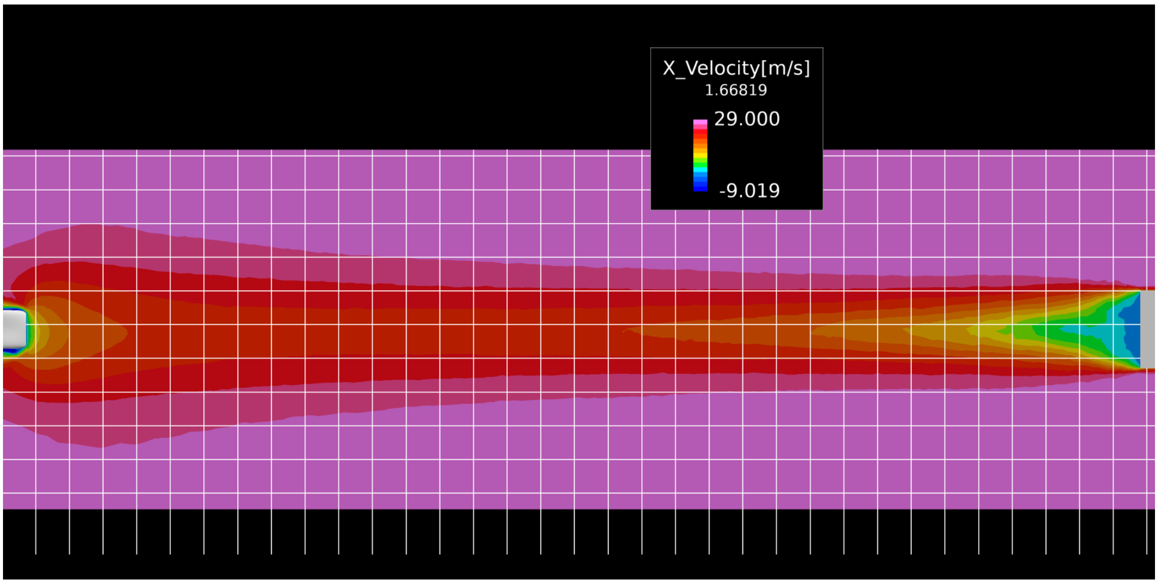

(a) L - F1

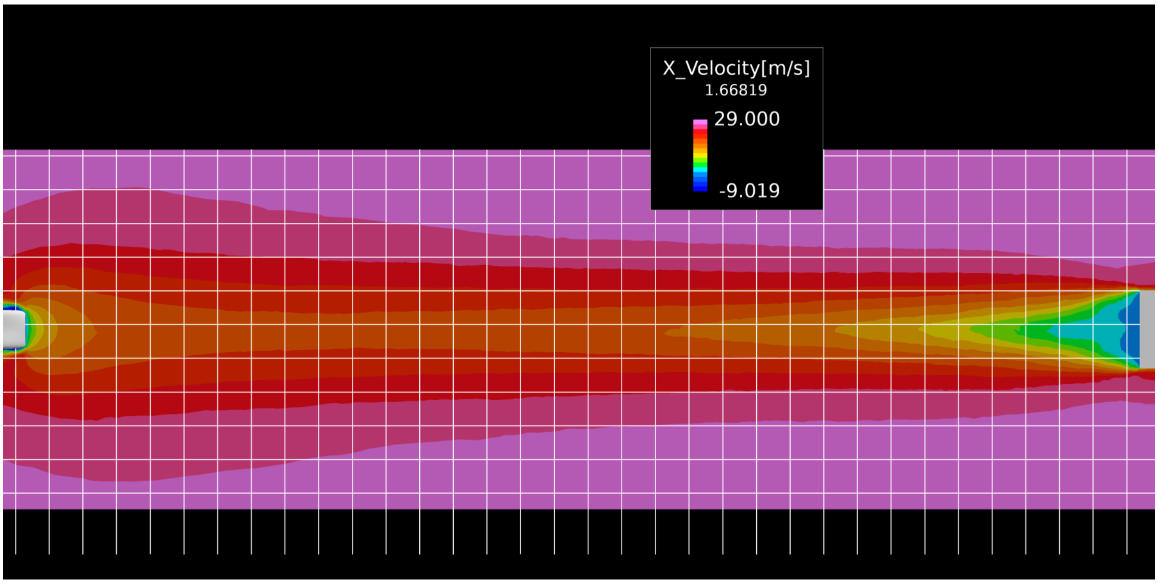

(b) F1 - F2

Figure 4.19: X-Velocity profile for three vehicle homogeneous platoon with uniform 100 ft separation distance

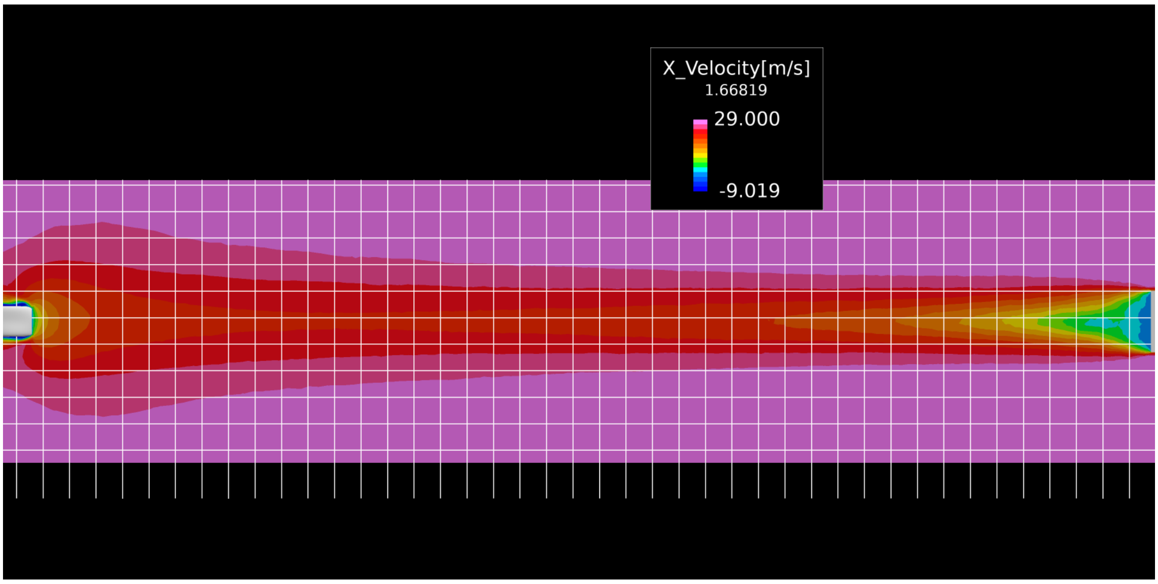

(a) L - F1

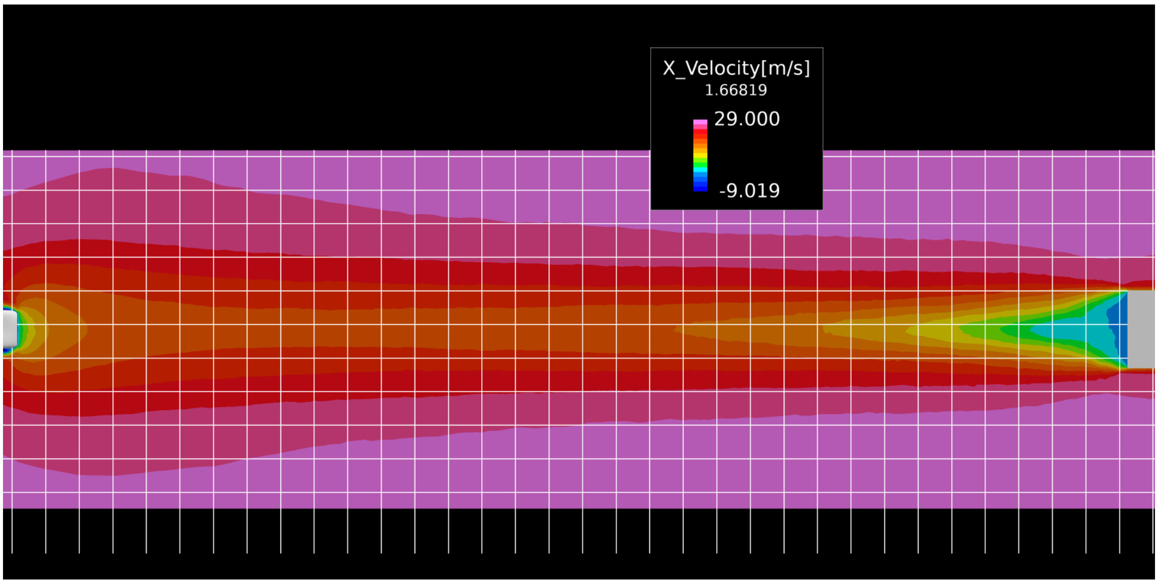

(b) F1 - F2

Figure 4.20: X-Velocity profile for three vehicle homogeneous platoon with 130 ft separation distance between L - F1 and 100 ft separation distance between F1 - F2

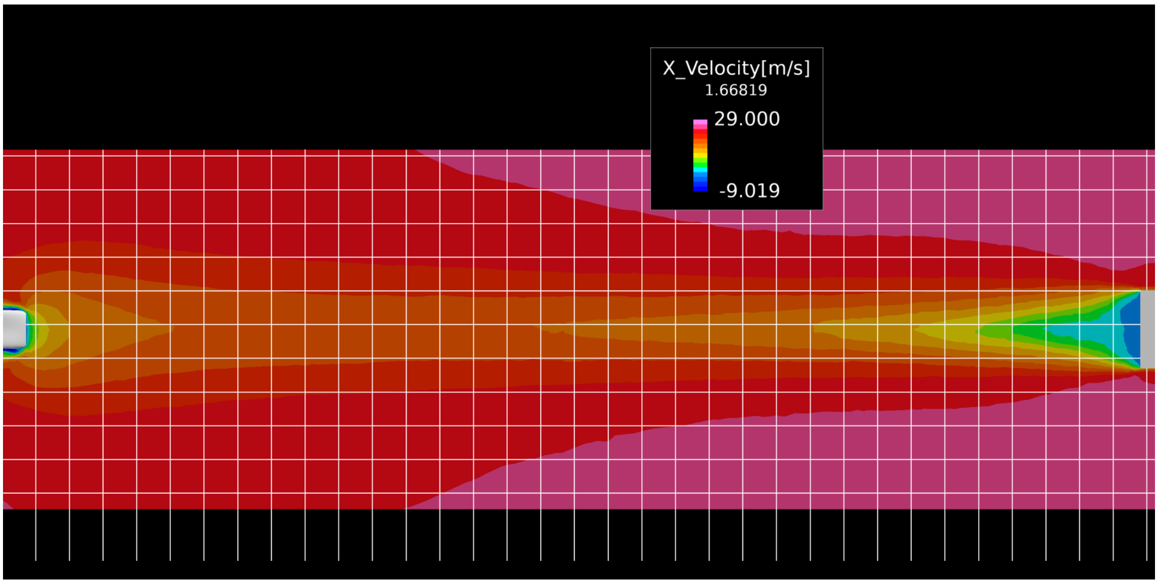

(a) L - F1

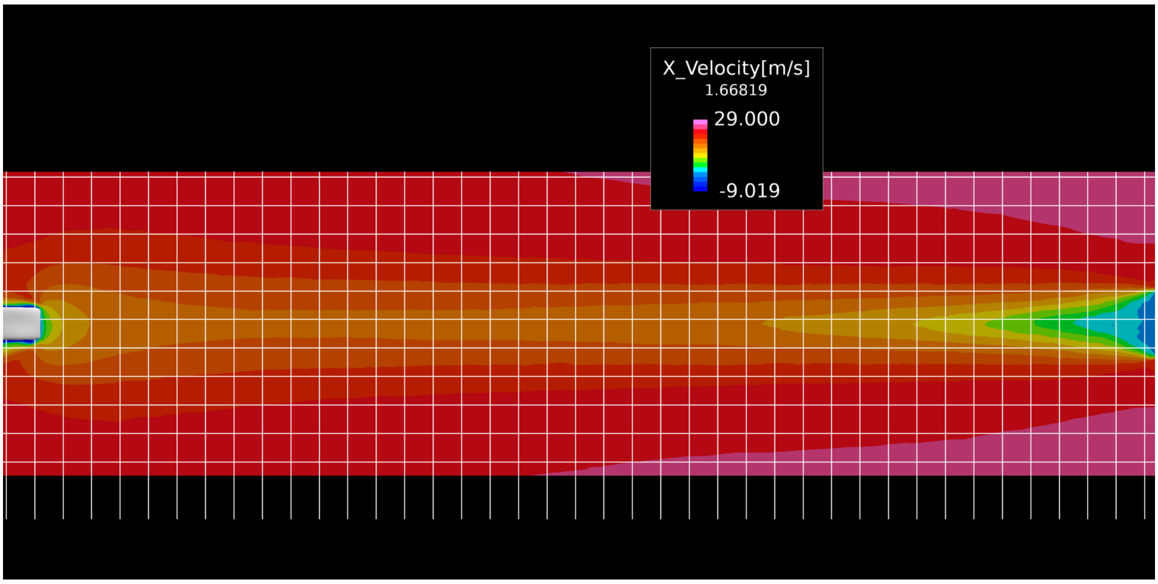

(b) F1 - F2

Figure 4.21: X-Velocity profile for three vehicle homogeneous platoon with 100 ft separation distance between L - F1 and 130 ft separation distance between F1 - F2

4.4 Heterogeneous Platoon

Scenario 3 described in Table 3.3 is limited in scope. Certain separation distances for this combination of vehicles led to erratic and often divergent solutions when subjected to the same parameters as the other cases in this thesis. As such, only data from those separation distances with high confidence, run with the same conditions as all other cases described in this study, is presented from this scenario.

It was hypothesized beforehand that Scenario 1 would be the most beneficial, placing the largest wake vehicles in the front and allowing those vehicles with smaller wakes to take advantage of the disturbed free-stream. Unexpectedly then, drag results from Figures 4.22 and 4.23 show up to about a 50% difference overall between the two platoons at 50 ft., with the flatbed in the lead of Scenario 2 seeing significantly reduced forces compared to Scenario 1 at all separation distances. This is in some agreement with suggestions of recent track testing [11] where scenarios with aerodynamically optimized trailers (featuring side-skirts and boat-tails) placed towards the rear of the platoon benefited the platoon much more significantly than standard trailers in the same positions.

An examination of the static pressure contours presented in Figures 4.25 through 4.31 allow for some inspection of the scenario and separation distance effects on the vehicle wakes. For 50 ft. separation distance, there are significant differences in the wake profiles of all vehicles between the two scenarios. Most significantly are the wakes behind the 20 ft. centered shipping container and the 53 ft. box trailer. The former features a much smaller recirculation region at the top of the trailing edge of the shipping container in Scenario 2 when compared to Scenario 1, while the latter has almost fully eliminated this region at the bottom of the trailing edge of the box trailer. Also of note is the lack of a clear, strong recirculation region at the front of the 40 ft. shipping container configuration in Scenario 2, while still being featured in Scenario 1. For the 200 ft. separation distance shown in Figures 4.28 and 4.31, most of the vehicles feature very similar wake profiles between the two scenarios and in comparison to the baselines of Figures 4.1 - 4.4. The most notable exception to this is the 53 ft. box trailer with side-skirts, which when placed at the rear of the platoon for 200 ft. separation distance features a smaller, and less intense recirculation zone off the trailing edge in scenario 2 than its counterpart in Scenario 1.

Scenario 1 and Scenario 3 are quite similar upon first comparison of the overall platoon savings in Figures 4.22 and 4.24. Significantly different however is the contribution to this by the respective lead vehicles, with the 40 ft. shipping container of Scenario 3 achieving much higher drag reduction than the 53 ft. box trailer of Scenario 1 (up to about 30% for the 50 ft. separation distance). More generally it seems that by swapping the positions of the two longest trailers, with Scenario 3 featuring the more optimized side-skirt trailer in a central platoon position, the platoon drag reduction is much more significantly made up of the forward trucks rather than the rear trucks, especially at 200 ft. Looking at the static pressure contours for Scenario 3 at 200 ft. in Figure 4.33, the rearmost two trucks feature extended and much stronger separation regions in the wake than even in their baseline configurations in Figures 4.1 - 4.4. This likely accounts for the decreased benefit experienced by these trucks, and also provides further support, in combination with the results of scenario 2, to the argument that the placement of more aero-optimized trailers rear of less optimized trailers is advantageous.

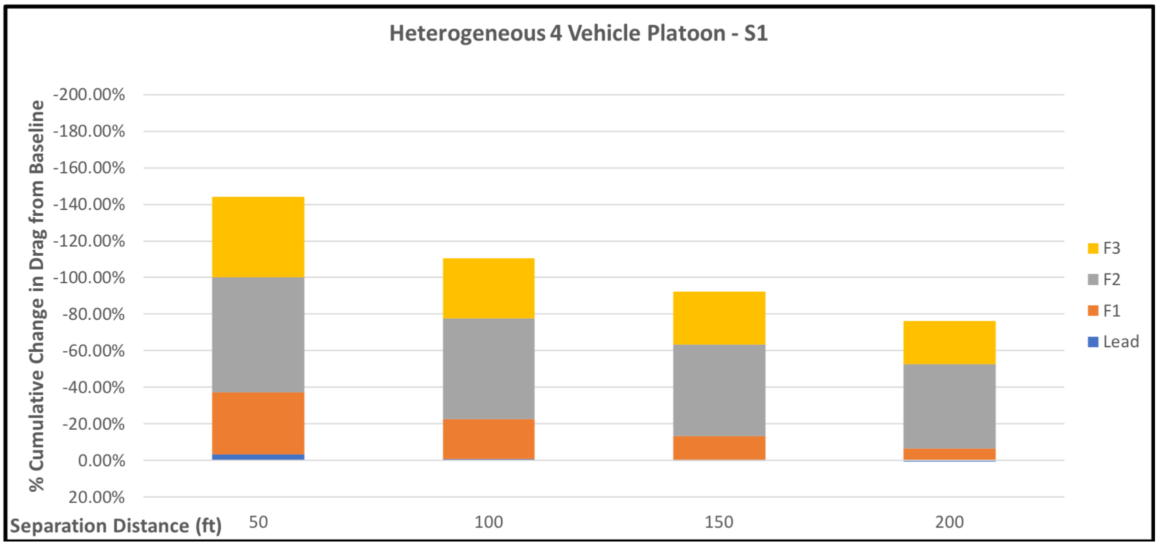

Figure 4.22: Drag reduction for heterogeneous platoon scenario 1, described in Table 3.3

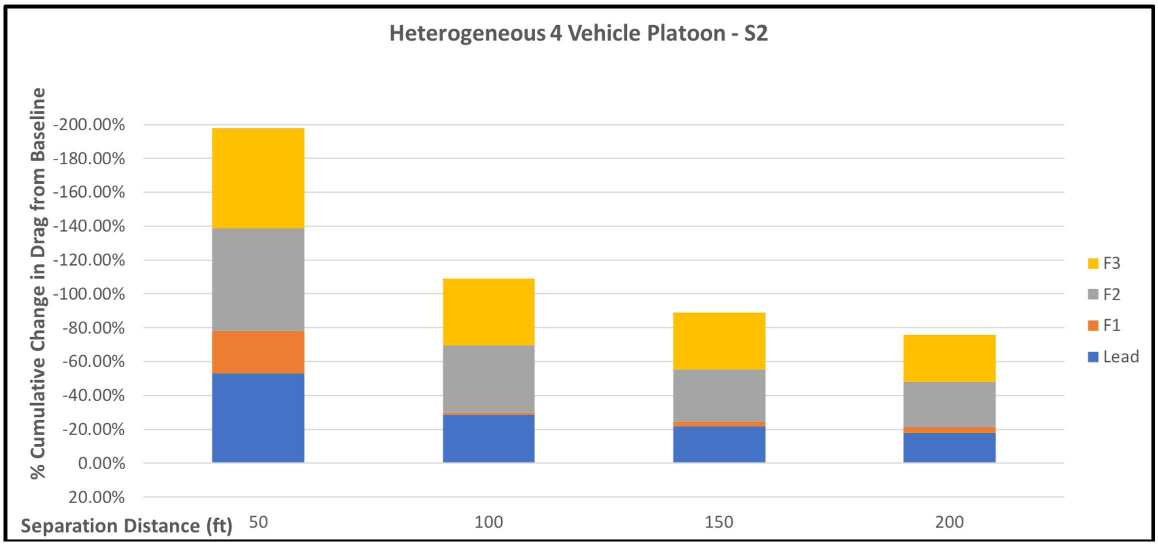

Figure 4.23: Drag reduction for heterogeneous platoon scenario 2, described in Table 3.3

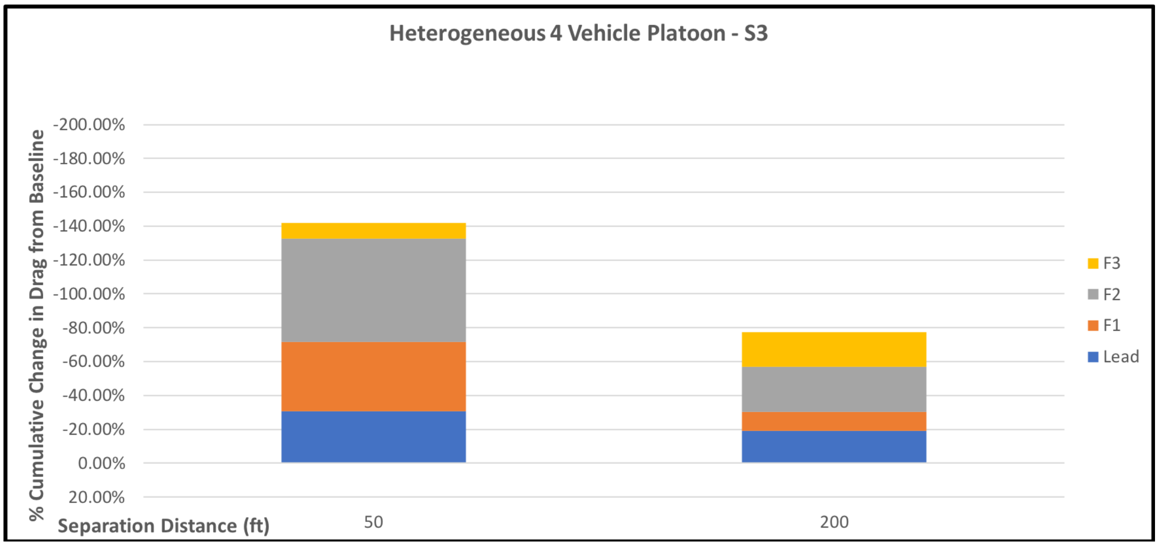

Figure 4.24: Drag reduction for heterogeneous platoon scenario 3, described in Table 3.3

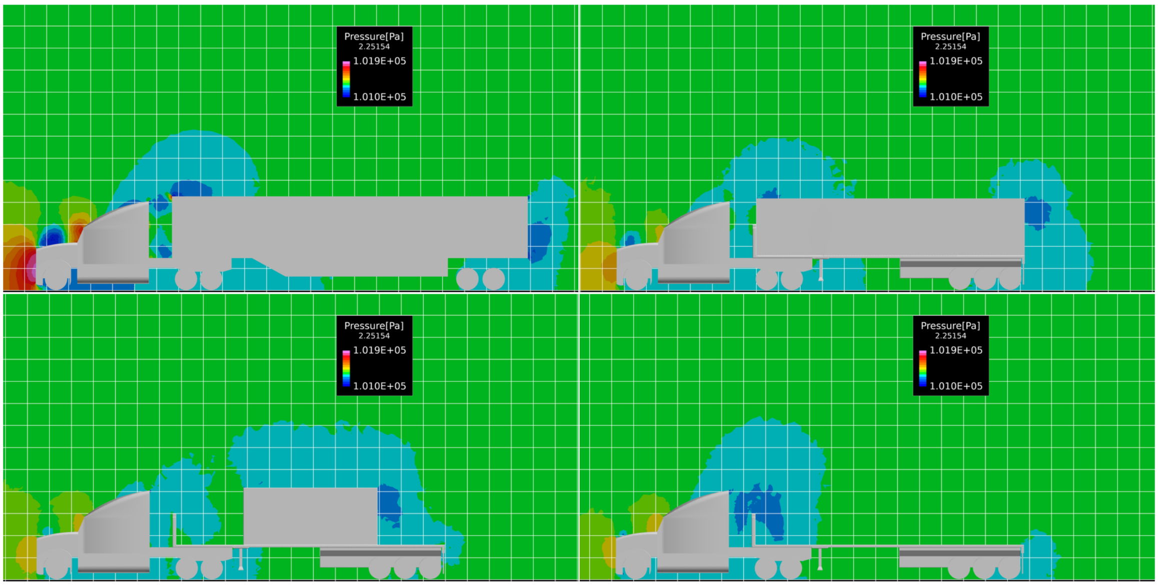

Figure 4.25: Static pressure contours for scenario 1, described in Table 3.3, at 50 ft.

Figure 4.26: Static pressure contours for scenario 1, described in Table 3.3, at 100 ft.

Figure 4.27: Static pressure contours for scenario 1, described in Table 3.3, at 150 ft.

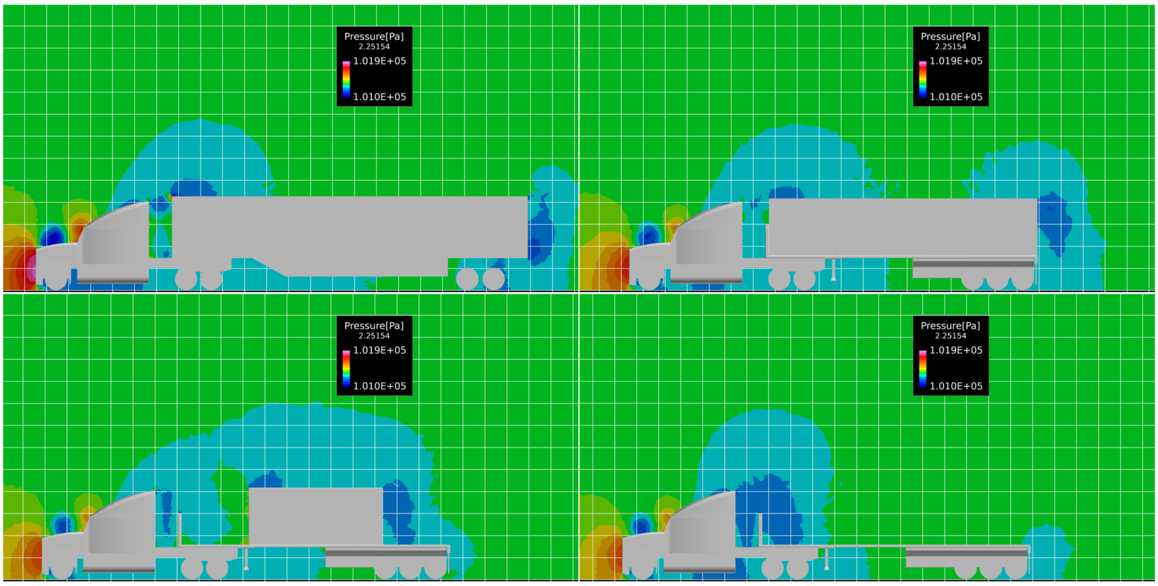

Figure 4.28: Static pressure contours for scenario 1, described in Table 3.3, at 200 ft.

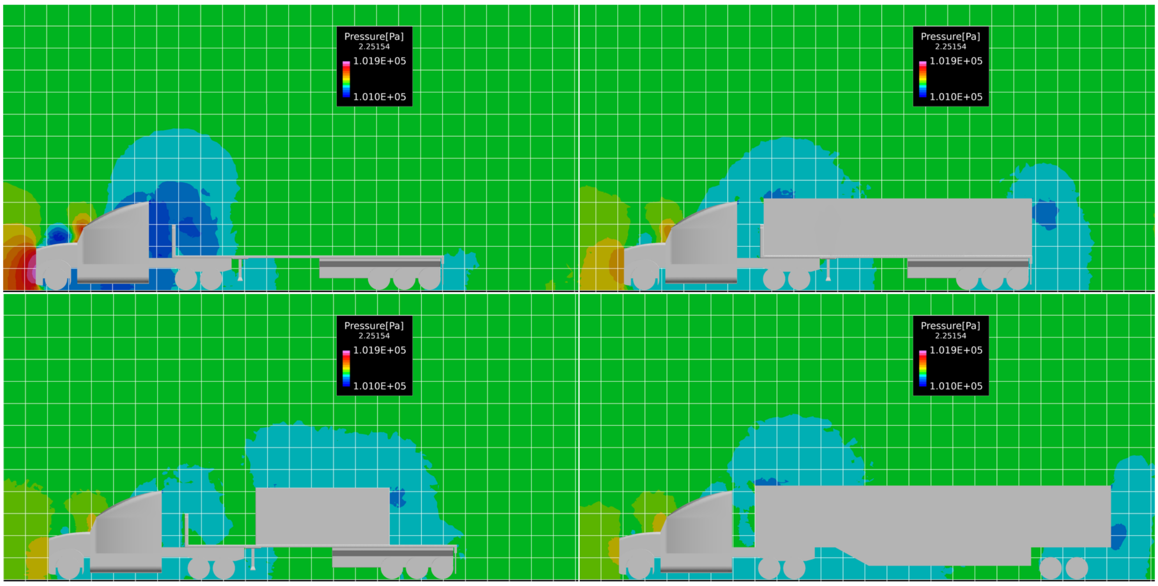

Figure 4.29: Static pressure contours for scenario 2, described in Table 3.3, at 50 ft.

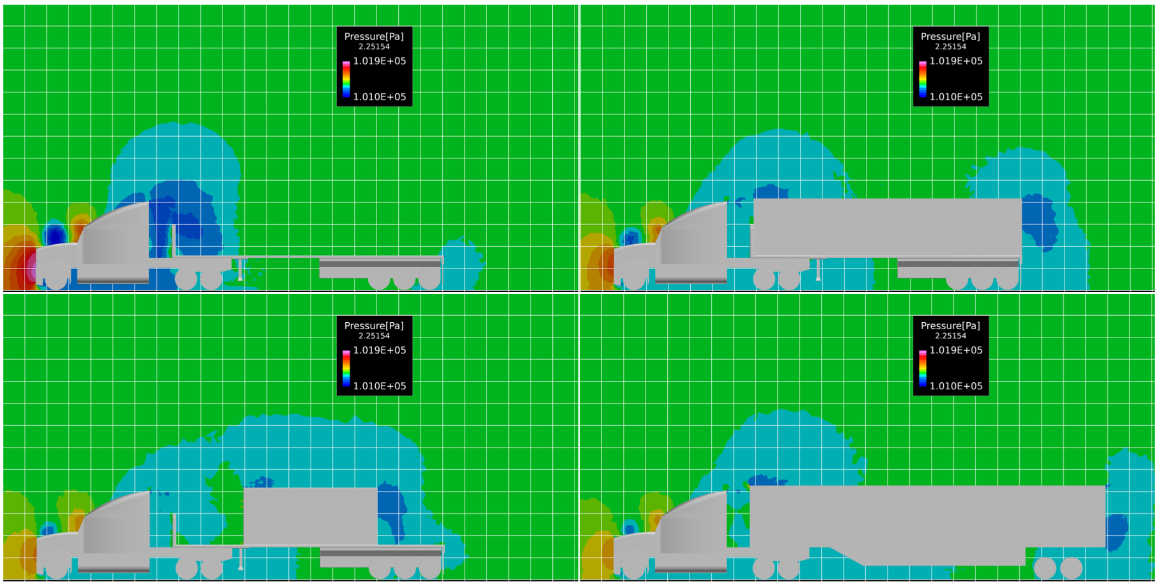

Figure 4.30: Static pressure contours for scenario 2, described in Table 3.3, at 100 ft.

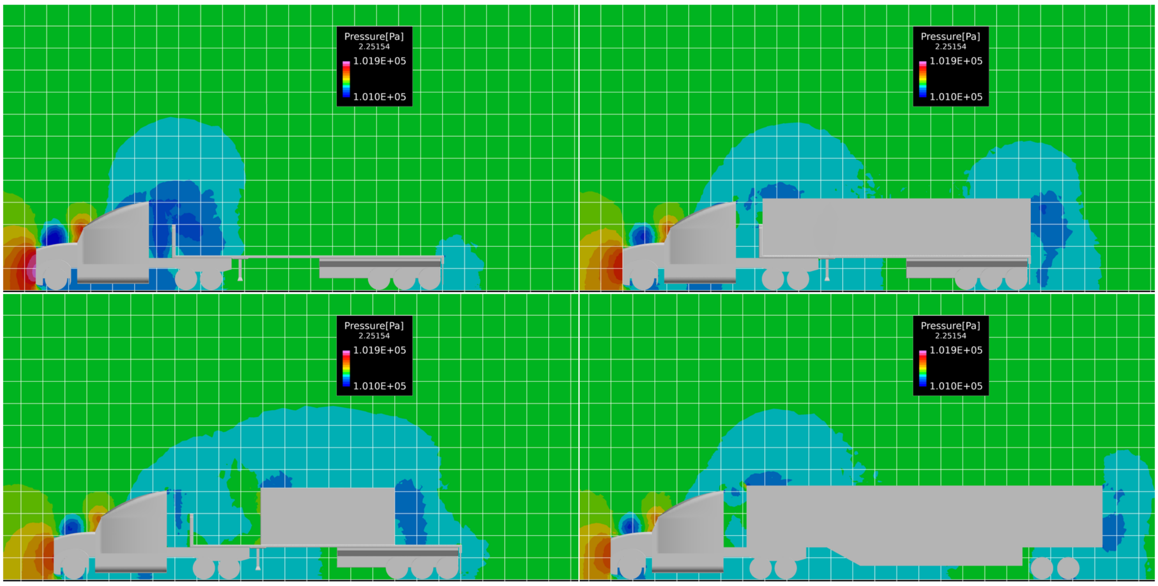

Figure 4.31: Static pressure contours for scenario 2, described in Table 3.3, at 200 ft.

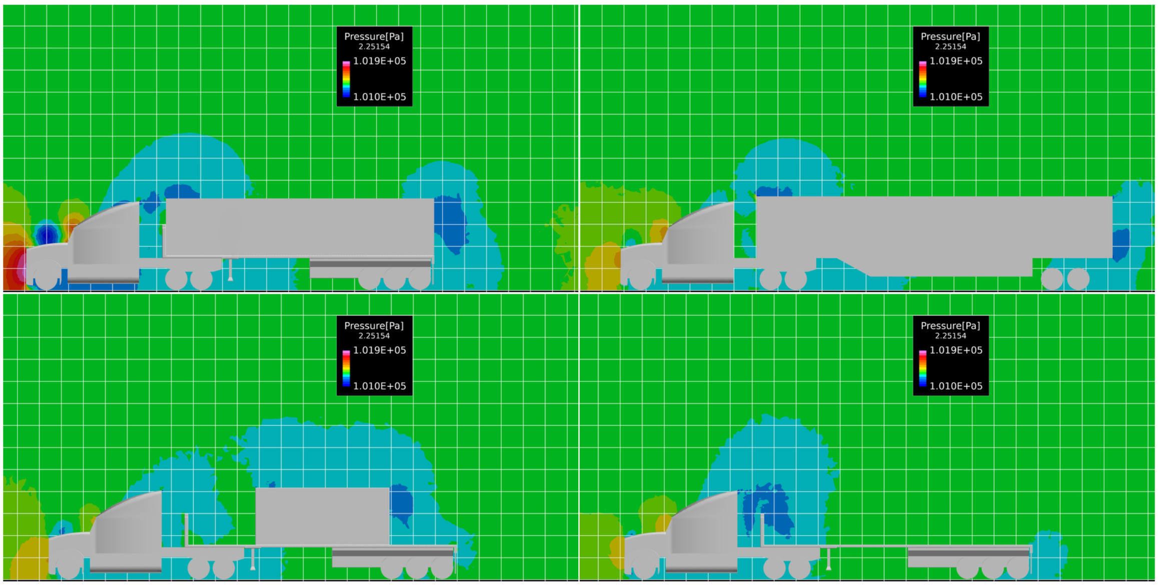

Figure 4.32: Static pressure contours for scenario 3, described in Table 3.3, at 50 ft.

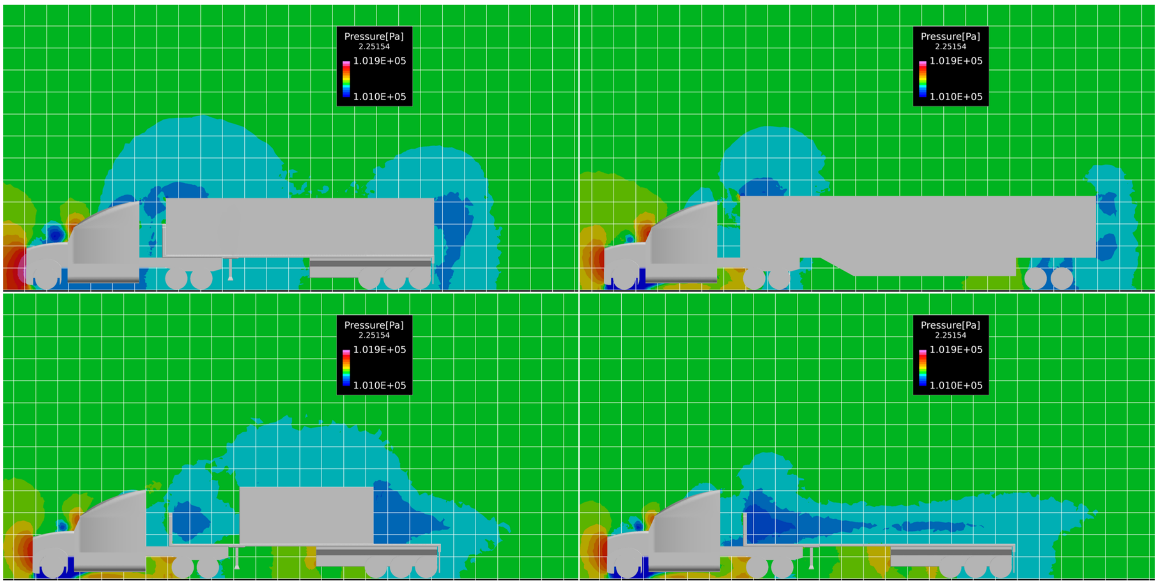

Figure 4.33: Static pressure contours for scenario 3, described in Table 3.3, at 200 ft.

Chapter 5

Conclusions & Future Work

5.1 Conclusions

This study covered a wide range of truck platoon scenarios via CFD in order to provide some ideas of important factors concerning configurations of truck platoons. The results from two truck, homogeneous platoons with induced lateral offset at smaller separation distances (less than 50 ft.) show that while the lead vehicle is mostly insensitive to changes in lateral offset, the follower vehicle experiences far more significant effects, in-line with previous Auburn University CFD studies[9]. A large spike in drag reduction at a non-minimum separation distance was noted for 10% trailer width lateral offset at 20 ft. particularly, but further lateral offsets at the same separation distance did not note any precursors or after-effects to this data point. As such, further refinement in terms of both lateral offset as well as separation distance in this region is needed in a more focused CFD study to better understand these effects beyond general conclusions, and determine the place this data point has within the broader set.

An analysis of intra-platoon separation distance variation for three vehicle homogeneous platoons was also conducted, noting that at larger homogeneous separation distances the third vehicle in the platoon saw much more drag reduction than the middle vehicle or the lead vehicle. Furthermore, at these larger separation distances, as the front distance was increased with the rear distance kept constant, the third vehicle saw little to no change in drag reduction, while the middle vehicle was fairly insensitive past a certain point as well. The reverse scenario, where the first gap was kept constant and the second gap increased, incurred much greater drag reduction for all vehicles in the platoon, including the lead vehicle. The third vehicle still saw the highest benefit overall, in-line with the other three vehicle platoons studied. These results suggest that this last scenario seems to be the most beneficial for platoons, where some leeway in separation distance is granted in the rear of the platoon when compared to the separation distances in the front of the platoon, especially in cases where it is important to maximize drag reduction on the lead vehicle.

A study of heterogeneous platoons featuring a 53 ft. box trailer with side-skirt, a 40 ft. shipping container trailer, a 20 ft. centered shipping container trailer, and an unloaded flatbed trailer was also conducted over several separation distances with three different platoon orders. The scenario with the flatbed trailer at the front of the platoon and the box trailer with side-skirt at the rear of the platoon saw significantly increased drag reduction on the platoon in comparison to the opposite scenario. This seems to be supported in results by recent track testing [11] where in scenarios featuring mismatched trailer configurations, placing the trailers with features such as side-skirts and boat-tails rearward of less optimized trailers led to similar trends. This was also supported to some extent in this study by placing the box trailer with side-skirt in a more central platoon location, rear of the 40 ft. shipping container trailer, which shifted the drag reduction benefits to the front of the platoon and limited the savings at the rear of the platoon.

5.2 Future Work

Obviously, the ideal testing scenario would involve a comprehensive test of all the individual factors presented in this paper, coupled together, as this is most representative of real-world deployments. Additionally, closer separation distances should be compared in addition to the ones presented here for three vehicle platoons, in order to determine if the recommendations from this work also apply in this region, as most current work purely studies larger separation distances.

Grid generation has proven to be a rather difficult issue for these scenarios, and as such it remains an area where great strides can still be undertaken to improve solution quality. Further refinement of the boundary layer by decreasing the initial y^+ value in addition to decreasing the growth rate may be necessary in order to capture all vortex effects accurately. However, this is dependent upon the creation of good quality cells in the final product which is not guaranteed. Additional CAD simplification may aid this, but may also degrade solution fidelity and accuracy. Alternatives in grid generation such as those presented by Onishi et al [30] to deal with ”dirty” geometries may also prove effective for these problems, allowing relatively simple steps between initial unprocessed CAD geometries to usable CFD grids.

There are of course many more separation distances and lateral offsets that can be tested in the scenarios presented by this thesis. In addition to this, there are of course methods here that would benefit from a more comprehensive approach of study. A major point of improvement is the addition of yaw angle sweeps for the freestream velocity in these tests, which is typically conducted at -6° to $+6^\circ$ yaw angle. This process allows for yaw-averaging and at least partially accounts for typical road conditions. Another major improvement involves a much longer period of time accuracy. In this thesis only 1.0 second was examined in time-accurate simulations. Additional time-accurate iterations would aid in a more complete study of the development of time-dependent features. Finally, it may behoove a study of this nature to assume some level of inlet turbulence rather than the laminar inlet presented here. This condition is more representative of true road conditions, where other traffic has already disturbed the air along the driving path. Free-stream turbulence difficult to quantify this however without some level of extensive study for particular conditions or a statistical sampling across a large number of regions.

References

[1] United States Department of Transportation: Bureau of Transportation Statistics, "National Transportation Statistics [online database]," `https://www.rita.dot.gov/bts/sites/rita.dot.gov.bts/files/publications/national_transportation_statistics/index.html`, 2017, [accessed Oct. 2017].

[2] Torrey, W. F. and Murray, D., "An Analysis of the Operational Costs of Trucking:2014 Update," `http://www.atri-online.org/wp-content/uploads/2014/09/ATRI-Operational-Costs-of-Trucking-2014-FINAL.pdf`, September 2014, [accessed Oct. 2017].

[3] Choi, H., Lee, J., and Park, H., "Aerodynamics of Heavy Vehicles," *Annual Review of Fluid Mechanics*, Vol. 46, October 2014, pp. 441–468.

[4] McCallen, R. et al., "DOEs Effort to Reduce Truck Aerodynamic Drag Through Joint Experiments and Computations [presentation]," `https://www3.nd.edu/~tcorke/w.Truck_papers/DOE_slides.pdf`, 2006, [accessed Oct. 2017].

[5] Tsugawa, S., "Results and Issues of an Automated Truck Platoon within the Energy ITS Project," *IEEE Paper*, 2014, 2014 IEEE Intelligent Vehicles Symposium (IV) June 8-11, 2014. Dearborn, Michigan, USA.

[6] Fago, B., Lidner, H., and Mahrenholtz, O., "The Effect of Ground Simulation on the Flow Around Vehicles in Wind Tunnel Testing," *Journal of Wind Engineering and Industrial Aerodynamics*, Vol. 38, 1991, pp. 47–57.

[7] Sreenivas, K., Pankajakshan, R., Nichols, D. S., Mitchell, B., Taylor, L. K., and Whitfield, D. L., “Aerodynamic Simulations of Heavy Trucks with Spinning Wheels,” *AIAA Paper 2006-1394*, 2006, 44th AIAA Aerospace Sciences Meeting and Exhibit, 9-12 January 2006, Reno, NV.

[8] Tsugawa, S., Kato, S., and Aoki, K., “An automated truck platoon for energy saving,” *2011 IEEE/RSJ International Conference on Intelligent Robots and Systems*, Sept 2011, pp. 4109–4114.

[9] Humphreys, H. and Bevly, D., “Computational Fluid Dynamic Analysis of a Generic 2 Truck Platoon,” *SAE Paper 2016-01-8008*, 2016.

[10] IV, H. H., *A Computational Fluid Dynamics Analysis of a Driver-Assistive Truck Platooning System with Lateral Offset*, Master’s thesis, Auburn University, 2017.

[11] McAulliffe, B., Lammert, M., Lu, X.-Y., Shladover, S., Surcel, M.-D., and Kailas, A., “Influences on Energy Savings of Heavy Trucks Using Cooperative Adaptive Cruise Control,” *SAE Paper 2018-01-1181*, 2018, SAE World Congress, April 2018, Detroit, MI.

[12] Schito, P. and Braghin, F., “Numerical and Experimental Investigation on Vehicles in Platoon,” *SAE International Journal of Commercial Vehicles*, Vol. 5, No. 1, apr 2012, pp. 63–71.

[13] Norrby, D., *A CFD Study Of The Aerodynamic Effects Of Platooning Trucks*, Master’s thesis, KTH Royal Institute of Technology, 2014.

[14] Vegendla, P., Sofu, T., Saha, R., Kumar, M. M., and Hwang, L.-K., “Investigation of Aerodynamic Influence on Truck Platooning,” *SAE Technical Paper 2015-01-2895*, 2015.

[15] Salari, K. and Ortega, J., “Experimental Investigation of the Aerodynamic Benefits of Truck Platooning,” *SAE Paper 2018-01-0732*, 2018, SAE World Congress, April 2018, Detroit, MI.

[16] Prandtl, L., "Proceedings of the Second International Congress for Applied Mechanics," *Proceedings of the Third Osaka Coloquium on Advanced CFD Applicationsto Ship Flow and Hull Form Design*, 1926, Zurich, Switzerland.

[17] Kays, W., Crawford, M., and Weigand, B., *Convective Heat and Mass Transfer*, McGraw-Hill, 2005.

[18] Roe, P. L., "Approximate Riemann Solvers, Parameter Vectors, and Difference Schemes," *Journal of Computational Physics*, Vol. 43, 1981, pp. 357–372.

[19] Toro, E. F., Spruce, M., and Speares, W., "Restoration of the contact surface in the HLL-Riemann solver," *Shock Waves*, Vol. 4, No. 1, Jul 1994, pp. 25–34.

[20] Sreenivas, K., Webster, R. S., and Hereth, E. A., "Impact of High-Order Spatial Accuracy on Multi-Stage Turbomachinery Simulations," *AIAA Paper 2017-4823*, 2017, 53rd AIAA/SAE/ASEE Joint Propulsion Conference, 10-12 July 2017, Atlanta, GA.

[21] Sreenivas, K., Nichols, S., Hyams, D., Mitchell, B., Sawyer, S., and Whitfield, D., "Computational Simulation of Heavy Trucks," *AIAA Paper 2007-1087*, 2007, 45th AIAA Aerospace Sciences Meeting and Exhibit, 8-11 January 2007, Reno, NV.

[22] Hyams, D. G., Sreenivas, K., Pankajakshan, R., Nichols, D. S., Briley, W. R., and Whitfield, D. L., "Computational simulation of model and full scale Class 8 trucks with drag reduction devices," *Computers & Fluids*, Vol. 41, No. 1, 2011, pp. 27 – 40, Implicit Solutions of Navier-Stokes Equations. Special Issue Dedicated to Drs. W.R. Briley and H. McDonald.

[23] Siemon, M. and Nichols, D. S., "A Numerical Investigation of Vortex Dynamics About a Streamlined Cylinder At Various Aspect Ratios," *AIAA Paper 2017-3307*, 2017, 47th AIAA Fluid Dynamics Conference, AIAA AVIATION Forum, Denver, CO.

[24] Taylor, L. K., *Unsteady Three-Dimensional Incompressible Algorithm based on Artificial Compressibility*, Ph.D. thesis, Mississippi State University, 1991.

[25] Strelets, M., “Detached Eddy Simulation of Massively Separated Flows,” *AIAA Paper 01-0879*, 2001, 39th AIAA Aerospace Sciences Meeting and Exhibit, 8-11 January 2001, Reno, NV.

[26] Peterbilt Trucks Inc., “Peterbilt 579,” `http://www.peterbilt.com/imgs/trucks/579/360/white_001.jpg`, [accessed Oct. 2017].

[27] Siemon, M., Smith, P., Nichols, D., Bevly, D., and Heim, S., “An Integrated CFD and Truck Simulation for 4 Vehicle Platoons,” *SAE Paper 2018-01-0797*, 2018, SAE World Congress, April 2018, Detroit, MI.

[28] Urick, B. and Marussig, B., “Why CAD Surface Geometry is Inexact,” `https://blog.pointwise.com/2017/11/29/why-cad-surface-geometry-is-inexact/`, [accessed Jan. 2018].

[29] SAE International, “Surface Vehicle Recommended Practice: Guidelines for Aerodynamic Assesment of Medium and Heavy Commercial Ground Vehicles Using Computational Fluid Dynamics J2966,” 2017.

[30] Onishi, K., Ando, Y., Nakasato, K., and Tsubokura, M., “Evaluation of an Open-grill Vehicle Aerodynamics Simulation Method Considering Dirty CAD Geometries,” *WCX World Congress Experience*, SAE International, apr 2018.

Appendices

Appendix A

Useful General CFD Equations

A.1 Approximation of y^+

A practical approximation of y^+ for calculation of initial viscous spacing can be obtained by the same treatment as boundary layer calculations for a flat plate. A local Reynolds number, Re_x, is first calculated such that

$$Re_x = \frac{\rho U_\infty L}{\mu} \tag{A.1}$$

Re_x is then used for an approximation of a skin friction coefficient C_f and associated wall shear stress τ_w where

$$C_f = \frac{0.026}{{Re_x}^{1/7}} \tag{A.2}$$

$$\tau_w = \frac{C_f \rho {u_\infty}^2}{2} \tag{A.3}$$

and τ_w is used for an approximation of a frictional velocity, u_f, which is then used to calculate an initial wall spacing, y, for a given y^+ by

$$u_f = \sqrt{\frac{\tau_w}{\rho}} \tag{A.4}$$

$$y = \frac{y^+ \mu}{u_f \rho} \tag{A.5}$$

which is analogous to the definition of y^+ presented in Equation 2.21.

A.2 Courant-Friedrichs-Lewy (CFL) Condition

In explicit numerical solutions for partial differential equations, it is necessary to define a Courant-Friedrichs-Lewy (CFL) condition which relates temporal discretization of a scenario to spatial discretization present in the grid. Essentially, it is the case that the artificial or true time-step used in such situations must satisfy a relation to the length of grid cells and the magnitude of the velocity of a given wave phenomena. This value, C, is defined for an n-dimensional case as

$$C = \Delta t \sum_{i=1}^{n} \frac{u_{x_i}}{\Delta x_i} \tag{A.6}$$

where $C \leq C_{max}$ with C_{max} being some specified maximum CFL value.

Appendix B

Selection of Time-Accurate Results: Lateral Offset

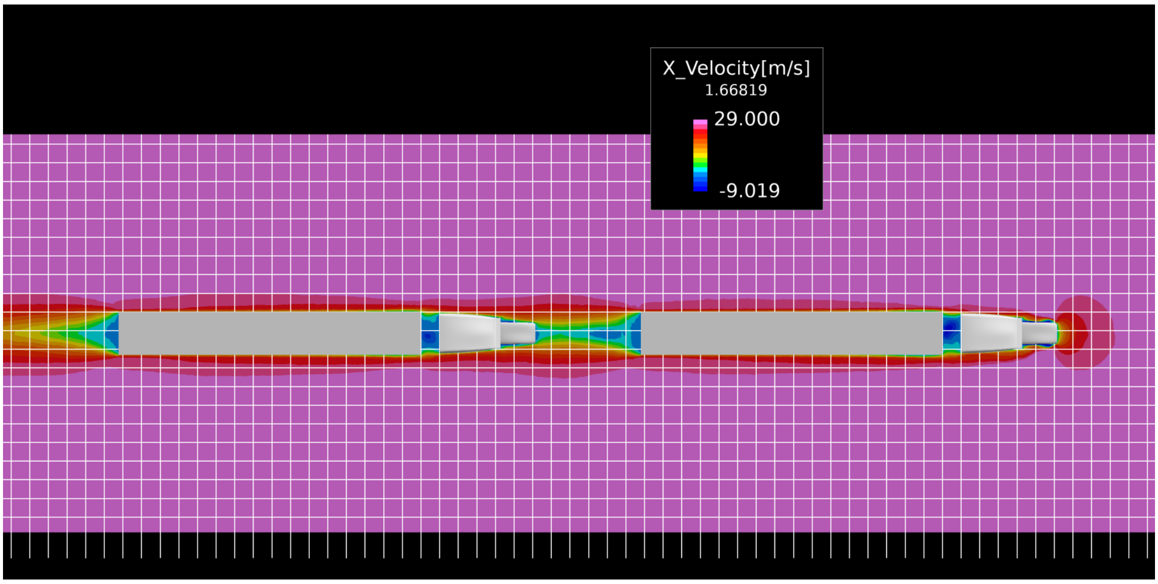

(a) $t = 0.0 - 0.1$ seconds

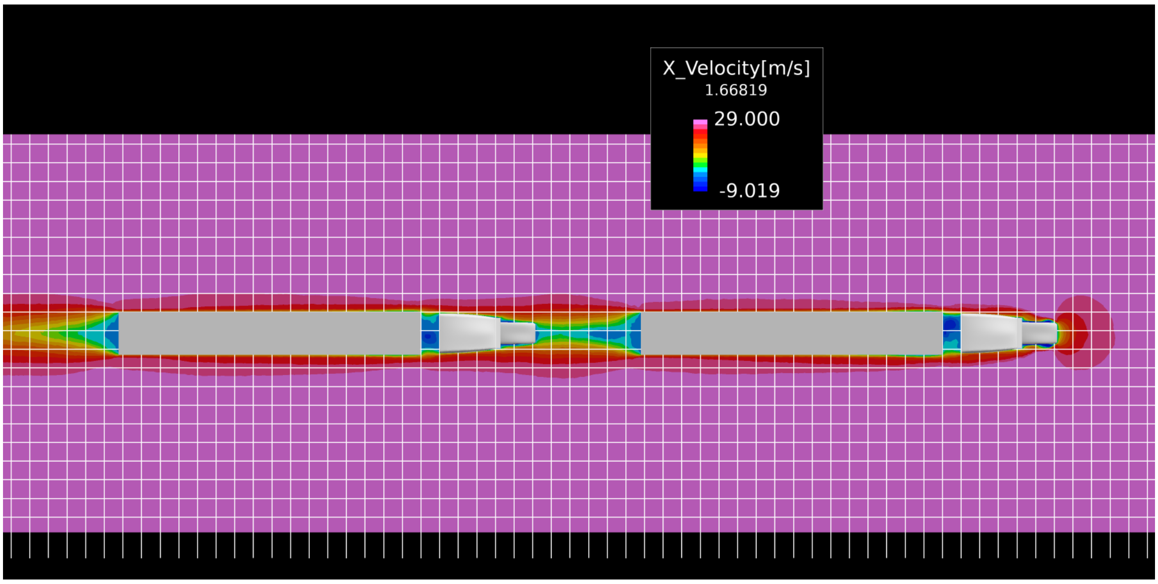

(b) $t = 0.1 - 0.2$ seconds

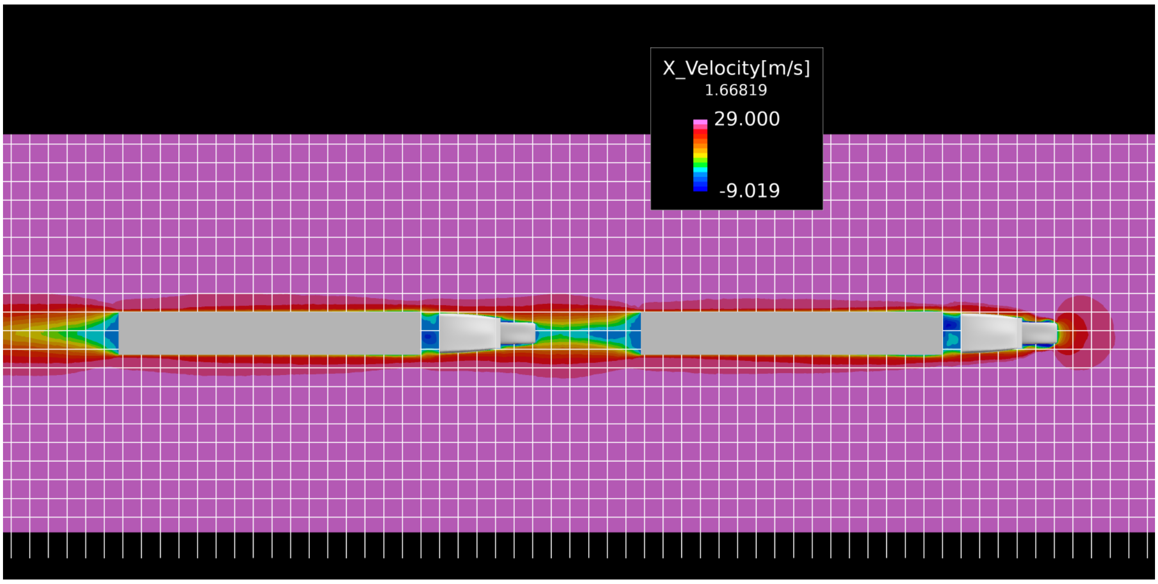

(c) $t = 0.2 - 0.3$ seconds

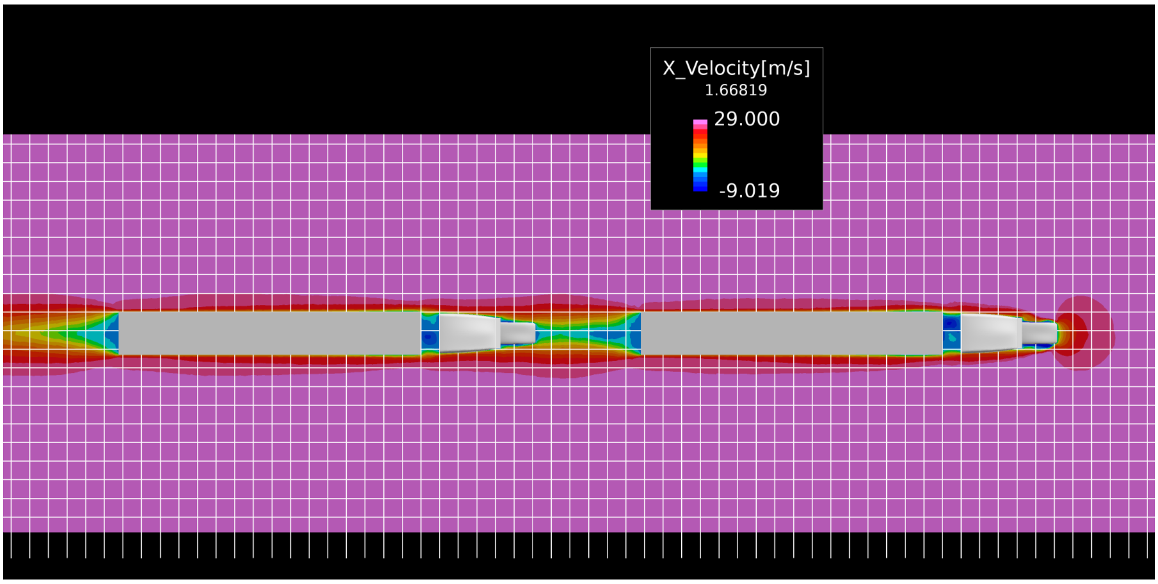

(d) $t = 0.3 - 0.4$ seconds

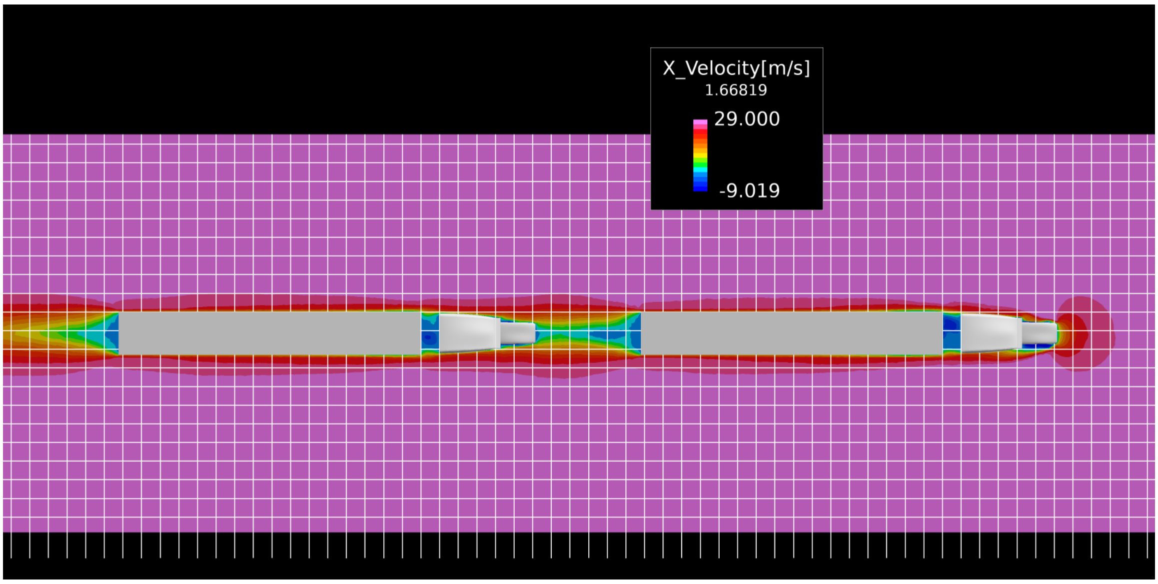

(e) $t = 0.4 - 0.5$ seconds

Figure B.1: X-Velocity profile for homogeneous, two box trailer platoon with 20 ft separation distance, 0% lateral offset, at various points in time (results are averaged across 0.1 second increments)

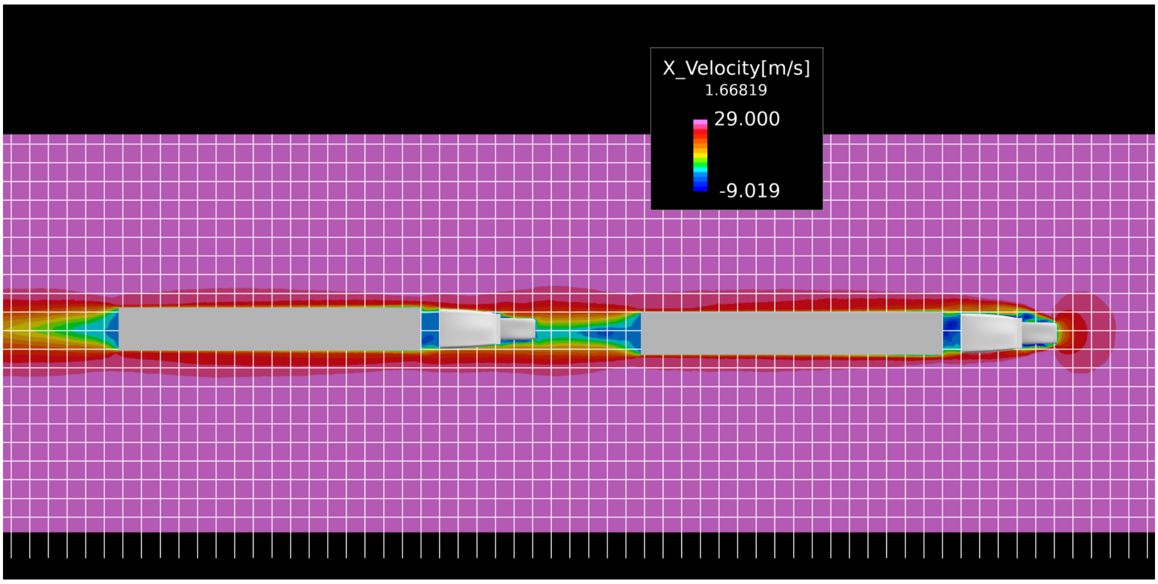

(a) $t = 0.0 - 0.1$ seconds

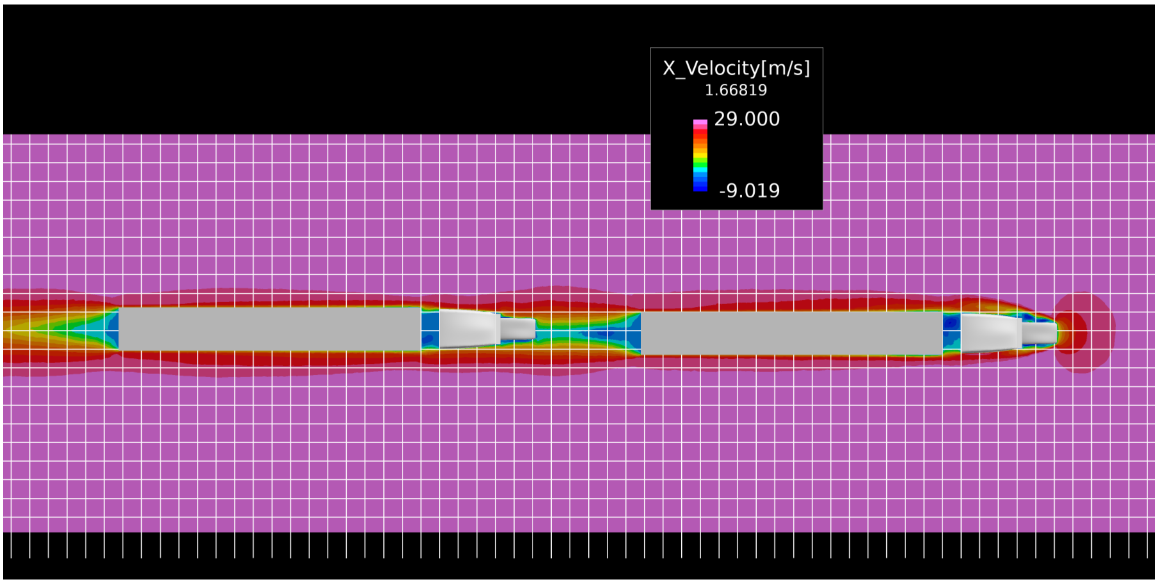

(b) $t = 0.1 - 0.2$ seconds

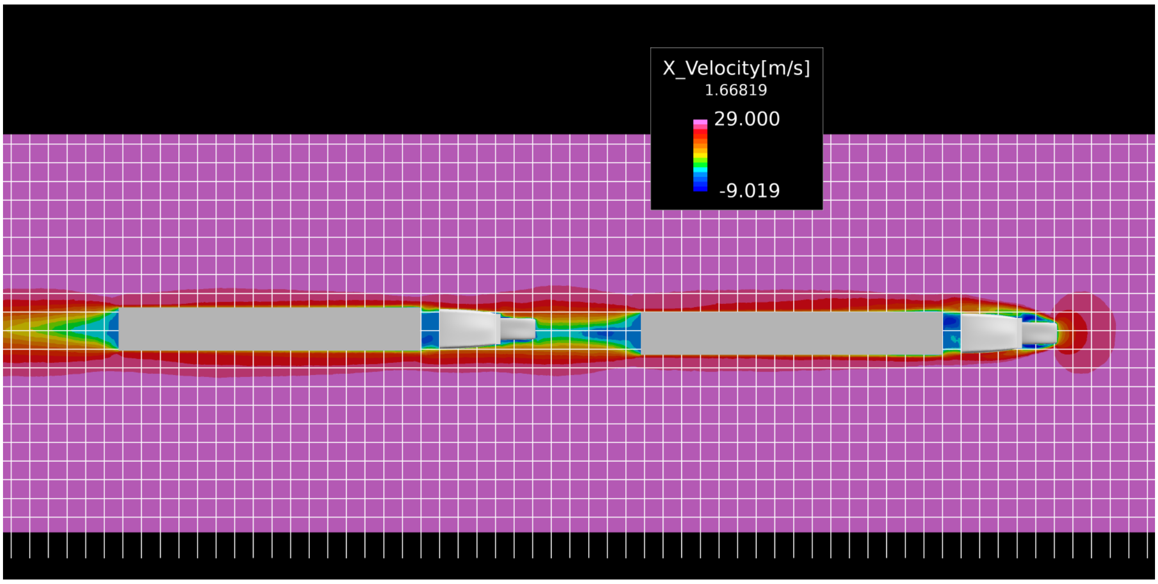

(c) $t = 0.2 - 0.3$ seconds

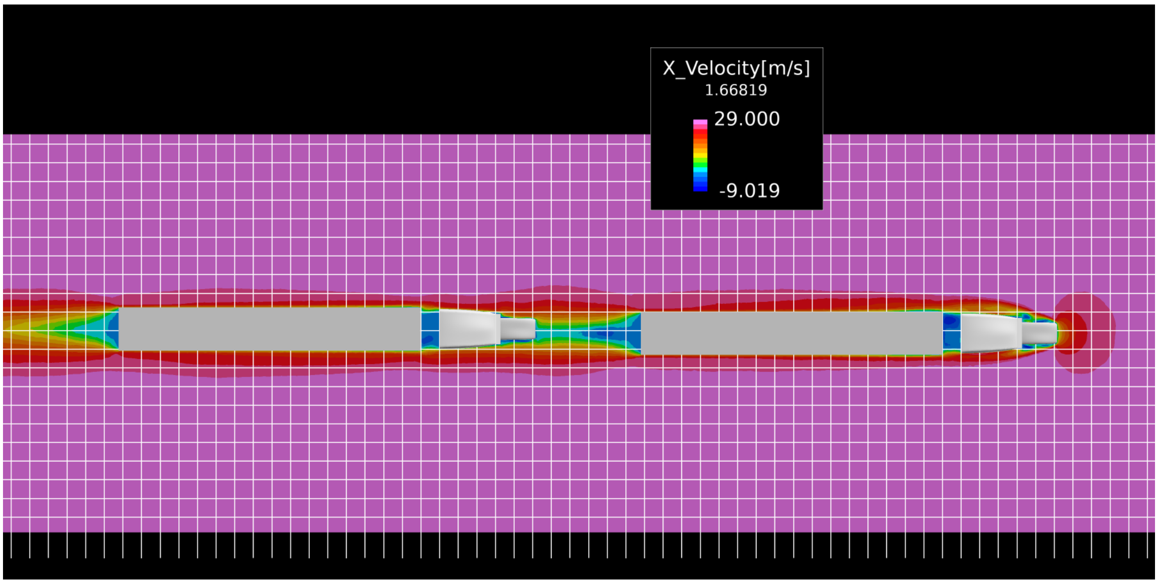

(d) $t = 0.3 - 0.4$ seconds

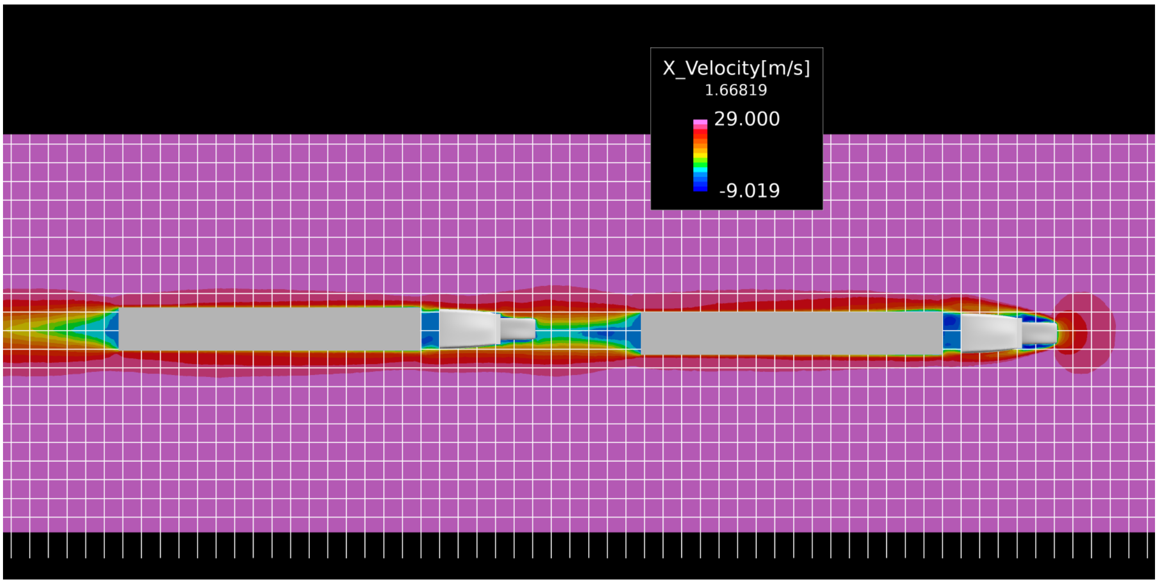

(e) $t = 0.4 - 0.5$ seconds

Figure B.2: X-Velocity profile for homogeneous, two box trailer platoon with 20 ft separation distance, 10% lateral offset, at various points in time (results are averaged across 0.1 second increments)